BINDING SERVICES
Tel +44 (0)29 2087 4949
Fax +44 (0)29 20371921
e-mail bindery@cardiff.ac.uk

Sinusoidal Frequency Estimation with Applications to Ultrasound

Thesis submitted to the University of Cardiff in candidature for the degree of Doctor of Philosophy.

Zhuo Zhang

Centre of Digital Signal Processing
Cardiff University
2005

ProQuest LLC
789 East Eisenhower Parkway
P.O. Box 1346
Ann Arbor, MI 48106-1346

DECLARATION

This work has not previously been accepted in substance for any degree and is not being concurrently submitted in candidature for any degree.

Signed ..... (candidate) Date 22/12/2005

STATEMENT 1

This thesis is the result of my own investigation, except where otherwise stated. Other sources are acknowledged by footnotes giving explicit reference. A bibliography is appended.

Signed ..... (candidate) Date 22/12/2005

STATEMENT 2

I hereby give consent for my thesis, if accepted, to be available for photocopying and for inter-library loan, and for the title and summary to be made available to out side organizations.

Signed ..... (candidate) Date 22/12/2005

ABSTRACT

This thesis comprises two parts. The first part deals with single carrier and multiple-carrier based frequency estimation. The second part is concerned with the application of ultrasound using the proposed estimators and introduces a novel efficient implementation of a subspace tracking technique.

In the first part, the problem of single frequency estimation is initially examined, and a hybrid single tone estimator is proposed, comprising both coarse and refined estimates. The coarse estimate of the unknown frequency is obtained using the unweighted linear prediction method, and is used to remove the frequency dependence of the signal-to-noise ratio (SNR) threshold. The SNR threshold is then further reduced via a combination of using an averaging filter and an outlier removal scheme. Finally, a refined frequency estimate is formed using a weighted phase average technique. The hybrid estimator outperforms other recently developed estimators and is found to be independent of the underlying frequency.

A second topic considered in the first part of this thesis is multiple-carrier based frequency estimation. Based on this idea, three novel velocity estimators are proposed by exploiting the velocity dependence of the backscattered carriers; using synthetic data, all three proposed estimators are found to exhibit the capability of mitigating the poor high velocity performance of the conventional correlation based techniques and thereby provide usable performance beyond the conventional Nyquist velocity limit. To evaluate these meth-

ods statistically, the Cramér-Rao lower bound for the velocity estimation is derived.

In the second part, the fundamentals of ultrasound are briefly reviewed. An efficient subspace tracking technique is introduced as a way to implement clutter eigenfilters, greatly reducing the computation complexity as compared to conventional eigenfilters which are based on the evaluation of the block singular value decomposition technique. Finally, the hybrid estimator and the multiple-carrier based velocity estimators proposed in the first part of the thesis are examined with realistic radio frequency data, illustrating the usefulness of these methods in solving practical problems.

ACKNOWLEDGEMENTS

I never thought the day of submitting my Ph.D. thesis would come so quickly although I have been looking forward to it. Now it has. This thesis is the culmination of the academic experience I have acquired during my Ph.D. study. Inspiration, encouragement and support have come from many people, several institutions and organizations. They certainly all contributed to the development of this thesis. It is a pleasure for me now to express my gratitude to them.

The experience of this Ph.D. study in signal processing started three years ago when my application was accepted by Prof. Jonathon A. Chambers. I would like to thank Jonathon for his expert knowledge, experience, suggestions and continuous encouragement which helped me so that all my efforts were certain to succeed. Without the support from Jonathon, this Ph.D. study would not have been possible from the very beginning to the end.

In my life as a student in schools, I have been truly fortunate to have the opportunity to work under Dr. Andreas Jakobsson. I am deeply indebted to Andreas for acting as my advisor. His constant and excellent guidance, helpful suggestions and inspiring ideas were decisive for the progress of my research. I am also grateful to Andreas for his guidance with the issues in LaTeX, Matlab, writing research papers and many useful "tricks". Under his tutorage, a long term dream and a goal for my professional life have been fulfilled.

Furthermore, I thank Dr. Malcolm D. Macleod for the rewarding discussions about the

single tone estimation; I am also grateful to Prof. Peter N. T. Wells for interesting and stimulating discussions about ultrasound. I thank both of them for acting as my faculty opponents.

Reflecting on my international research visits, I thank Prof. Jørgen Arendt Jensen for inviting me twice to visit the *Center for Fast Ultrasound Imaging* (CFU) at Technical University of Denmark and Dr Andreas Jakobsson for inviting me to visit the *Center for Control, Signals and Systems* (CCSS) at Kalstad University, respectively. Both the visits were fruitful and rewarding. Thanks also go to Dr. Svetoslav Nikolov, Dr. Malene Schlaikjer, Mr. Jesper Udesen and Mr. Fredrik Gran at CFU for the stimulating discussions and their help using the Field II toolbox. I also express my appreciations to Ms Elna Sørensen at CFU and Ms Carin Bergström-Carlsson at CCSS for their indispensable assistance helping me settle in in Copenhagen and Kalstad, respectively.

I very gratefully acknowledge the financial support from UK Universities, Cardiff University, King's College London, China-UK Trust and the Wing Yip Brothers for supporting me to complete my Ph.D. study.

I also wish to thank all my research companions both at King's College London and Cardiff University, past and present; Dr. Wenwu Wang, Dr. Yuhui Luo, Dr. Maria Jafari, Dr. Cenk Toker, Dr. Sajid Ahmed, Mr. Thomas Bowles, Mr. Rab Nawaz, Mr. Clive Cheong Took, Mr. Yonggang Zhang, Mr. Qiang Yu, Mr. Cheng Shen, Mr. Andrew Aubrey, Mr. Li Zhang, Ms Min Jing, Ms Yue Zheng and Ms Lay Teen, for their great company and support over the last three years.

Finally, I thank my parents, sister and two brothers for their unconditional care, support and encouragement; I thank my girlfriend, Xia, for her unremitting support. Without their love and support, I will not be where I am now.

CONTENTS

Acronyms

BSS Blind Source Separation

CFI Colour Flow Imaging

CRLB Cramér-Rao Lower Bound

DAVE Data Adaptive Velocity Estimator

DKLT Discrete Karhunen-Loève Transform

EVD Eigenvalue Decomposition

FCFB Four Channel Forward Backward

FFT Fast Fourier Transform

FIR Finite Impulse Response

ICA Independent Component Analysis

IIR Infinite Impulse Response

ILP Iterative Linear Prediction

KAT Kasai's Autocorrelation Technique [KNKO85]

KWPA Kay's Weighted Phase Average

LOS Line of Sight

ML Maximum Likelihood

MSE Mean Square Error

NAT Nitzpon *et al.*'s extended Autocorrelation Technique [NRB+95]

NLS Nonlinear Least Squares

ORE Outlier Removal Estimator

PCA Principal Component Analysis

PW Pulsed Wave

R-SWASVD Revised Sliding Window Adaptive SVD

RF Radio Frequency

ROI Region of Interest

SNR Signal-to-Noise Ratio

SVD Singular Value Decomposition

SVE Subspace-based Velocity Estimator

SWASVD Sliding Window Adaptive SVD

UWLP Unweighted Linear Prediction

UWPA Unweighted Phase Average

List of Figures

List of Tables

Chapter 1

INTRODUCTION

"I hear, I forget;
I see, I remember;
I do, I understand."
A Chinese Saying.

The work comprising this Ph.D. study is primarily concerned with single and multiple frequency estimation, together with efficient implementation of subspace tracking. Several approaches to these problems are proposed in this thesis. To examine performance, the methods are evaluated using both synthetic data and realistic medical ultrasound data. The present chapter serves as an introduction and an overview of the main topics covered in this thesis.

1.1 Motivation and Overview

Parameter estimation has been a classical problem for more than 200 years [Pro95] and is still an important research topic with a wide range of practical applications such as in biomedicine, communications, radar and speech (see, e.g., [Pro89, Edd93, Jen96a, KP95, EM00, SM05]

and the references therein). More specifically, in biomedicine, estimation of various signal characteristics from a patient, such as ultrasound-based radio frequency (RF) data, can, for instance, provide information about Doppler shift which can be useful in colour flow imaging (CFI) for blood velocity estimation [Jen96a, EM00]. In communications, one problem of current interest is the need to track the time-varying parameters in a cellular radio system [Pro89]. In radar and sonar systems, an accurate estimate can provide information on the location and motion of targets situated in the field of view [Edd93, SM05]. In speech, parameter estimation of audio signals can be useful in better understanding the speech production process as well as for speech synthesis, coding and recognition [KP95]. A vast number of other applications can easily be found.

An estimate can be formed using either a parametric or a nonparametric approach. Most modern estimation approaches in signal processing are model-based in the sense that they rely on certain assumptions made on the observed data. In particular, the topic of sinusoidal parameter estimation has received a huge interest in recent decades, with numerous books written on the topic (see, e.g., [Mar87, Kay88, QH01, SM05], and the references therein). One reason for this is due to the wide applicability of such problems. A typical sinusoidal model can be written as a sum of complex-valued sinusoid(s) corrupted by a Gaussian noise process typically not known, e.g,

$$y_s(t) = x_s(t) + e(t) \quad ; \quad x_s(t) = \sum_{k=1}^{d} \alpha_k(t) e^{i(\omega_k t + \varphi_k)} \quad , \tag{1.1.1}$$

where $x_s(t)$ denotes the (complex-valued) noise-free sinusoidal signal; $\{\alpha_k(t)\}$, $\{\omega_k\}$ and $\{\varphi_k\}$ are its time-varying amplitudes (power), angular frequencies and initial phases, respectively; and $e(t)$ is an additive observation noise which is often assumed to be zero mean complex-valued circular white with Gaussian distribution. Often, one is only interested in one or some of the parameters in (1.1.1), depending on the specific application. Typically, estimation of the frequencies is often the crucial step in the problem because they are nonlinear functions

in the received data sequence. In addition, in many applications, it is the frequency contents of a signal that carry the information about some desired property, e.g., Doppler shift and the resulting blood velocity in CFI. Once the frequencies have been determined, the remaining parameters, namely amplitudes and phases, can then be computed straightforwardly [SM05]. It is noteworthy that for exponentially damped sinusoids, one also needs to determine the extra parameters of damping factors, which can be estimated jointly with the frequencies [ZH97], or separately using least-squares or forward-backward linear prediction (see, e.g., [Sto93, ZH97, VSH+00, KK01], and the references therein). In general, many algorithms are tested on the basis of limited length synthetic sinusoidal data samples, which is feasible if the sinusoidal data model closely matches the practical data. However, in the real world, many signals are non-stationary, have a frequency spread (broadband) and/or exhibit a non-sinusoidal property with power damping, corrupting the data model commonly causing the estimation procedure to fail. An example of an area where such problems are encountered is in medical ultrasound where one tries to extract information from a backscattered RF signal, which will be discussed in later chapters. Given the great interest in good methods for frequency estimation, vast numbers of approaches have been proposed over the years, each with their own pros and cons. In this thesis, several frequency estimators are proposed based on a simplified version of (1.1.1) as discussed later. Herein, the proposed methods are motivated and associated with the application of ultrasound-based blood velocity estimation. However, it is worth emphasizing that these estimators can be easily extended/applied to related problems in radar and sonar and other possible applications.

Another topic this thesis deals with is subspace estimation and tracking in association with the application of clutter rejection in CFI. Subspace-based signal analysis consists of splitting the observations into a set of desired and a set of uninteresting components which can be viewed in terms of signal and noise subspaces. In CFI, the observed radio frequency (RF) ultrasound data normally contains a disturbing clutter component which is

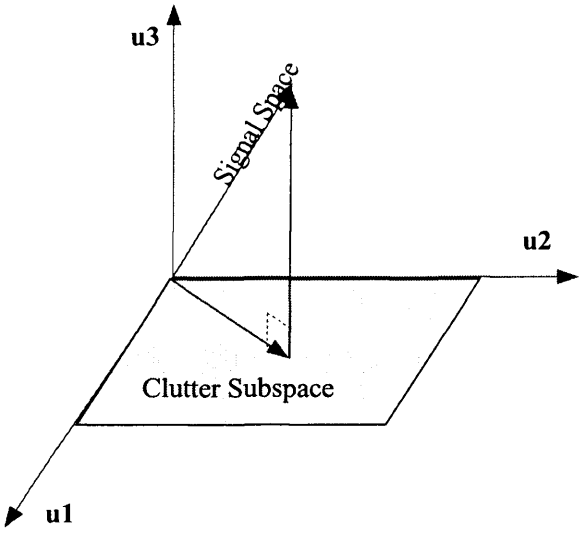

Figure 1.1. Projection of a signal space (spanned by basis vectors $\mathbf{u}_1$, $\mathbf{u}_2$ and $\mathbf{u}_3$) into a clutter subspace (spanned by basis vectors $\mathbf{u}_1$ and $\mathbf{u}_2$).

much stronger than the echoes from blood scatters [Jen96a, EM00]. To estimate accurately blood velocities, the clutter component must be first suppressed; this step is termed *clutter rejection*. Clutter rejection can be performed in many different ways, which will be further discussed in Chapter 5. One of the promising methods is the recently developed *eigenfilter* technique which is based on estimating the clutter subspace using the eigenvalue decomposition (EVD) technique, or alternatively, using the singular value decomposition (SVD) technique (see, e.g., [BHR95, LBH97, EM00, BTK02], and the references therein). Once the clutter subspace is formed, the clutter component can be removed by projecting the observed

RF signal onto the space orthogonal to the clutter subspace, as depicted in Figure 1.1, where the clutter subspace is spanned by basis vectors $\mathbf{u}_1$ and $\mathbf{u}_2$. However, the computational cost of evaluating the required SVD, or alternatively the estimation of the correlation matrix of the examined RF signal and the computation of its EVD is often prohibitive, limiting the practical applicability of the eigenfilter in CFI. Therefore, there is a real need for the computationally efficient implementation of this approach. In this thesis, we exploit the fact that the clutter signal has a slowly time-varying nature both in the temporal and spatial direction, enabling an efficient evaluation of the consecutive SVDs using a subspace tracking technique refining the sliding window adaptive SVD (SWASVD) algorithm proposed by Badeau *et al.* [BRD04].

1.2 Thesis Outline and Contributions

This thesis consists of two parts, *estimation using a single carrier or multiple carriers* and a focus *application: ultrasound.* This section presents the outline and contributions of this thesis.

1.2.1 Estimation Using a Single Carrier Or Multiple Carriers

This part of the thesis includes Chapter 2 and Chapter 3 which deal with general single tone estimation as well as multiple-carrier based velocity estimation. As some of this part of the thesis is associated with Part II, which mainly concerns with the application of medical ultrasound, readers can also refer to Chapter 4 in Part II to obtain some fundamentals of ultrasound.

Chapter 2

This chapter discusses single frequency estimation, particularly with phase-based techniques. The topic of computationally efficient frequency estimation of a single complex sinusoid corrupted by additive white Gaussian noise has received significant attention over the last decades due to the wide applicability of such estimators in a variety of fields (see, e.g., [RB74, Kay89, CKQ94, H95, KNC96, FJ99, QH01, Fow02, Mac04, Kle05], and the references therein). In this chapter, a computationally fast and statistically improved hybrid single tone estimator is proposed. The proposed approach outperforms other recently proposed methods, lowering the signal-to-noise ratio at which the Cramér-Rao lower bound is reached.

The work of this chapter has been published in part as:

- Z. Zhang, A. Jakobsson, M. D. Macleod, and J. A. Chambers, *Hybrid Phase-based Single Frequency Estimator*, IEEE Signal Processing Letters, 12(9):657-660, Sept. 2005.
- Z. Zhang, A. Jakobsson, M. D. Macleod, and J. A. Chambers, *Computationally Efficient Estimation of a Single Tone*, In IEEE 13th Workshop on Statistical Signal Processing, Bordeaux, France, July 2005.
- Z. Zhang, A. Jakobsson, M. D. Macleod, and J. A. Chambers, *Statistically and Computationally Efficient Frequency Estimation of a Single Tone*, Tech. Rep. EE-2005-02, Dept. of Electrical Engineering, Karlstad Univ., Karlstad, Sweden, February 2005.

Chapter 3

Typically, velocity estimators based on the estimation of the Doppler shift will suffer from a limited unambiguous velocity range. In this chapter, three novel multiple-carrier based velocity estimators extending the velocity range above the Nyquist velocity limit are proposed.

Numerical simulations indicate that the proposed estimators offer improved estimation performance as compared to other existing techniques.

The work of this chapter has been published in part as:

- Z. Zhang, A. Jakobsson, S. Nikolov, and J. A. Chambers. *Extending the Unambiguous Velocity Range Using Multiple Carrier Frequencies*, IEE Electronics Letters, 41(22):1206-1208, Oct. 2005.
- Z. Zhang, A. Jakobsson, and J. A. Chambers, *On Multicarrier-based Velocity Estimation*, Tech. Rep. EE-2005-04, Dept. of Electrical Engineering, Karlstad Univ., Karlstad, Sweden, May 2005.

1.2.2 Application: Ultrasound

Following the first part of the thesis, the second part consists of Chapter 4, Chapter 5 and Chapter 6, which are mainly concerned with the application of ultrasound. The hybrid single tone estimator and multiple-carrier based estimators proposed in Part I will be examined in this part with realistic RF data simulated with the Field II toolbox. The details on how to simulate RF data with the Field II toolbox can be found in [Jen01, Jen96b].

Chapter 4

Before examining the proposed methods in the context of ultrasound, it is preferable to introduce some general theory of ultrasound. In this chapter, some basic theory of acoustics and the fundamentals of medical ultrasound are introduced.

Chapter 5

In colour flow imaging, efficient clutter rejection is a key preprocessing step prior to blood velocity estimation. In this chapter, an efficient implementation of clutter eigenfilters using a recent developed subspace tracking technique is introduced.

The work of this chapter has been published in part as:

- Z. Zhang, A. Jakobsson, J. A. Jensen, and J. A. Chambers, *On the Efficient Implementation of Adaptive Clutter Filters for Ultrasound Color Flow Imaging*, In Sixth IMA International Conference on Mathematics in Signal Processing, pages 227-230, Cirencester, UK, 2004.

Chapter 6

This chapter is concerned with blood velocity estimation using the hybrid single tone estimator and the multiple-carrier based estimators proposed in Part I.

The work of this chapter has been published in part as:

- Z. Zhang, A. Jakobsson, M. D. Macleod, and J. A. Chambers, *On the Efficient Estimation of Blood Velocities*, In Proceedings of the 2005 IEEE Engineering in Medicine and Biology 27th Annual Conference, Shanghai, China, Sept. 2005.
- Z. Zhang, A. Jakobsson, S. Nikolov, and J. A. Chambers, *Novel Velocity Estimator Using Multiple Frequency Carriers*, In Medical Imaging 2004: Ultrasonic Imaging and Signal Processing, volume 5373, pages 281-289, San Diego, USA, Feb. 2004.

Chapter 7

This chapter will summarize the work involved in this thesis and will suggest some related topics for future work.

Part I

Estimation Using a Single Carrier Or Multiple Carriers

Chapter 2

EFFICIENT ESTIMATION OF A SINGLE TONE

The frequency estimation of a single tone corrupted by additive white Gaussian noise has received significant attention over the last decades due to its wide applicability in signal processing. In this chapter, a computationally fast and statistically improved hybrid single tone estimator is proposed, which outperforms other recently proposed approaches. Numerical simulations indicate that, in contrast to many other techniques, the performance of the hybrid estimator is essentially independent of the underlying frequency component. Furthermore, it has also been examined for how power damping and frequency spread affect the performance of the estimator.

2.1 Introduction

Frequency estimation is a topic widely occurring in signal processing and can be roughly classified into two main parameter estimation problems:

- Single tone estimation: where the signal is a single, constant-frequency sinusoid, corrupted by some noise.
- Multi-carrier frequency estimation: where there are several carriers of harmonically

related or unrelated frequencies present as in the multiple-carrier based estimators to be discussed in Chapter 3.

In this chapter, discussion will be confined to single tone estimation. The problem of estimating the frequency of a sinusoid in noise has received much attention in the literature as the problem arises in many areas of applied signal processing, such as biomedicine, communications and radar [Edd93, Wai02, Jen96a]. One often encounters a need to find a low computational complexity estimate of the frequency component of data which are assumed to consist of a single complex sinusoid corrupted by additive white Gaussian noise, and the topic has, as a result, attracted significant interest over the last decades (see, e.g., [LRP73, RB74, Tre85, Kay89, LM89, LW92, Cla92, CKQ94, H95, KNC96, FJ99, Qui00, Fow02, Mac04, Kle05], and the references therein). The problem can be briefly stated as follows; consider the data sequence

$$y(t) = \beta e^{i(\omega t+\theta)} + n(t), \tag{2.1.1}$$

where $\beta \in \mathbb{R}$, ω and $\theta \in [-\pi, \pi)$ denote the deterministic but unknown amplitude, frequency, and initial phase, respectively, of a complex sinusoid. Further, $n(t)$ is circular zero mean complex Gaussian white noise with variance σ_n^2. Then, given the sequence $y(t)$, for $t = 0, \ldots, N-1$, the problem is simply to estimate accurately ω with the lowest possible computational complexity. In [RB74], Rife and Boorstyn derived the maximum likelihood (ML) estimator of ω and proposed a statistically efficient approximate ML approach involving both a combined coarse and fine search using the fast Fourier transform (FFT) algorithm. However, zeropadding is often required to obtain sufficient resolution, requiring $\mathcal{O}(N' \log_2 N')$ operations, where N' is the size of the desired frequency grid, with typically $N' \gg N$. Furthermore, an iterative linear prediction (ILP) approach requiring $\mathcal{O}(N \log_2 N)$ operations was suggested in [BW02] showing similar performance to that of the ML estimator. A variety of phase-based methods requiring only $\mathcal{O}(N)$ operations have been developed. In [Tre85], for example, Tretter proposed a phase-based approach simplifying the problem

to a linear regression on the phase. The method is based on a phase unwrapping algorithm, requiring a very high signal-to-noise ratio (SNR) ($SNR \gg 1$), here defined as

$$SNR = \frac{\beta^2}{\sigma_n^2}, \tag{2.1.2}$$

to work well. Later, Kay proposed a modified version of Tretter's algorithm avoiding the use of the phase unwrapping algorithm [Kay89]. The method, here termed Kay's weighted phase average (KWPA) estimator, was claimed to be unbiased and its variance attains the Cramér-Rao lower bound (CRLB) for sufficiently high SNR (a higher threshold than the ML method). Later, analysis showed that the KWPA method is in general biased, and the SNR for which the CRLB is achieved depends on the underlying frequency [CKQ94, LW92, Qui00]. For much of the frequency range, the KWPA method can not handle the circular nature (rotation) of frequency correctly. As a result, the focus of recent contributions has mainly been aimed at reducing the SNR threshold [KNC96], the frequency dependency of the threshold [Cla92], or both [FJ99, Mac04].

In this chapter, we propose a hybrid method combining the ideas in [KNC96, FJ99, Mac04] to show performance close to that of ML or ILP, but only requiring $\mathcal{O}(N)$ operations. The hybrid estimate is based on an initial coarse estimate of the unknown frequency using the unweighted linear prediction (UWLP) method [LRP73, Kay89]; this estimate is used to remove the frequency dependence of the SNR threshold. This SNR threshold is then further reduced via a combination of using an averaging filter, as suggested in [KNC96], and an outlier removal scheme as proposed in [Mac04]. Finally, a refined frequency estimate is formed along the lines proposed in [KNC96, FJ99]. In Section 2.2, several basic estimators are discussed, including the ML estimator in Section 2.2.1, the UWLP in Section 2.2.2, the KWPA in Section 2.2.3; then the proposed hybrid estimator is given in Section 2.2.4. Section 2.4 contains numerical examples, with a conclusion in Section 2.5.

2.2 Single Tone Estimators

In this section, an overview of recent single frequency estimators is presented as well as the proposed hybrid estimator. In this section, all the results have been obtained using 10^3 Monte Carlo simulations.

2.2.1 Maximum Likelihood Estimator

If the additive noise, $n(t)$, in (2.1.1) is a zero mean white Gaussian process, the ML estimator of the frequency ω in (2.1.1) is the maximizer of the likelihood function (also called the joint probability density function) of the sequence $\{y(t)\}$, given as

$$\hat{\omega}_{MLE} = \arg\max_{\omega} f(\mathbf{y};\xi), \tag{2.2.1}$$

where $\hat{\omega}_{MLE}$ is the ML estimate, with the likelihood function defined as

$$f(\mathbf{y};\xi) = \frac{1}{(\pi\sigma_n^2)^N} \exp\left(-\frac{1}{\sigma_n^2}\sum_{t=0}^{N-1}\left(y(t) - \beta e^{i(\omega t+\theta)}\right)^2\right), \tag{2.2.2}$$

where $\mathbf{y} = [y(0),\cdots,y(N-1)]^T$, σ_n^2 = the noise variance and $\xi = [\beta,\omega,\theta]^T$, with $[\cdot]^T$ denoting the transpose operation. Maximizing (2.2.1) is equivalent to minimizing

$$\hat{\omega}_{MLE} = \arg\min_{\omega} \sum_{t=0}^{N-1}\left(y(t) - \beta e^{i(\omega t+\theta)}\right)^2, \tag{2.2.3}$$

which can be seen to be the nonlinear least squares (NLS) estimation problem. It can readily be shown that the NLS estimate of the frequency of a single sine wave buried in white noise is given by the peak of the periodogram of the data sequence [SM05], i.e.,

$$\hat{\omega}_{MLE} = \arg\max_{\omega} P(\omega), \tag{2.2.4}$$

with

$$P(\omega) = \frac{1}{N}\left|\sum_{t=0}^{N-1} y(t)e^{-i\omega t}\right|^2, \tag{2.2.5}$$

where $|x|$ denotes the modulus of the scalar x.

Rife & Boorstyn [RB74] proposed a numerical method similar to the ML estimator, which involves a coarse and a fine search. The coarse estimate is obtained by choosing the frequency having the greatest magnitude in the periodogram, as discussed above. A finer estimate is obtained using a method such as the secant method. Generally, zeropadding is required to obtain sufficient resolution when using the FFT, requiring $\mathcal{O}(N' \log_2 N')$ operations, where N' is the size of the desired frequency grid, with typically $N' \gg N$. Thus, the estimator is not computationally efficient. However, it is statistically efficient with the lowest SNR threshold among the variously proposed estimators, exhibiting estimation variance identical to the corresponding CRLB given by [RB74]

$$CRLB_{\hat{\omega}} = \frac{6}{N(N^2-1)\,SNR} \quad (rad/sample)^2, \tag{2.2.6}$$

where $\hat{\omega}$ denotes the estimated frequency and the $CRLB_{\hat{\omega}}$ is the lowest variance which a statistically unbiased estimator may exhibit for a given SNR and N. Over the last decades, the ML estimator's high computation cost has led to a search for alternative methods that approach its statistical performance, but with less computation.

2.2.2 Unweighted Linear Predictor

As suggested in [Tre85], the data model in (2.1.1) can be written as

$$y(t) = [1 + v(t)]\beta e^{i(\omega t+\theta)}, \tag{2.2.7}$$

where

$$v(t) = \beta^{-1} n(t) e^{-i(\omega t+\theta)} \tag{2.2.8}$$

is a complex white sequence. Let $v_r(t)$ and $v_i(t)$ denote the real and the imaginary parts of $v(t)$, respectively. Then, for high SNR,

$$1 + v(t) \approx e^{i \arctan v_i(t)} \approx e^{i v_i(t)}, \tag{2.2.9}$$

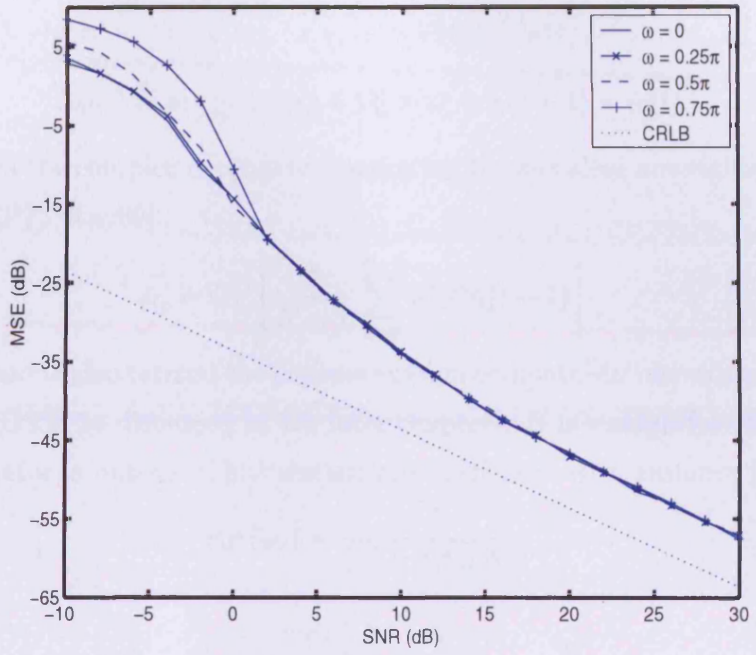

Figure 2.1. The MSE of the UWLP estimator as a function of the SNR, $N = 24$.

allowing the approximation

$$y(t) \approx \beta e^{i\phi(t)}, \tag{2.2.10}$$

where

$$\phi(t) = \omega t + \theta + v_i(t). \tag{2.2.11}$$

Thus, the additive noise has been converted into an equivalent phase noise $v_i(t)$ with variance [Kay89]

$$var(v_i(t)) = \frac{\sigma_n^2}{2\beta^2} = \frac{1}{2\,SNR}. \tag{2.2.12}$$

Most of the recent phase-based approaches exploit this approximation, allowing the phase to be approximately estimated from the difference of the adjacent phase values suggested by

Kay [Kay89], i.e.,

$$\Delta\phi(t) \triangleq \arg\left[y^*(t)y(t+1)\right] \approx \omega + v_i(t+1) - v_i(t), \tag{2.2.13}$$

where $(\cdot)^*$ denotes the complex conjugate, suggesting the so-called unweighted linear predictor (UWLP) [LRP73, Kay89]

$$\hat{\omega}_c = \arg\left[\frac{1}{N-1}\sum_{t=0}^{N-2} y^*(t)y(t+1)\right]. \tag{2.2.14}$$

The UWLP method is also termed the autocorrelation estimator in ultrasound blood velocity estimation [KNKO85], as discussed in the later chapters. It is straightforward to show that the UWLP estimator is unbiased, but statistically inefficient with variance [Kay89, CKQ94]

$$var(\hat{\omega}_c) = \frac{1}{(N-1)^2\, SNR} \tag{2.2.15}$$

giving the ratio

$$\frac{var(\hat{\omega}_c)}{CRLB_{\hat{\omega}}} = \frac{N}{6}. \tag{2.2.16}$$

Figure 2.1 shows the mean square error (MSE) of the UWLP estimator as a function of SNR, with different frequencies denoted by different plots therein. As is clear from the figure, the UWLP method is statistically inefficient for all examined frequencies across the whole SNR range, unable to reach the CRLB. However, given the fact that the UWLP is very simple with very low computational cost, it can be adequate as a coarse estimator, as will be used in our proposed hybrid estimator discussed later.

2.2.3 Kay's Weighted Phase Averager

Another basic computationally efficient estimator discussed here is Kay's weighted phase average (KWPA) method [Kay89]. Recall $\Delta\phi(t)$ in (2.2.13), the KWPA method is expressed as

$$\hat{\omega}_{KWPA} = \sum_{t=0}^{N-2} w(t)\Delta\phi(t), \tag{2.2.17}$$

where $\hat{\omega}_{KWPA}$ denotes the KWPA estimate, and the parabolic window

$$w(t) = \frac{6(t+1)(N-(t+1))}{N(N^2-1)}. \tag{2.2.18}$$

The approximation in (2.2.13) will hold for a very high SNR ($SNR \gg 1$) following the approximation in (2.2.9) and (2.2.10). For this condition $\hat{\omega}_{KWPA}$ can be shown to be an unbiased estimator following the derivation below

$$\begin{aligned} E\{\hat{\omega}_{KWPA}\} &= \sum_{t=0}^{N-2} w(t) E\{\Delta\phi(t)\} \\ &= \sum_{t=0}^{N-2} w(t) E\{\Delta\phi(t)\} \\ &\approx \sum_{t=0}^{N-2} w(t) E\{\omega + v_i(t+1) - v_i(t)\} \\ &= \omega \sum_{t=0}^{N-2} w(t) \\ &= \omega \end{aligned} \tag{2.2.19}$$

where the last equality follows from

$$\sum_{t=0}^{N-2} w(t) = 1. \tag{2.2.20}$$

Similarly, as in (2.2.19), the KWPA estimator, for high SNR, can be shown to have the following variance [Kay89]

$$var(\hat{\omega}_{KWPA}) = \frac{6}{N(N^2-1)\,SNR} \tag{2.2.21}$$

which is identical to the CRLB in (2.2.6). As discussed earlier, the KWPA method is in general biased and (2.2.21) will only hold true for high SNR and very low frequency range [CKQ94, LW92, Qui00].

It has been shown that one of the drawbacks of the KWPA method is the unavoidable wrapping errors when the phase ω approaches $-\pi/+\pi$, making the SNR threshold dependent on underlying frequency [FJ99]. This is because the cumulative errors from noise component $v_i(t)$ will sometimes make the estimate lower than ω and sometimes higher than ω. If $\Delta\phi(t)$ exceeds $-\pi/+\pi$, then it gets wrapped over the $-\pi/+\pi$ boundary and thus aliasing occurs resulting in higher variance as shown in Figure 2.2. Another drawback of the KWPA method is that its performance highly depends on SNR [Kay89]. When the SNR drops below a certain threshold as shown in Figure 2.2, the performance of the KWPA method falls off rapidly, exhibiting threshold behavior at a higher SNR which is also confirmed in Figure 2.2. Also, unlike the ML method, as the data length N increases, the SNR threshold of the KWPA method slowly increases [LM89], which is illustrated in Figure 2.3. As Kay pointed out [Kay89], the coefficients of the parabolic window are responsible for $\hat{\omega}_{KWPA}$ attaining the CRLB. If we let

$$w(t) = \frac{1}{N-1}, \tag{2.2.22}$$

then (2.2.17) becomes

$$\begin{aligned}\hat{\omega}_{UWPA} &= \frac{1}{N-1}\sum_{t=0}^{N-2}\Delta\phi(t) \\ &= \frac{1}{N-1}\left[\phi(N-1)-\phi(0)\right] \\ &= \omega + \frac{1}{N-1}\left[v_i(N-1)-v_i(0)\right]\end{aligned} \tag{2.2.23}$$

which is termed the unweighted phase average (UWPA) estimator and is unbiased, but again becomes inefficient statistically as shown in Figure 2.4. This is because the UWPA estimator in (2.2.23) discards useful information by allowing common information in adjacent terms of the sum to cancel. This is the direct result of ignoring the colouring in the noise term $v_i(t+1)-v_i(t)$ in (2.2.13).

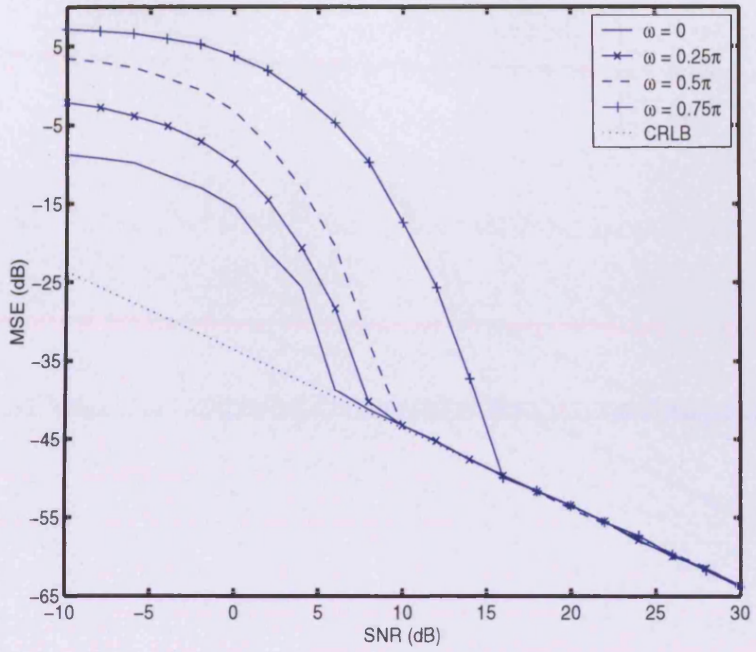

Figure 2.2. The MSE of the examined KWPA estimator as a function of the SNR, $N = 24$.

2.2.4 The Proposed Hybrid Estimator

Given the limitations of the KWPA estimator discussed above, various improved and extended methods have been proposed for reducing the SNR threshold and the frequency dependency of the threshold (see, e.g., [KNC96, Cla92, FJ99, BW02, Mac04], and the references therein). In this section, the proposed hybrid method combines the ideas in [KNC96, FJ99, Mac04] to obtain the performance close to that of ML or ILP, but only requiring $\mathcal{O}(N)$ operations.

As suggested in [Cla92, BW02, Mac04], the UWLP estimate is used to form a downshifted signal, $y_d(t)$, to remove the frequency dependence of the SNR threshold, i.e.,

$$y_d(t) = y(t)e^{-i\hat{\omega}_c t}. \tag{2.2.24}$$

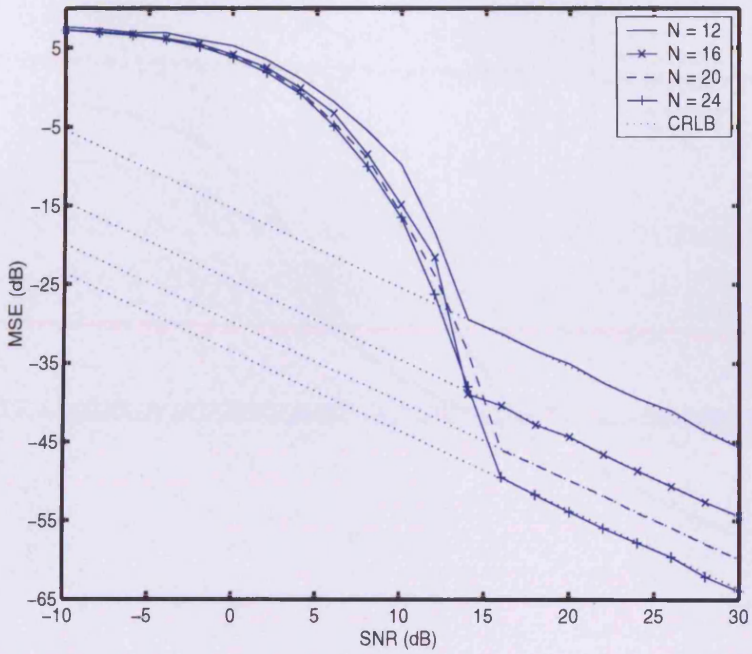

Figure 2.3. The MSE of the examined KWPA estimator as a function of the SNR, $\omega = 0.75\pi$.

In [KNC96], Kim *et al.* proposed using a simple K-tap moving average filter to smooth irregularities and random variations prior to the frequency estimation as a way to reduce the SNR threshold. Such an averaging can be shown to lower the SNR threshold up to $10 \log_{10} K$ dB. However, as such an averaging will severely restrict the allowed frequency range down to $(-\pi/K, \pi/K]$, the method in [KNC96] is limited to signals with frequencies near zero. This is because the finite impulse response (FIR) averaging filter is essentially a low pass filter. Herein, it is noted that the frequency content of the downshifted signal, $y_d(t)$, will satisfy such a restriction, and it is therefore proposed to instead form an averaged

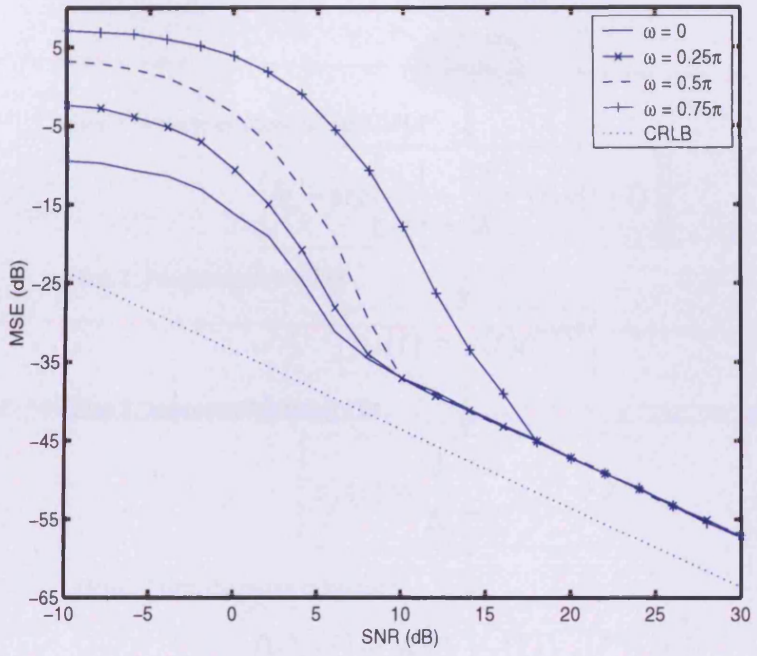

Figure 2.4. The MSE of the examined UWPA estimator as a function of the SNR, $N = 24$.

signal as

$$y_f(t) = \frac{1}{K} \sum_{k=0}^{K-1} y_d(t+k). \tag{2.2.25}$$

Similar to (2.2.13), the adjacent phase difference of (2.2.25) can be formed as

$$\Delta\phi_f(t) = \arg\left[y_f^*(t) y_f(t+1)\right] = \omega_f + u_c(t), \tag{2.2.26}$$

where $u_c(t)$ is given by (2.A.9) for a general K (see Appendix 2.A for further details). It is worth noting that the noise process $u_c(t)$ will now be *coloured* due to the average filtering.

As shown in [LM89], the SNR threshold behavior of the phase-based frequency estimators is affected by cumulative $\pm 2\pi$ phase errors resulting from the effect of the additive noise. This effect can be countered by introducing an outlier detection scheme. Recently, an

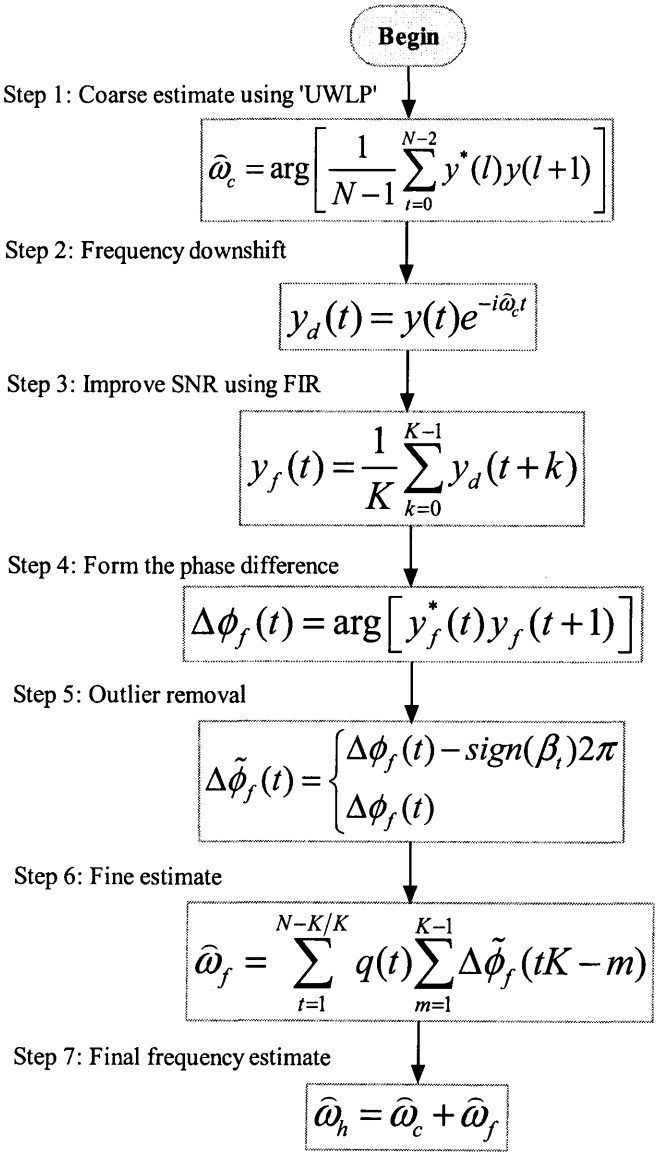

Figure 2.5. Summary of the proposed hybrid estimator.

effective scheme was proposed in [Mac04], where $\pm 2\pi$ outliers are detected if $|\beta_t| > |\beta_{t\pm p}|$ and

$$|\beta_t| > \lambda \tag{2.2.27}$$

with

$$\beta_t = \sum_{p=-P, p\neq 0}^{P} \Delta\phi_f(t-p) \tag{2.2.28}$$

where $\beta_k = \Delta\phi_f(k) = 0$, for $k \in [-P, 1]$ and $k \in [N-K, N-K+P-1]$. Thus, the outliers can be removed as follows

$$\Delta\tilde{\phi}_f(t) = \begin{cases} \Delta\phi_f(t) - \text{sign}(\beta_t)2\pi & \text{if outlier detected} \\ \Delta\phi_f(t) & \text{otherwise} \end{cases} \tag{2.2.29}$$

for $t = 0, \ldots, N-K-1$. Here, λ and P are user parameters, as discussed below. After the SNR threshold reduction using (2.2.25) and (2.2.29), further improvement can be achieved by taking into account the colouration of the noise term in (2.2.26). This can be achieved using the suggested Four Channel Forward Backward (FCFB) method in [FJ99, Fow02], whereby the frequency correction term, $\hat{\omega}_f$, can be found as

$$\hat{\omega}_f = \sum_{t=1}^{(N-K)/K} q(t) \sum_{m=1}^{K-1} \Delta\tilde{\phi}_f(tK-m), \tag{2.2.30}$$

where

$$q(t) = \frac{6tK(N-tK)}{N^3 - NK^2}, \tag{2.2.31}$$

with $t = 1, 2, \ldots, (N-K)/K$. As mentioned in [Fow02], it is possible to develop a closed form in (2.2.30) for any value of N, but they consider only the case when N is an integer multiple of K because it leads to an efficient structure for the processing. Combined with the coarse estimate, the hybrid frequency estimate is found as

$$\hat{\omega}_h = \hat{\omega}_c + \hat{\omega}_f. \tag{2.2.32}$$

It is worth noting that the FCFB applies a different set of weights than those used in the KWPA approach.

In summary, the proposed hybrid estimator is found by first forming the downshifted signal in (2.2.24) using the UWLP estimate in (2.2.14). Then, the phase difference of the filtered signal is formed using (2.2.26), followed by the outlier removal scheme in (2.2.29). Finally, the refined frequency estimate is formed as (2.2.32), using (2.2.30). The hybrid estimator is summarized in Figure 2.5. It is worth stressing that the hybrid method differs from previously suggested approaches in that it combines all the above steps; the FCFB method does not include the outlier removal scheme in (2.2.29). Similarly, the method proposed in [Mac04], hereafter termed the outlier removal estimator (ORE), does not include the filtering in (2.2.25). In this chapter and Chapter 6, $K = 6$, $P = 1$ and $\lambda = 4$ will be used in the simulations for the hybrid estimator, which is based on the numerical analysis of the estimator given in Section 2.4.

2.3 Other Issues

The estimators discussed in the previous section deal with one pure sinusoid corrupted by noise as in (2.1.1), without taking into account power damping and frequency spread over time. In this thesis, application to ultrasonics is a major focus and the sinusoidal-type signals encountered typically have non-zero bandwidth making it interesting to examine how robust the proposed estimator is to frequency spread and power damping, both of which are ways to approximate the non-zero bandwidth of tones. In this section, discussion is given on how the proposed hybrid estimator will be affected by these factors. All the corresponding results displayed in this section have been obtained using 10^3 Monte Carlo simulations.

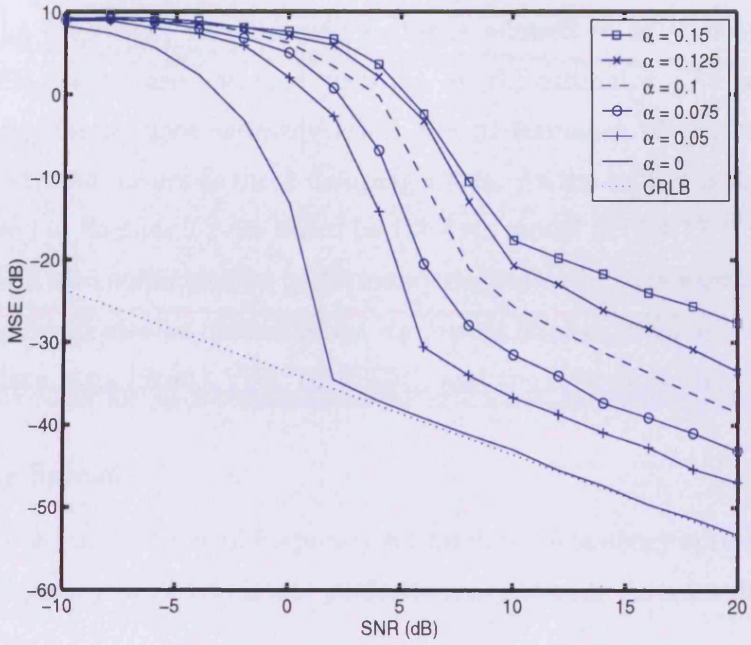

Figure 2.6. The MSE of the Hybrid estimator as a function of SNR with varying damping factor α, for $N = 24$ and $\omega = 0.75\pi$.

2.3.1 Power Damping

Similar to (2.1.1), the observations are modelled as

$$z_d(t) = \tilde{\beta}(t)e^{i(\omega t+\theta)} + n(t), \tag{2.3.1}$$

whilst allowing for a decaying amplitude component

$$\tilde{\beta}(t) = \beta e^{(-\alpha t)} \tag{2.3.2}$$

where $z_d(t)$ denotes the observation sample for $t = 0, \ldots, N-1$, and α the damping factor assumed to be positive, with other definitions as in (2.1.1). To examine the impact on the

performance of the estimator, the damping factor is allowed to vary as shown in Figure 2.6 where the MSE results are obtained with the hybrid estimator. As is clear from the figure, the damping factor does seriously affect the performance of the estimator. More performance degradation occurs as more damping exists. As the hybrid estimator and other estimators discussed in Section 2.2 are based on the data model in (2.1.1), it is expected that other estimators will also suffer similar performance degradation. It is worth noting that the unknown damping could also be estimated by, e.g., using least-squares or forward-backward linear prediction (see, e.g., [Sto93, VSH+00, KK01], and the references therein).

2.3.2 Frequency Spread

Another issue involved in the topic of frequency estimation is frequency spread, which implies that the carrier frequency in (2.1.1) is not perfectly narrowband. As a result, (2.3.1) can be further modified as

$$z_{ds}(t) = \tilde{\beta}(t) \sum_{k=0}^{K} e^{i(\omega t + \delta_k t)} + n(t), \tag{2.3.3}$$

where $z_{ds}(t)$ denotes the observation sample taking into account damping factor denoted by $\tilde{\beta}(t)$ and frequency spread denoted by δ_k. Both factors are assumed to be positive. To examine the impact on the performance of the hybrid estimator as an example, we assume both damping factor and frequency spread existing in the data samples as in (2.3.3) and the corresponding MSE results are shown in Figure 2.7. As is clear from the figure (clockwise from the top left), the MSE of the estimator becomes larger when the damping factor, α, increases; and the performance of the estimator will get worse as the damping factor rises to some level, say $\alpha = 0.1$ as shown in the sub-figure on the bottom left, no matter if the frequency spread exists or not. On the other hand, for any examined power damping factor, the MSE of the estimator will change when the frequency spread changes. It is interesting to note from the figure that the MSEs corresponding to the frequency spreads denoted by δ_{n1}

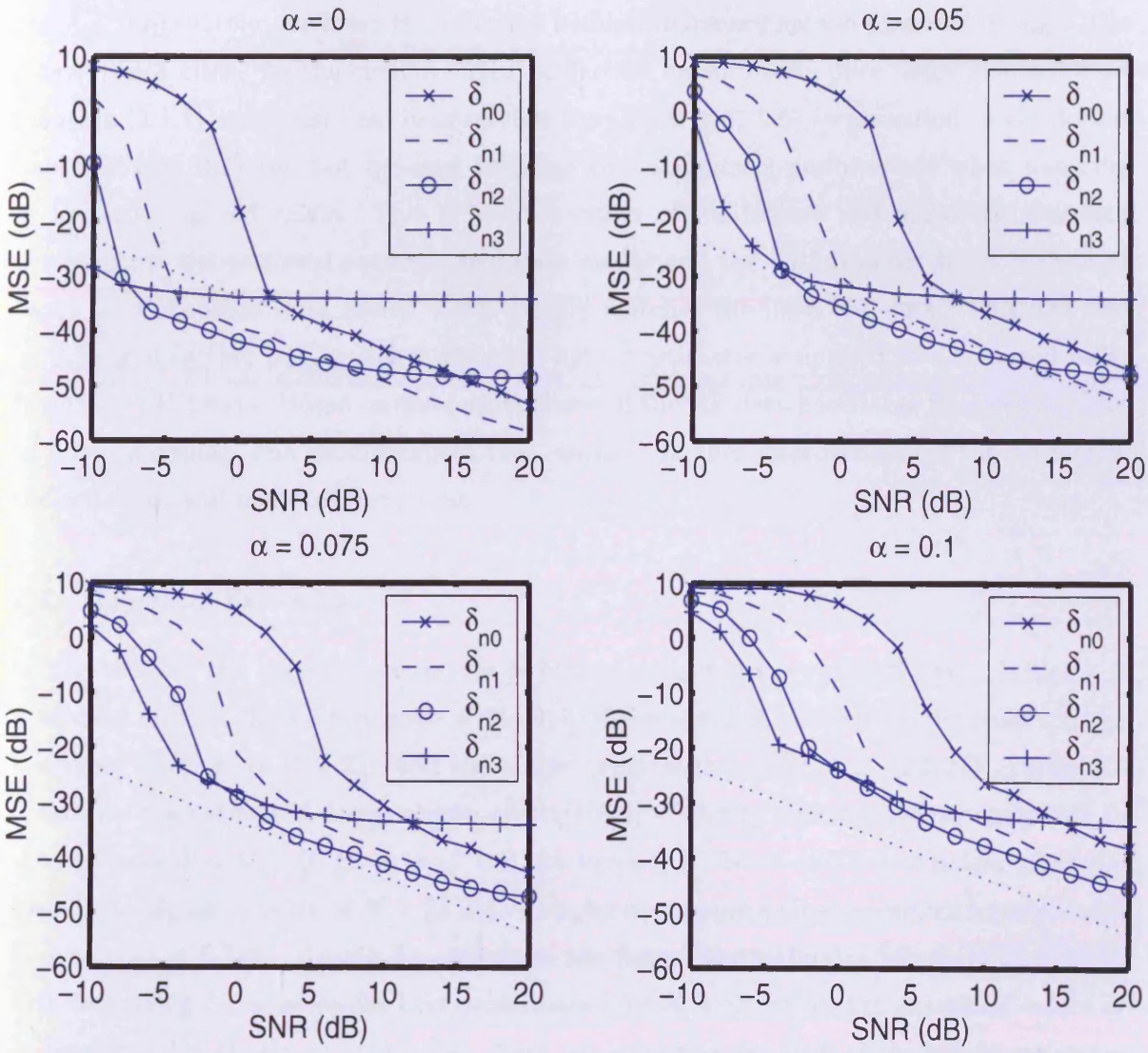

Figure 2.7. The MSE of the proposed hybrid estimator as a function of the SNR, with varying δ in each sub-figure, for $\omega = 0.75\pi$. δ_{n0} means no spread exists; δ_{n1} means spread exists with $\delta_1 = 1e^{-3}$; δ_{n2} means spread exists with $\delta_1 = 1e^{-3}$ and $\delta_2 = 1e^{-2}$; δ_{n3} means spread exists with $\delta_1 = 1e^{-3}$, $\delta_2 = 1e^{-2}$ and $\delta_3 = 0.1$.

and δ_{n2}, respectively, are lower than the one without frequency spread (denoted by δ_{n0}). The reason is not clear. As the current CRLB is derived based on the pure single sinusoid data model in (2.1.1), one must bear in mind that the CRLB in (2.2.6) (represented by the dotted line in Figure 2.7) can not be used to judge the estimator's performance when damping or frequency spread exists. This is because either of the factors will make the real data deviate from the assumed pure sinusoid data model and the CRLB needs to be re-derived based on a modified data model which closely matches the observed data. This will also be discussed further in Chapter 5 when the hybrid estimator is applied to ultrasound radio frequency (RF) data. Based on the results above, if the RF data have large frequency spread or power damping, one should expect that, without further improvement of the estimator, the estimator will not work very well.

2.4 Numerical Examples

In this section, the proposed estimator is first examined with synthetic data. Initially, it is studied on how the performance of the hybrid estimator is affected by the length of the averaging filter, K in (2.2.25), and the outlier removal threshold, λ in (2.2.27). Figure 2.8 illustrates the estimated mean square error (MSE) of the hybrid method as compared to the corresponding CRLB, given in (2.2.6), for varying K. Here, and below unless otherwise stated, the signal consists of $N = 24$ data samples containing a single complex sinusoid with frequency $\omega = 0.75\pi$. As can be seen from the figure, the estimator improves to a point with increasing K, showing its best performance for $K = 6$, for all the examined values of λ. Here $P = 1$ is chosen as in [Mac04]. Next, we examined the MSE of the hybrid estimator for varying P. Figure 2.9 demonstrates the performance as compared to the corresponding CRLB. The results imply that the hybrid estimator shows its best performance for $P = 1$. Furthermore, Figure 2.10 shows the MSE for varying λ, for $K = 6$ and $P = 1$. As can be

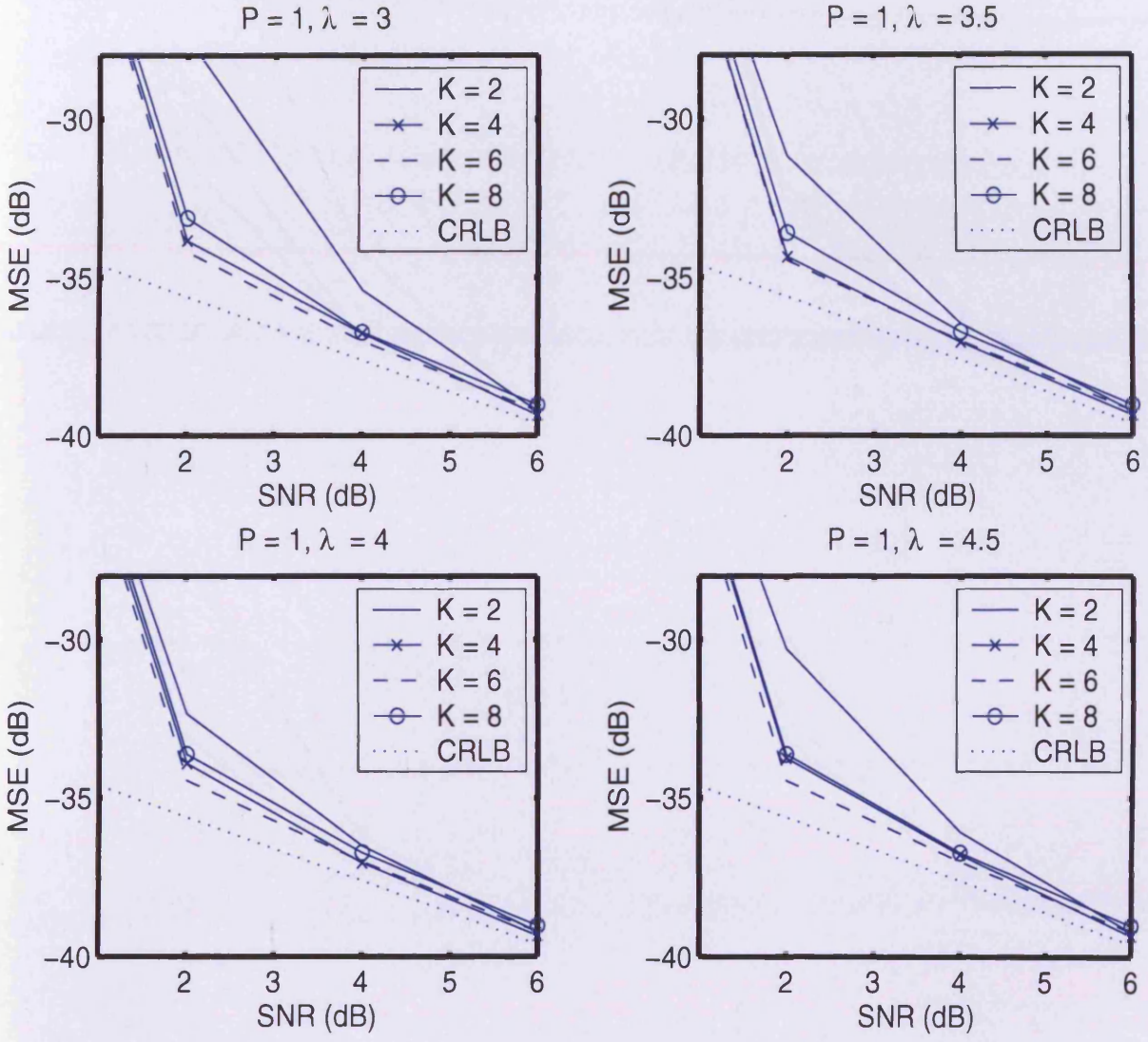

Figure 2.8. The MSE of the proposed hybrid estimator as a function of the SNR, with varying K, for $\omega = 0.75\pi$.

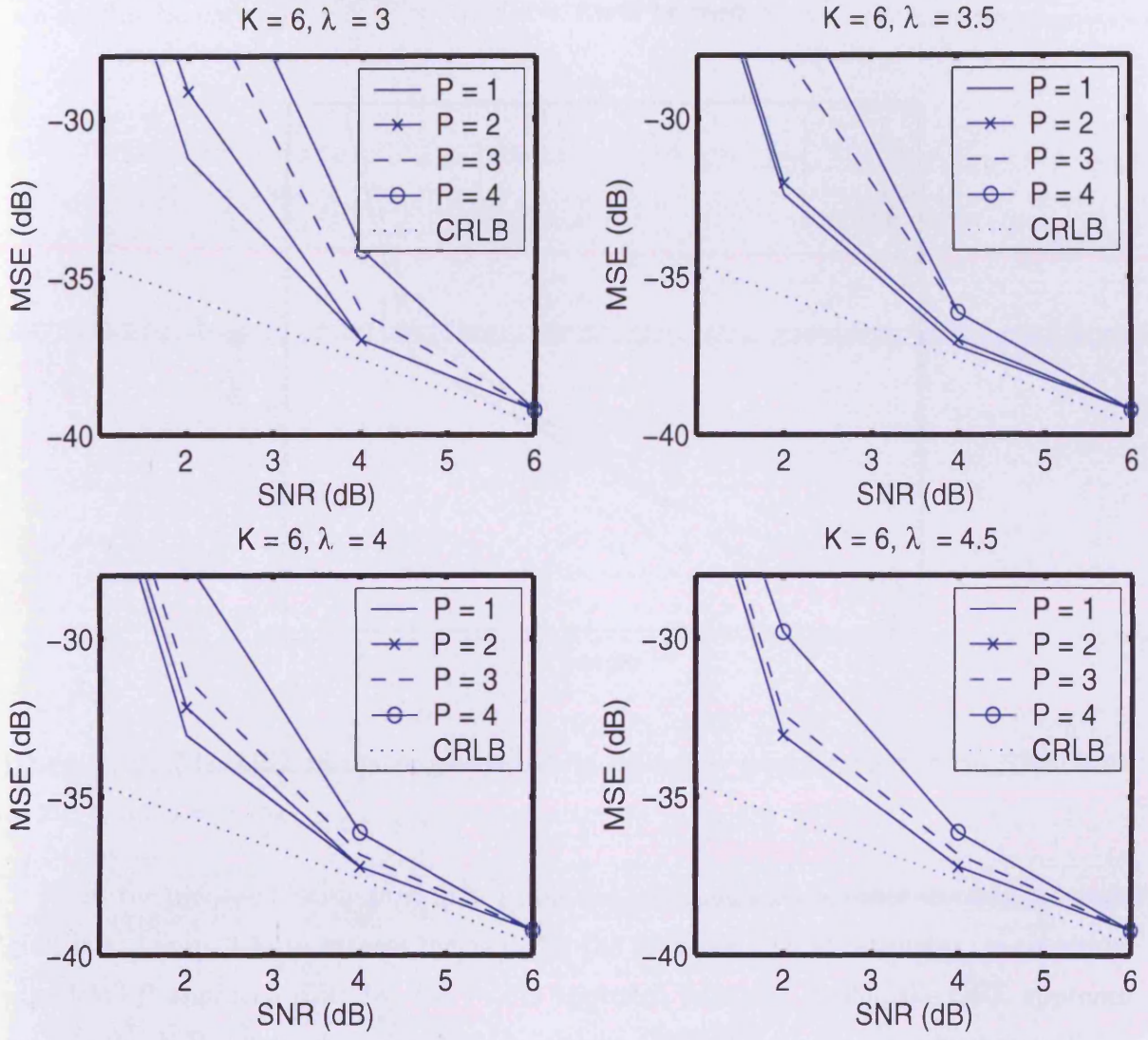

Figure 2.9. The MSE of the proposed hybrid estimator as a function of the SNR, with varying P, for $\omega = 0.75\pi$.

seen from the figure, the method achieves similar performance as soon as $\lambda > 3$. Based on these results, hereafter $K = 6$, $P = 1$ and $\lambda = 4$ will be used.

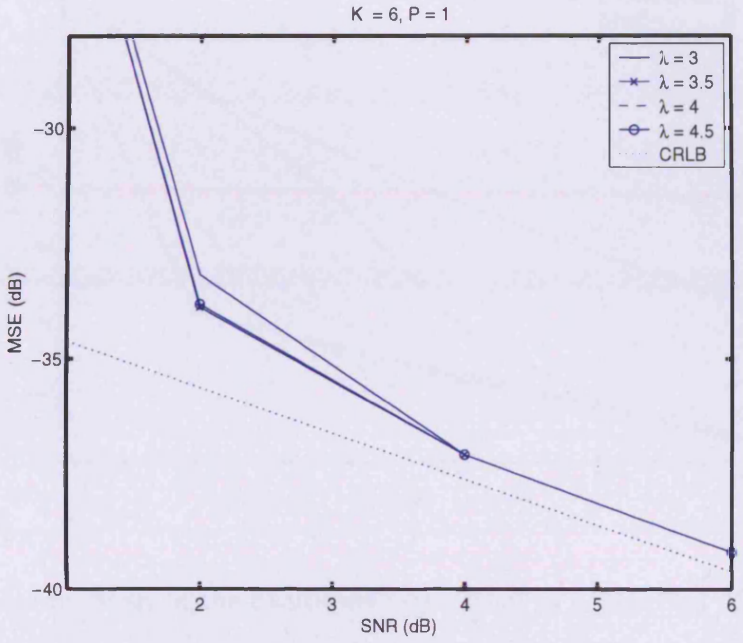

Figure 2.10. The MSE of the proposed hybrid estimator as a function of the SNR, with varying λ, for $\omega = 0.75\pi$.

Next, the proposed estimator will be examined and compared to other recently proposed algorithms. Figure 2.11 illustrates the MSE for the proposed hybrid estimator, as compared to the UWLP approach [LRP73], the FCFB approach following [FJ99], the ORE approach [Mac04], the ILP approach using three iterations [BW02] and the corresponding CRLB as given in [RB74]. As is clear from the figure, the performance of the proposed hybrid estimator is statistically improved, closely following the CRLB at a lower SNR threshold (about 2 dB herein) than the other examined methods. It is noteworthy that the hybrid

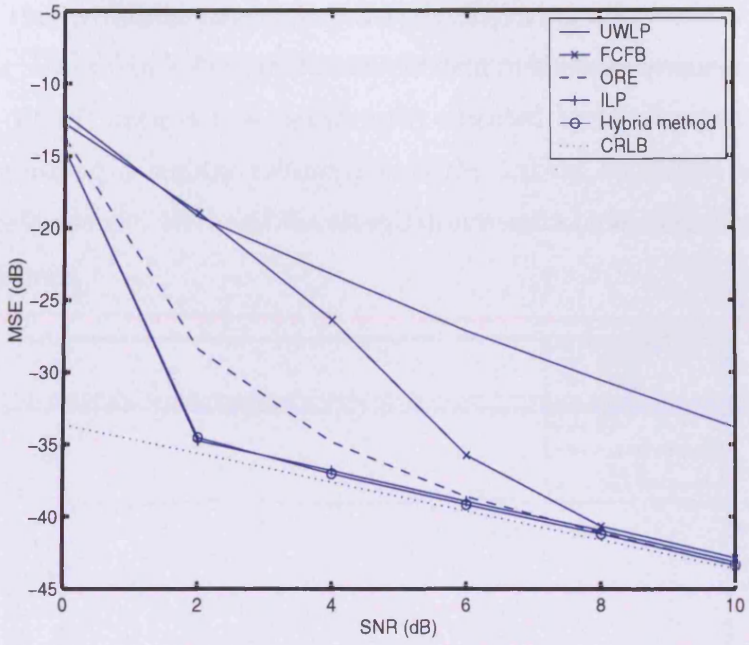

Figure 2.11. The MSE of the examined estimators as a function of the SNR.

estimator shows similar but slightly better performance than the ILP estimator (similar conclusion holds in Figure 2.12 and Figure 2.13); however, the latter requires $\mathcal{O}(N \log_2 N)$ operations, whereas the former only requires $\mathcal{O}(N)$ operations. The hybrid method also uniformly yields a lower MSE than the other methods. It is worth noting that the hybrid estimator suffers some performance degradation due to the introduced averaging in (2.2.25), as pointed out in [KNC96]. This explains why the MSE of the proposed hybrid estimator can not fully reach the CRLB as shown in Figure 2.11 and other figures.

As is well known, the performance of single frequency estimators is often affected by the underlying frequency. Figures 2.12 and 2.13 illustrate how the MSE varies as a function of the frequency of the sinusoid, ω, for $SNR = 6$ dB and $SNR = 4$ dB, respectively. As

seen in the figures, the hybrid estimator is uniformly achieving a lower MSE than the other approaches, and has performance essentially independent of the true frequency. Furthermore, it is clear that the FCFB approach is significantly affected by the frequency, whereas the ORE approach is showing a similar robustness as the hybrid approach, although with a somewhat worse performance. Here, all the simulation results have been obtained using 10^3 Monte Carlo simulations.

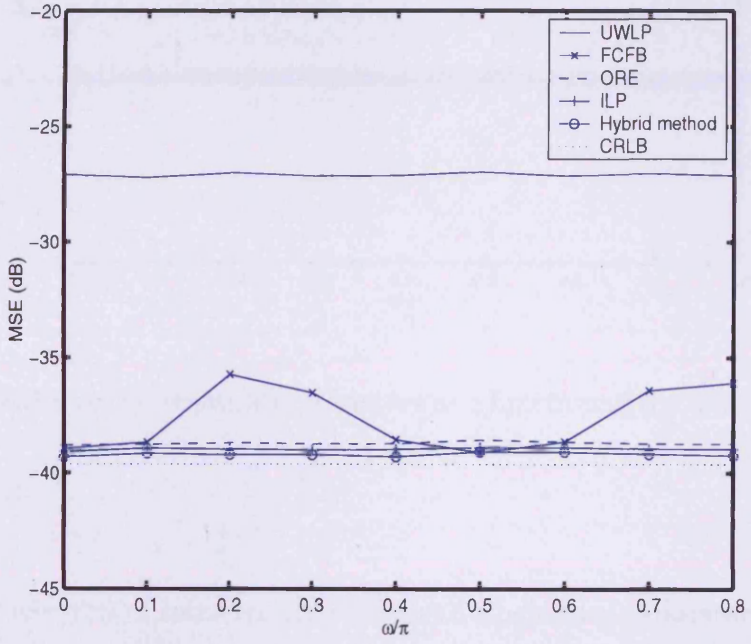

Figure 2.12. The MSE of the examined estimators as a function of the underlying frequency, for SNR = 6 dB.

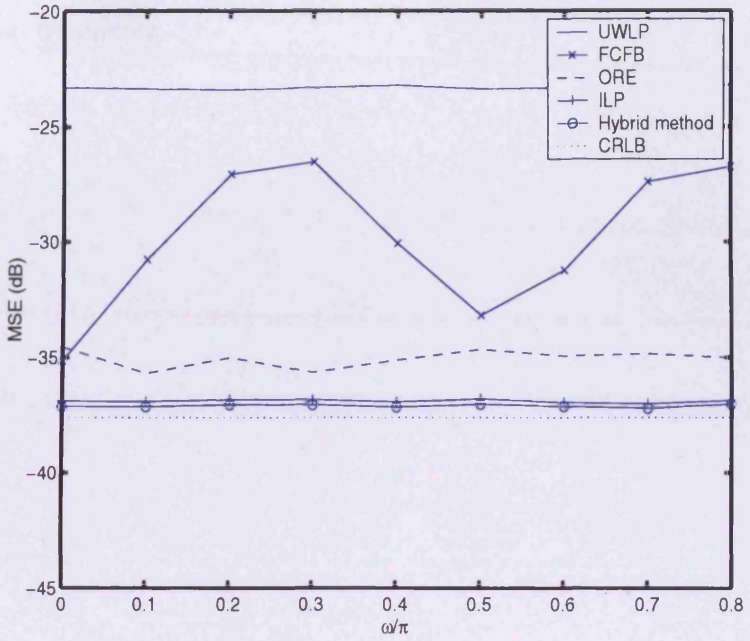

Figure 2.13. The MSE of the examined estimators as a function of the underlying frequency, for SNR = 4 dB.

2.5 Conclusion

In this chapter, an overview of some recently proposed single tone estimators was given first. A low computational complexity hybrid phase-based single frequency estimator combining previously proposed SNR threshold reduction approaches with a recent outlier removal scheme was then proposed. Also, the related issues such as power damping and frequency spread were briefly discussed. Numerical simulations in Section 2.4 indicate that the proposed hybrid estimator achieves a lower mean square error than other available techniques, closely approaching the CRLB at a lower SNR threshold. Furthermore, in contrast to many other techniques, the performance of the hybrid estimator is found to be essentially inde-

pendent of the true frequency.

Appendix

2.A Derivation of the Noise Process in (2.2.26)

In this appendix an expression for the noise process $u_c(t)$, given in (2.2.26), is derived for a general K. Let $\omega_f = \omega - \hat{\omega}_c$, then, using (2.2.7), $y_f(t)$ can be expressed as

$$y_f(t) = \frac{\beta}{K} e^{i\omega_f t + i\theta} \sum_{k=0}^{K-1} \left[1 + v(t+k)\right] e^{i\omega_f k}, \tag{2.A.1}$$

for $t = 0, \ldots, N-K$. Introduce

$$\Psi_K \triangleq \sum_{k=0}^{K-1} e^{i(kK-1)\omega_f/K}, \tag{2.A.2}$$

and

$$\Phi_v^K(t) \triangleq \sum_{k=0}^{K-1} v(t+k) e^{i(kK-1)\omega_f/K}. \tag{2.A.3}$$

Then,

$$\begin{aligned} y_f(t) &= \frac{\beta}{K} e^{i\omega_f t + i\theta + i\omega_f/K} \left[\Psi_K + \Phi_v^K(t)\right] \\ &= \frac{\beta\Psi_K}{K} e^{i\omega_f t + i\theta + i\omega_f/K} \left[1 + \Psi_K^{-1}\Phi_v^K(t)\right] \end{aligned} \tag{2.A.4}$$

Thus, the argument of $y_f(t)$ can be expressed as

$$\begin{aligned} \arg\left[y_f(t)\right] = &\arg\left[\Psi_K\right] + \omega_f t + \theta + \omega_f/K \\ &+ \arg\left[1 + \Psi_K^{-1}\Phi_v^K(t)\right], \end{aligned}$$

implying that the phase difference from adjacent samples, $\Delta\phi_f(t)$, can be expressed as

$$\Delta\phi_f(t) = \omega_f + u_c(t), \tag{2.A.5}$$

where, for $t = 0, \ldots, N - K - 1$,

$$\begin{aligned} u_c(t) &\triangleq \arg\left[1 + \Psi_K^{-1}\Phi_v^K(t+1)\right] \\ &\quad - \arg\left[1 + \Psi_K^{-1}\Phi_v^K(t)\right] \end{aligned} \tag{2.A.6}$$

Then, using the approximation in (2.2.9), (2.A.6) can for high SNR be approximated as

$$u_c(t) \approx \operatorname{Im}\left\{\Psi_K^{-1}\left[\Phi_v^K(t+1) - \Phi_v^K(t)\right]\right\}, \tag{2.A.7}$$

where $\operatorname{Im}\{x\}$ denotes the imaginary part of x. We note that, using a first-order Taylor expansion,

$$\Phi_v^K(t) \approx \sum_{k=0}^{K-1} v(t+k), \tag{2.A.8}$$

as ω_f is small due to the downshifting, implying that

$$u_c(t) \approx \operatorname{Im}\left\{\Psi_K^{-1}\left[v(t+K) - v(t)\right]\right\}. \tag{2.A.9}$$

We note that for $K = 2$, (2.A.9) yields the expression given in [KNC96], i.e.,

$$u_c(t) \approx \frac{v_i(t+2) - v_i(t)}{2\cos(\omega_f/2)}. \tag{2.A.10}$$

Chapter 3

VELOCITY ESTIMATION USING MULTIPLE CARRIERS

Velocity estimation of a moving reflector is an important topic in a wide variety of fields. Typically, this is achieved by estimating the Doppler frequency shift, or equivalent, in the measured signal. Due to aliasing, the resulting velocity estimate will suffer from a limited unambiguous velocity range, which, depending on application, might limit the usability of the estimator. In this chapter, three novel multiple-carrier based velocity estimators are proposed designed such that the velocity range is extended above the Nyquist velocity limit. Furthermore, the CRLB for the velocity estimation is derived to evaluate the performances of the proposed methods. Extensive numerical simulations clearly indicate the extended unambiguous velocity range and the performance gain as compared to other existing methods.

3.1 Introduction

Estimating the velocity of a moving reflector is an important topic in a wide variety of fields such as, for example, blood flow dynamics, radar and sonar. Typically, the velocity is determined by examining the Doppler frequency shift, or equivalent, in the measured signal [Edd93, Wai02, Jen96a]. Such an approach will inherently offer only a limited unambiguous

velocity range due to aliasing, which, depending on the application, might pose a restrictive limitation. Herein, the discussion will mainly focus on the estimation of blood velocities in ultrasound systems, where the unambiguous velocity range will limit the usability of the system; but the developed techniques are general and can easily be applied to other fields. The great majority of commercially available pulsed-wave (PW) medical ultrasound systems use a narrow-band autocorrelation-based velocity estimation technique developed by Kasai *et al.* [KNKO85]. This technique, hereafter termed Kasai's autocorrelation technique (KAT), which is also termed the UWLP estimator [LRP73, Kay89] as discussed in Chapter 2, is both numerically robust and computationally simple [Wel94, AP03], but suffers from a limited unambiguous velocity range. Also, as analyzed in Chapter 2, it is not statistically efficient. The maximum detectable axial velocity using KAT, also called the Nyquist velocity limit here denoted, v_{Nyq}, can be expressed as

$$v_{Nyq} = \frac{cf_{prf}}{4f_c}, \tag{3.1.1}$$

where c denotes the speed of the wave propagation in the tissue, f_c the carrier frequency, and f_{prf} the pulse repetition frequency [Jen96a]. As the maximum depth into the body that can be examined, d_{max}, is determined as [Jen96a]

$$d_{max} = \frac{c}{2f_{prf}}, \tag{3.1.2}$$

it is very difficult to estimate larger velocities in deep vessels, such as in the heart, where the blood velocity can be as high as 10 m/s [BFMT93]. Due to the importance of such estimations, numerous techniques to extend the unambiguous velocity range for ultrasound systems have been proposed in the recent literature [BP86, Tor89, Jen93a, SDM93, Eva93, Wel94, NRB+95, YK99]; with several of these applicable to other fields as well. In principle, the aliasing effect is correctable as the aliasing can be distinguished from the true flow by the absence of any indication of even the briefest period of zero flow [Wel94]. However,

in practice, such an approach typically fails if there are flows in opposite directions simultaneously within the sample volume, as in turbulent flow and an eddy[1]. Another way to overcome the aliasing problem is to use a wideband technique such as the cross-correlation technique presented in [BP86]. Here, the maximum unambiguous velocity is determined by the number of available time lags. However, the width of the blood vessel cross section, the computing capability, or both, eventually limits the number of lags and the maximum measurable velocity [YK99]. Furthermore, high velocities are difficult to obtain unless the cross-correlation search is limited to the main lobe of the correlation function [Jen93a]. Narrowband periodogram-based techniques have also attracted many investigations both in CFI and spectral Doppler over the last decades. The temporal tracking FFT methods have been investigated to detect when the velocity estimates cross the aliasing boundary, then the velocity estimates are corrected accordingly [Tor89]. For CFI, the velocity changes between two successive frames can be large, making temporal tracking impractical [YK99]. Instead, spatial tracking along a scan line (i.e., across a vessel's velocity profile) has been shown to perform well, while it has limitations for laminar flow [SDM93]. If there exists turbulent flow, the bidirectional flow and, as a result, the changeable sign of Doppler shift will mislead the frequency correction mechanism which assumes the frequency rotation is due to frequency beyond the Nyquist limit. Later, a conceptually novel system was proposed in [NRB+95] (hereafter termed NAT), where Nitzpon *et al.* proposed an integrated parallel PW system with two different carrier frequencies (f_1 and f_2) to extend the maximum detectable velocity by a factor of

$$F = \frac{f_1}{f_2 - f_1}. \tag{3.1.3}$$

This technique has been applied to both spectral Doppler and to CFI (the so-called Quasar technique [DGS92]). However, the achieved measurable Doppler signal bandwidth is less

[1]Eddy: in turbulent fluid motion, a blob of the fluid that has some definitive character and moves in some way differently from the main flow.

than f_{prf} and it will not be sufficient to analyze broadband turbulent flow [NRB+95]. In this chapter, three multi-carrier estimation techniques are proposed, extending and refining the idea in [NRB+95] and exploiting the velocity dependence of the backscattered carriers, to yield a subspace-based velocity estimator (SVE), a data adaptive velocity estimator (DAVE) and an NLS estimator. A conventional method developed from an individual carrier will suffer from aliasing and will hence have limited application range. However, as the frequency of each backscattered carrier is determined by the velocity of the reflecting target, the frequency separation between the reflected carriers will uniquely determine the blood velocity without suffering aliasing, and therefore schemes based on multiple carriers potentially have increased operational range.

The remainder of this chapter is organized as follows: in the next section, the signal model is introduced and the SVE, the DAVE and the NLS methods are presented. In Section 3.3, extensive numerical simulations clearly illustrate the performance of the proposed estimators. Finally, Section 3.4 contains the conclusions.

3.2 Estimation Using Multiple Carriers

3.2.1 Signal Model

Consider a transmitted signal, consisting of d complex sinusoidal carriers, which is backscattered from multiple moving reflectors. The received signal can then be well modelled as

$$y(t) = x(t) + w(t), \tag{3.2.1}$$

with

$$x(t) = \sum_{k=1}^{d} \beta_k e^{i\omega_k(v)t}, \tag{3.2.2}$$

and

$$\beta_k = \alpha_k e^{i\varphi_k} \tag{3.2.3}$$

for $t = 0, \ldots, N-1$, where β_k denotes the received complex amplitude of the kth sinusoid, φ_k the initial phase which can be well modelled as independent random variable uniformly distributed on $[-\pi, \pi]$, and $\omega_k(v)$ is the frequency shift of the kth sinusoidal component due to the (axial) velocity, v, of the reflecting scatterer. Furthermore, $w(t)$ is additive white Gaussian noise with $w(t) \sim N(0, \sigma^2)$, which is due to reflections from other scatterers as well as thermal and measurement noises. In the following, the frequency shifting function, $\omega_k(v)$, is assumed *known*, whereas the received sinusoidal amplitudes, β_k, as well as the velocity of the reflecting scatterer, v, are *unknown*. Depending on application, different frequency distorting functions can be considered. The multiple carrier frequency-based estimators proposed here are targetted at the application of blood velocity estimation, but it is noteworthy that these estimators can be easily applied to related problems in radar and sonar. In the estimation of blood velocities using ultrasound the angular frequency distorting function can be written as [Jen96a]

$$\omega_k(v) = 2\pi \frac{2v f_{c_k}}{c}, \tag{3.2.4}$$

where f_{c_k} is the kth carrier frequency in emission.

3.2.2 The Subspace-based Velocity Estimator

In this section, the proposed subspace-based velocity estimator is outlined. Let

$$\begin{aligned} \mathbf{y}_L(t) &\triangleq \left[\begin{array}{ccc} y(t) & \ldots & y(t+L-1) \end{array} \right]^T \\ &= \mathbf{A}_L(v)\mathbf{\Phi}_v(t)\boldsymbol{\beta} + \mathbf{w}_L(t), \end{aligned} \tag{3.2.5}$$

for $t = 0, \ldots, M = N - L$ with $L > d$, where $(\cdot)^T$ denotes the transpose operation, $\mathbf{w}_L(t)$ is defined similar to $\mathbf{y}_L(t)$, and

$$\mathbf{A}_L(v) = \left[\begin{array}{ccc} \mathbf{a}_{L,1}(v) & \ldots & \mathbf{a}_{L,d}(v) \end{array} \right], \tag{3.2.6}$$

$$\mathbf{a}_{L,k}(v) = \left[\begin{array}{cccc} 1 & e^{i\omega_k(v)} & \ldots & e^{i(L-1)\omega_k(v)} \end{array} \right]^T \tag{3.2.7}$$

with

$$\mathbf{\Phi}_v(t) = \begin{bmatrix} e^{it\omega_1(v)} & & \mathbf{0} \\ & \ddots & \\ \mathbf{0} & & e^{it\omega_d(v)} \end{bmatrix}, \tag{3.2.8}$$

$$\boldsymbol{\beta} = \begin{bmatrix} \beta_1 & \dots & \beta_d \end{bmatrix}^T. \tag{3.2.9}$$

The length of the filters, $L < N/2$, is a user parameter affecting the resolution and variance of the resulting estimator; a large L will yield high resolution estimates with high variance, whereas a small L will yield low resolution estimates with low variance. As the subspace-based velocity estimator proposed here is based on the fact that the eigen-structure of the covariance matrix of the data contains complete information on the frequencies $\{\omega_k(v)\}$ [SM05], the data covariance matrix is formed as

$$\mathbf{R}_y \triangleq E\{\mathbf{y}_L(t)\mathbf{y}_L{}^H(t)\} = \mathbf{A}_L(v)\mathbf{P}\mathbf{A}_L^H(v) + \sigma^2\mathbf{I}, \tag{3.2.10}$$

where $E\{\cdot\}$ denotes statistical expectation, $(\cdot)^H$ the conjugate transpose (Hermitian) operation and $\mathbf{I}$ the $L \times L$ identity matrix. As $\beta_k = \alpha_k e^{i\varphi_k}$, $\mathbf{P}$ can be simplified as

$$\mathbf{P} = E\{\mathbf{\Phi}_v(t)\boldsymbol{\beta}\boldsymbol{\beta}^H\mathbf{\Phi}_v^H(t)\} = \text{diag}\left\{\begin{bmatrix} \alpha_1^2 & \dots & \alpha_d^2 \end{bmatrix}\right\}, \tag{3.2.11}$$

where $\text{diag}\{\mathbf{x}\}$ denotes the diagonal matrix whose non-zero elements are the elements of the vector $\mathbf{x}$. The derivation of (3.2.11) is given in Appendix 3.A.

As $\mathbf{R}_y$ is typically unknown, a consistent sample estimate $\hat{\mathbf{R}}_y^f$ should be used in place of $\mathbf{R}_y$. Such an estimate can be obtained as

$$\hat{\mathbf{R}}_y^f = \frac{1}{M}\sum_{t=0}^{M} \mathbf{y}_L(t)\mathbf{y}_L^H(t). \tag{3.2.12}$$

Furthermore, it is often preferable to use forward-backward averaging to eliminate sensitivity to initial phase to obtain such an estimate [SM05], forming the estimated correlation matrix

as

$$\hat{\mathbf{R}}_y = \frac{1}{2}\left(\hat{\mathbf{R}}_y^f + \mathbf{J}\hat{\mathbf{R}}_y^{fT}\mathbf{J}\right), \tag{3.2.13}$$

where $\mathbf{J}$ is the $L \times L$ exchange matrix

$$\mathbf{J} = \begin{bmatrix} 0 & & 1 \\ & \iddots & \\ 1 & & 0 \end{bmatrix}. \tag{3.2.14}$$

Note that $\hat{\mathbf{R}}_y$ can be decomposed as

$$\hat{\mathbf{R}}_y = \hat{\mathbf{U}}\hat{\mathbf{\Lambda}}\hat{\mathbf{U}}^H, \tag{3.2.15}$$

where $\hat{\mathbf{U}}$ contains the eigenvectors and $\hat{\mathbf{\Lambda}}$ is a diagonal matrix with the corresponding eigenvalues nonincreasingly lying along the diagonal. As a result, the underlying velocity can be obtained as

$$\hat{v} = \arg\min_v \|\mathbf{A}_L^H(v)\hat{\mathbf{G}}\|_F^2 \tag{3.2.16}$$

where $\|\cdot\|_F$ denotes the Frobenius norm and $\hat{\mathbf{G}}$ the noise subspace of $\hat{\mathbf{R}}_y$, spanned by the last $L-d$ columns of $\hat{\mathbf{U}}$. The proof of (3.2.16) is given in Appendix 3.B. Thus, by evaluating (3.2.16) for a range of velocities of interest, $v \in [v_{min}, v_{max}]$, the velocity of the reflecting scatterer can be estimated as the velocity minimizing $\|\mathbf{A}_L(v)^H\hat{\mathbf{G}}\|_F^2$, which is termed the *subspace-based velocity estimator* (SVE). As the columns of $\mathbf{A}_L(v)$ and $\hat{\mathbf{G}}$ span the signal subspace and the noise subspace, implying $\mathbf{A}_L^H(v)\hat{\mathbf{G}} = \mathbf{0}$ as in (3.B.6), thus $trace\{\mathbf{A}_L^H(v)\hat{\mathbf{G}}\hat{\mathbf{G}}^H\mathbf{A}_L(v)\}$ can be seen as a good approximation of $\|\mathbf{A}_L^H(v)\hat{\mathbf{G}}\|_F^2$. As a result, alternatively, a good approximation of $\hat{v}$ in (3.2.16) can be written as the location of the peak of the following function

$$\hat{v} = \arg\max_v \frac{1}{trace\{\mathbf{A}_L^H(v)\hat{\mathbf{G}}\hat{\mathbf{G}}^H\mathbf{A}_L(v)\}} \tag{3.2.17}$$

where $trace\{\mathbf{X}\}$ denotes the trace of matrix $\mathbf{X}$.

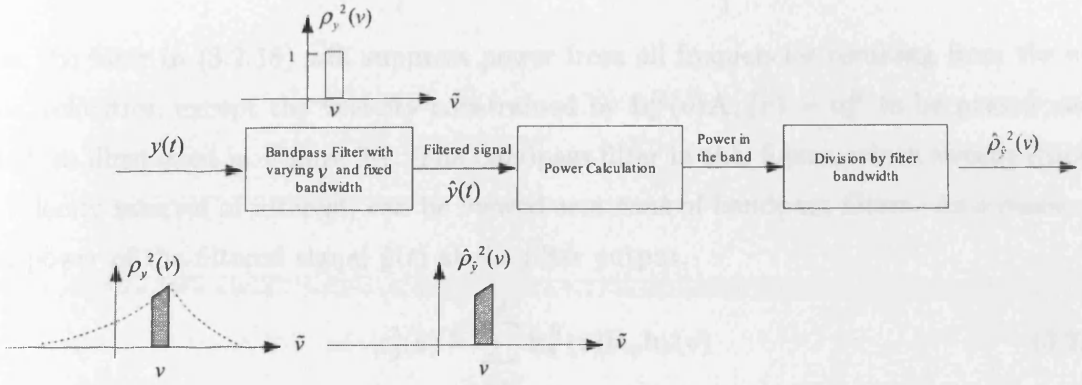

Figure 3.1. The filter bank approach to velocity spectrum estimation.

3.2.3 The Data Adaptive Velocity Estimator

In this section, a non-parametric filterbank velocity estimator is formulated allowing the additive noise process, $w(t)$, to be modelled as an unknown zero mean colored noise process. By constructing a set of L-tap data adaptive bandpass FIR filters, each centered at a particular velocity v, one may estimate the so-called *velocity spectrum*, $\rho_y^2(v)$, creating a representation of how well a particular velocity is represented in the data set. Herein, a set of L-tap data adaptive finite impulse response (FIR) filters is designed, $\mathbf{h}_k(v)$, for $k = 1, \ldots, d$, each centered at a given common velocity v designed such that

$$\mathbf{h}_k(v) = \arg\min_{\mathbf{h}_k(v)} \mathbf{h}_k^H(v)\mathbf{R}_y\mathbf{h}_k(v) \quad \text{subject to} \quad \mathbf{h}_k^H(v)\mathbf{A}_L(v) = \mathbf{u}_k^T \quad \text{for} \quad k = 1, \ldots, d \tag{3.2.18}$$

where $\mathbf{u}_k$ is the signature vector with a one at position k, and zeros elsewhere, i.e.,

$$\mathbf{u}_k = \begin{bmatrix} 0 & \dots & 0 & 1 & 0 & \dots & 0 \end{bmatrix}^T. \tag{3.2.19}$$

Thus, the filter in (3.2.18) will suppress power from all frequencies resulting from the evaluated velocities, except the velocity constrained by $\mathbf{h}_k^H(v)\mathbf{A}_L(v) = \mathbf{u}_k^H$ to be passed undistorted, as illustrated in Figure 3.1. The bandpass filter in this figure, which sweeps through the velocity interval of interest, can be viewed as a *bank* of bandpass filters. As a result, the total power of the filtered signal $\hat{y}(t)$ at the filter output,

$$\rho_{\hat{y}}^2(v) \triangleq \sum_{k=1}^{d} \mathbf{h}_k^H(v)\mathbf{R}_y\mathbf{h}_k(v) \tag{3.2.20}$$

will mainly be from the d sinusoidal components resulting from the underlying velocity v. By examining the velocity spectrum $\rho_{\hat{y}}^2(v)$, then the peak of the spectrum will correspond to the underlying velocity as illustrated in Figure 3.1. It is noteworthy that the filter minimizing (3.2.18), is obtained as (please refer to Appendix 3.C for the proof; also see, e.g., [SM05])

$$\mathbf{h}_k(v) = \mathbf{R}_y^{-1}\mathbf{A}_L(v)\left(\mathbf{A}_L^H(v)\mathbf{R}_y^{-1}\mathbf{A}_L(v)\right)^{-1}\mathbf{u}_k \tag{3.2.21}$$

Substituting (3.2.21) into (3.2.20), and using (3.2.13) to replace $\mathbf{R}_y$, then we have

$$\hat{\rho}_{\hat{y}}^2(v) = \sum_{k=1}^{d} \mathbf{u}_k^T\left(\mathbf{A}_L^H(v)\hat{\mathbf{R}}_y^{-1}\mathbf{A}_L(v)\right)^{-1}\mathbf{u}_k, \tag{3.2.22}$$

leading to the velocity estimation as

$$\hat{v} = \arg\max_v \hat{\rho}_{\hat{y}}^2(v) \tag{3.2.23}$$

which is termed as the *data adaptive velocity estimator* (DAVE). It is worth highlighting that the inversion of matrix $\mathbf{A}_L^H(v)\hat{\mathbf{R}}_y^{-1}\mathbf{A}_L(v)$ in (3.2.22) may be poorly conditioned for some specific v due to the resulting closely spaced frequency components. To alleviate this problem, a low rank approximation technique is employed as outlined in Appendix 3.D.

3.2.4 The Nonlinear Least Squares Estimator

Next, (3.2.1) is written as

$$\mathbf{y}_N = \mathbf{x} + \mathbf{w}_N, \tag{3.2.24}$$

with

$$\mathbf{x} = \mathbf{A}_N(v)\boldsymbol{\beta} = [x(0), \cdots, x(N-1)]^T, \tag{3.2.25}$$

where

$$\mathbf{y}_N = \begin{bmatrix} y(0) & \cdots & y(N-1) \end{bmatrix}^T. \tag{3.2.26}$$

Here, $\mathbf{A}_N(v)$ and $\mathbf{w}_N$ are respectively defined similar to $\mathbf{A}_L(v)$ and $\mathbf{y}_N$. The NLS estimate of v is obtained as

$$\hat{v} = \arg\min_{\boldsymbol{\beta},v} \| \mathbf{y}_N - \mathbf{A}_N(v)\boldsymbol{\beta} \|_F^2. \tag{3.2.27}$$

Let $f = \|\mathbf{y}_N - \mathbf{A}_N(v)\boldsymbol{\beta}\|_F^2$ and $\boldsymbol{\Psi}(v) = \mathbf{A}_N^H(v)\mathbf{A}_N(v)$, and note that f can be written as [SM05]

$$\begin{aligned} f = \left[\boldsymbol{\beta} - \boldsymbol{\Psi}^{-1}(v)\mathbf{A}_N^H(v)\mathbf{y}_N\right]^H \boldsymbol{\Psi}(v) \left[\boldsymbol{\beta} - \boldsymbol{\Psi}^{-1}(v)\mathbf{A}_N^H(v)\mathbf{y}_N\right] + \\ \mathbf{y}_N^H\mathbf{y}_N - \mathbf{y}_N^H\mathbf{A}_N(v)\boldsymbol{\Psi}^{-1}(v)\mathbf{A}_N^H(v)\mathbf{y}_N. \end{aligned} \tag{3.2.28}$$

This yields the least-squares estimate of $\boldsymbol{\beta}$ as

$$\hat{\boldsymbol{\beta}} = \left(\mathbf{A}_N^H(v)\mathbf{A}_N(v)\right)^{-1}\mathbf{A}_N^H(v)\mathbf{y}_N, \tag{3.2.29}$$

which inserted into (3.2.27) yields the minimization

$$\hat{v} = \arg\min_{v} \| \boldsymbol{\Pi}^{\perp}_{\mathbf{A}_N(v)}\mathbf{y}_N \|_F^2 \tag{3.2.30}$$

with

$$\begin{aligned} \boldsymbol{\Pi}^{\perp}_{\mathbf{A}_N(v)} &\triangleq \mathbf{I} - \boldsymbol{\Pi}_{\mathbf{A}_N(v)} \\ &= \mathbf{I} - \mathbf{A}_N(v)\left(\mathbf{A}_N^H(v)\mathbf{A}_N(v)\right)^{-1}\mathbf{A}_N^H(v). \end{aligned} \tag{3.2.31}$$

Minimizing (3.2.27) for the general case of d unknown frequencies results in a d-dimensional search. By noting that each frequency component will be distorted by a common known frequency distorting function as given in (3.2.4), the minimization with respect to v can be obtained by a simple one-dimensional search. Equivalently, one can estimate v as

$$\hat{v} = \arg\max_{v} \|\mathbf{A}_N(v) \left(\mathbf{A}_N^H(v)\mathbf{A}_N(v)\right)^{-1} \mathbf{A}_N^H(v)\mathbf{y}_N\|_F^2. \tag{3.2.32}$$

Again, it reminds us that the inversion of matrix $\left(\mathbf{A}_N^H(v)\mathbf{A}_N(v)\right)^{-1}$ in (3.2.31) may be poorly conditioned for some specific v due to the resulting closely spaced frequency components. To alleviate this problem, a low rank approximation technique is employed similar to the one outlined in Appendix 3.D.

3.3 Numerical examples

To examine the performances and the abilities of extending the unambiguous velocity range, the performance of the proposed estimators is examined in a simplified scenario. In the following simulations, no clutter component is assumed in the simulated data and, as a result, no clutter rejection operation is employed in the processing. Herein, a single reflecting scatterer moving towards the transmitter with velocity v is assumed, and a carrier consisting of $d = 2$ sinusoids with absolute frequencies, $f_1 = 0.081$ and $f_2 = 0.1197$, is considered. The received signal is assumed to be corrupted by zero mean circular white Gaussian noise $w(t)$. Let the signal to noise ratio (SNR) be calculated as

$$SNR = 10\log_{10}\frac{\sigma_x^2}{\sigma^2}, \tag{3.3.1}$$

with $\sigma_x^2 = E\{\mathbf{x}^H\mathbf{x}\}$ and σ^2 the variance of $w(t)$.

Initially, the details of the velocity spectra of the proposed estimators with data samples $N = 20$ are studied. The velocity spectra of the SVE, the DAVE and the NLS method are

defined in (3.2.17), (3.2.23) and (3.2.32), respectively. Figure 3.2 shows the velocity spectra of the proposed methods with varying SNR for true velocity $v = 2v_{Nyq}$. For very low SNR, all the methods have difficulty in locating the true velocity as shown in Figure 3.2 (a), which is not surprising. As the SNR increases, the side lobes of the spectra decrease and all the proposed methods exhibit their ability to find the true velocity which corresponds to the main peak in the corresponding plot in the figure. It is worth noting that, even for high SNR, a comparable peak to the main peak in the spectrum occurs at location where $v = -2v_{Nyq}$, likely resulting in some outliers in estimation. To further explore this, the proposed estimators are examined for varying velocity with $SNR = 10$ dB. The corresponding velocity spectra are shown in Figure 3.3. As can be seen, for velocity unequal to integer multiples of the Nyquist velocity v_{Nyq}, the spectrum of each proposed method only contains one distinct peak which correctly locates the underlying true velocity, as for the cases in Figure 3.3 (b) and (d) where the true velocity $v = 1.5v_{Nyq}$ and $v = 2.5v_{Nyq}$, respectively. On the other hand, for velocity equal to integer multiples of v_{Nyq} as in Figure 3.3 (a) and (c), a similar conclusion holds as in Figure 3.2 in terms of the second peak likely misleading the estimation. Based on the finding above, in the later simulations, a third order median filter is employed to suppress the possible outliers.

In the rest of this section, the proposed methods are examined statistically and their performances are compared to the existing methods, NAT and KAT. Figure 3.4 shows the mean square errors (MSE) of the proposed three estimators and the NAT method as a function of SNR. To allow for the best possible performance of the NAT method, *ideal* (not realizable) filters have been assumed to separate the carriers, f_1 and f_2. If non-ideal filters are used, the performance of the NAT method will be significantly worse. It is noteworthy that no details of the used filters are given in [NRB+95]. In the figure, the performance is compared to the corresponding CRLB derived in Appendix 3.E. Here, $v = 2\,v_{Nyq}$, $v_{Nyq} = 0.385$ m/s and $N = 20$. It is clear from the figure that all the proposed methods exhibit low MSE

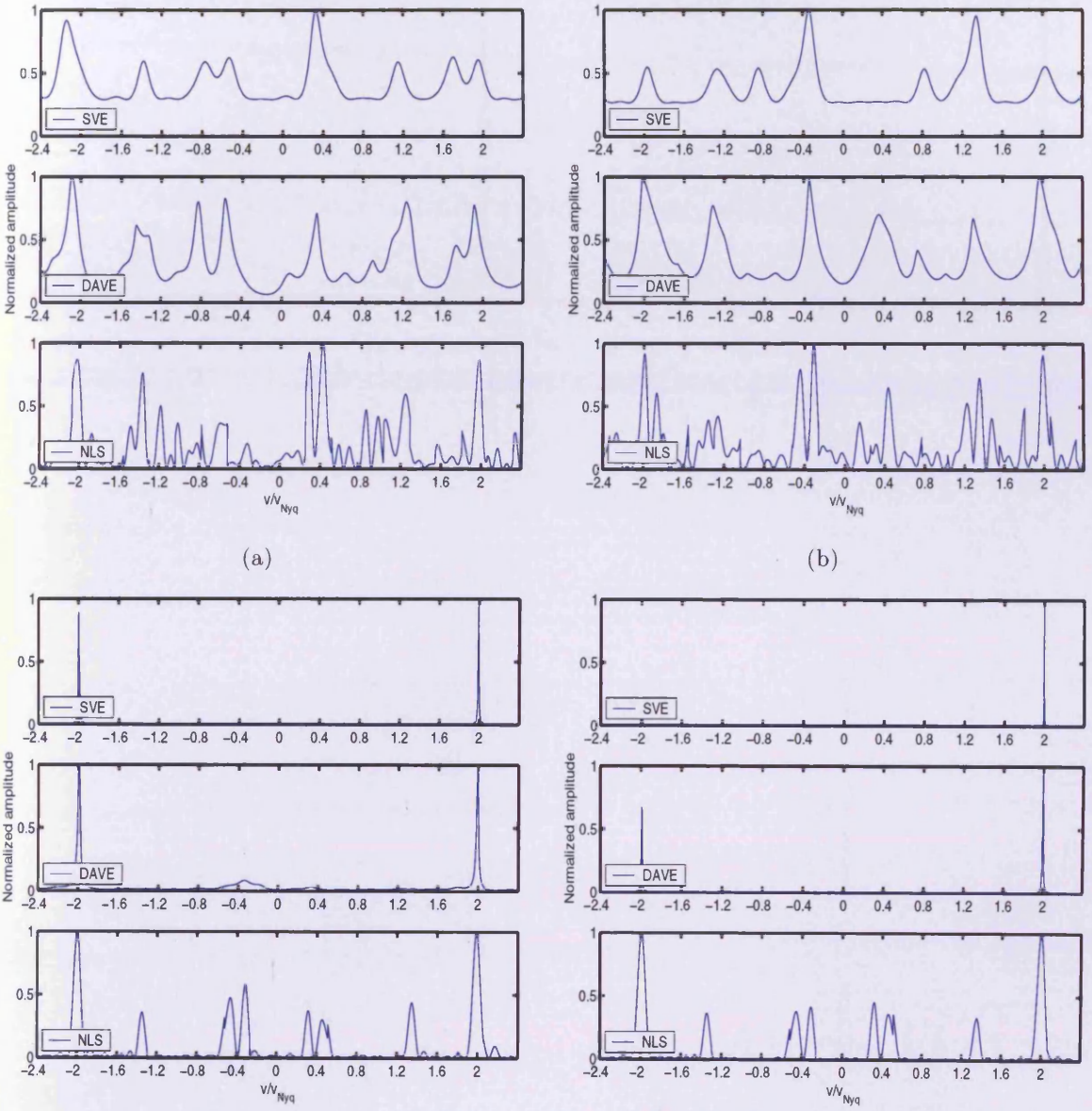

Figure 3.2. The velocity spectra using the proposed methods, with underlying true velocity, $v = 2v_{Nyq}$, obtained from (a) $SNR = -5$ dB; (b) $SNR = 0$ dB; (c) $SNR = 10$ dB; (d) $SNR = 20$ dB.

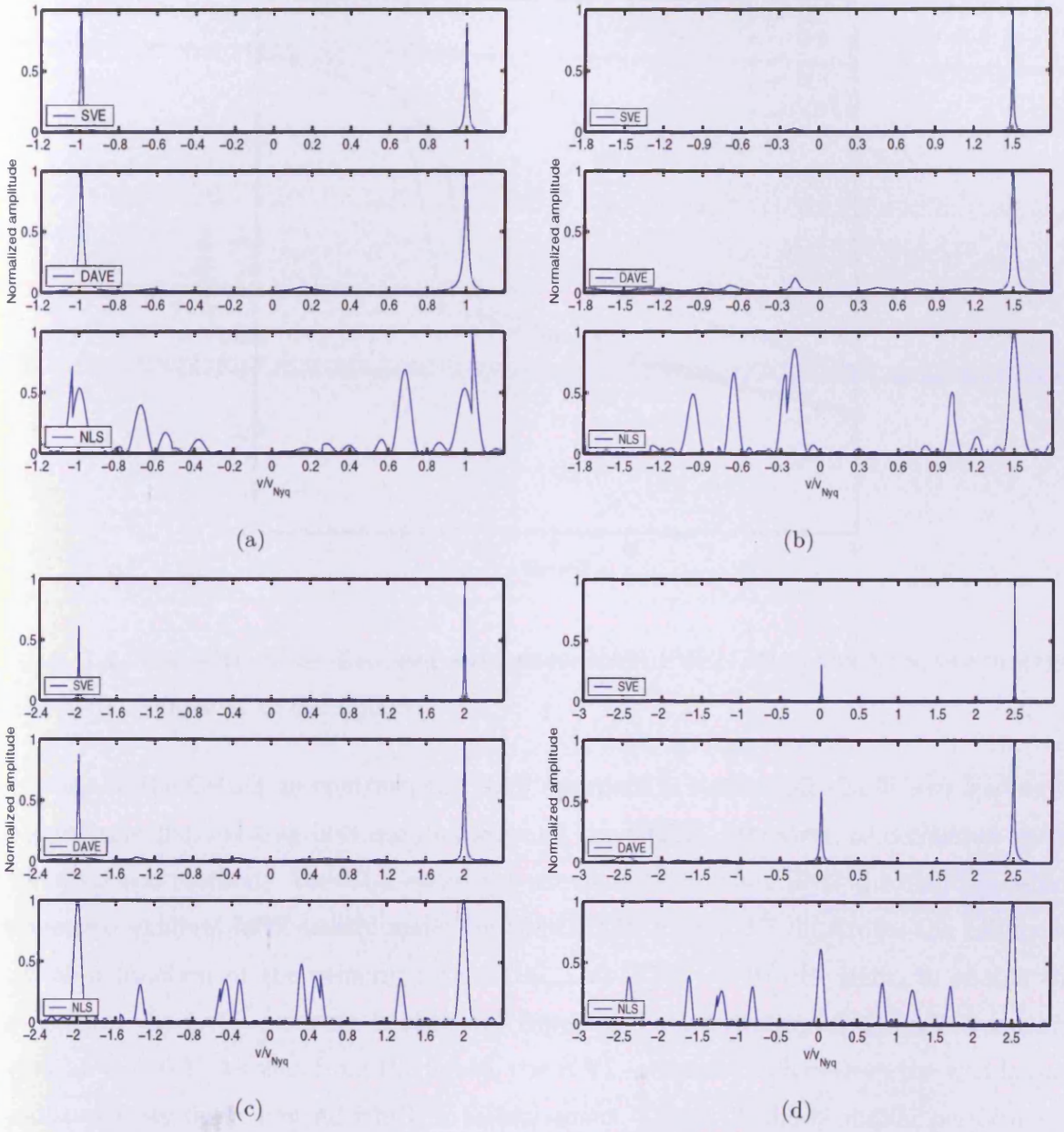

Figure 3.3. The velocity spectra using the proposed methods, with $SNR = 10$ dB, obtained from (a) $v = v_{Nyq}$; (b) $v = 1.5v_{Nyq}$; (c) $v = 2v_{Nyq}$; (d) $v = 2.5v_{Nyq}$.

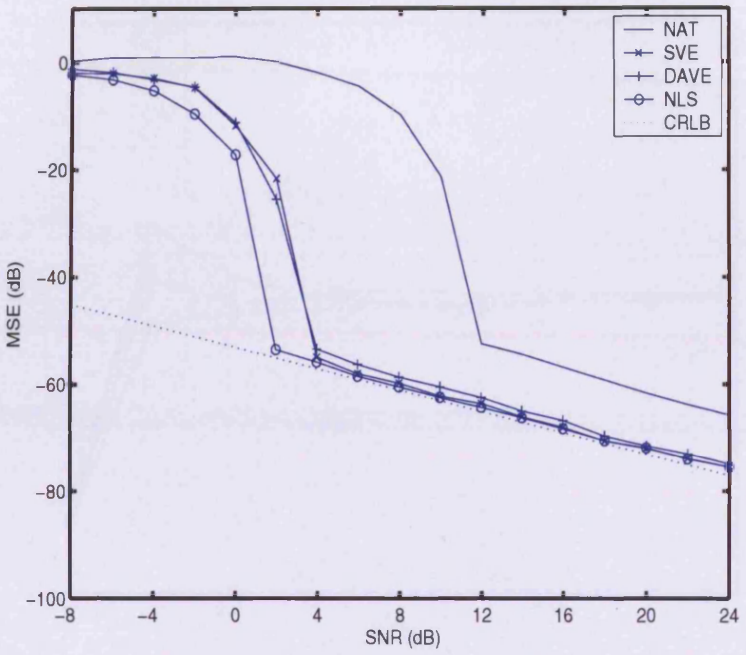

Figure 3.4. The MSE of the discussed estimators, NAT, SVE, DAVE and NLS, as a function of the SNR, compared to the CRLB.

very close to the CRLB. In contrast, the NAT approach is statistically inefficient leading to the significant gap existing between its MSE and the CRLB. Moreover, as compared to the other proposed methods, the NLS estimator shows slightly lower SNR threshold at which the method exhibits MSE nearly matching the CRLB. Figure 3.5 illustrates the estimated MSE as a function of the velocity ratio v/v_{Nyq}, at $SNR = 10$ dB. Here, to enable the comparison, the KAT estimate is obtained from the backscattering of a single frequency carrier at $f_3 = 0.1$. As seen from the figure, the KAT estimator suffers from the well-known Nyquist velocity limit, beyond which it breaks down. The NAT shows similar performance to that using KAT for velocities below v_{Nyq}. As is clear from the figure, the proposed SVE,

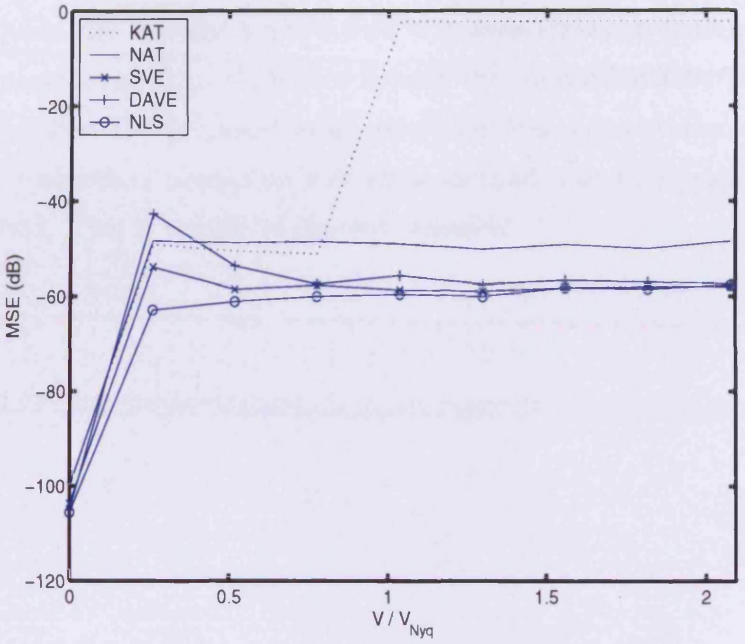

Figure 3.5. The MSE of the discussed estimators, KAT, NAT, SVE, DAVE and NLS, as a function of the velocity.

DAVE and NLS estimators uniformly exhibit lower MSE than the NAT over the whole examined velocity range. Furthermore, the NLS method shows preferable performance as compared to the proposed SVD and DAVE methods. The results shown in Figure 3.4 and Figure 3.5 are obtained from 10^3 Monte Carlo simulations.

3.4 Conclusions

In this chapter, three novel velocity estimators using multiple frequency carriers have been developed. Furthermore, the CRLB for the velocity estimation is derived to evaluate the performance of the proposed methods. Analysis shows that these new estimators are able

to mitigate the poor high velocity performance of conventional correlation based techniques and thereby to provide usable performance beyond the conventional Nyquist velocity limit. It is worth noting that the proposed estimators have high computational complexity. As a result, further research is needed on how these methods can be implemented with lower computational load. This is a topic of ongoing research.

Appendix

3.A Derivation of (3.2.11)

Following [SM05], the derivation of (3.2.16) is given as follows. The initial phase terms $\{\varphi_k\}$ are modeled as independent random variables uniformly distributed on $[-\pi, \pi)$. Recalling (3.2.11), $\mathbf{P}$ can be written as

$$\begin{aligned} \mathbf{P} &= E\{\mathbf{\Phi}_v(t)\boldsymbol{\beta}\boldsymbol{\beta}^H\mathbf{\Phi}_v^H(t)\} \\ &= \mathbf{\Phi}_v(t)E\{\boldsymbol{\beta}\boldsymbol{\beta}^H\}\mathbf{\Phi}_v^H(t). \end{aligned} \tag{3.A.1}$$

Recalling β_k defined in (3.2.3), $E\{\boldsymbol{\beta}\boldsymbol{\beta}^H\}$ can be further simplified as

$$\left[E\{\boldsymbol{\beta}\boldsymbol{\beta}^H\}\right]_{k,l} = \alpha_k\alpha_l E\{e^{i\varphi_k}e^{-i\varphi_l}\} \tag{3.A.2}$$

where $[\mathbf{X}]_{k,l}$ denotes the element of $\mathbf{X}$ at its k^{th} row and l^{th} column. For $k = l$,

$$E\{e^{i\varphi_k}e^{-i\varphi_l}\} = 1, \tag{3.A.3}$$

and for $k \neq l$, this becomes

$$\begin{aligned} E\{e^{i\varphi_k}e^{-i\varphi_l}\} &= E\{e^{i\varphi_k}\}E\{e^{-i\varphi_l}\} \\ &= \left[\frac{1}{2\pi}\int_{-\pi}^{\pi} e^{i\varphi}d\varphi\right]\left[\frac{1}{2\pi}\int_{-\pi}^{\pi} e^{-i\varphi}d\varphi\right] \\ &= 0. \end{aligned} \tag{3.A.4}$$

Thus,

$$E\{\boldsymbol{\beta}\boldsymbol{\beta}^H\} = \text{diag}\left\{\left[\begin{array}{ccc} \alpha_1^2 & \ldots & \alpha_d^2 \end{array}\right]\right\}, \tag{3.A.5}$$

and as a result,

$$\begin{aligned} \mathbf{P} &= \mathbf{\Phi}_v(t)E\{\boldsymbol{\beta}\boldsymbol{\beta}^H\}\mathbf{\Phi}_v^H(t) \\ &= E\{\boldsymbol{\beta}\boldsymbol{\beta}^H\}, \end{aligned} \tag{3.A.6}$$

where $\mathbf{\Phi}_v(t)$ is a diagonal matrix defined in (3.2.9).

3.B Proof of (3.2.16)

Following [SM05], the proof of (3.2.16) is given as follows. Recalling the covariance matrix $\mathbf{R}_y$ in (3.2.10), let $\lambda_1 \geq \lambda_2 \geq \cdots \geq \lambda_L$ denote the eigenvalues of $\mathbf{R}_y$, and let

$$\mathbf{S} = [\mathbf{s}_1, \cdots, \mathbf{s}_d]_{L\times d} \tag{3.B.1}$$

in which the orthonormal eigenvectors $\{\mathbf{s}_k\}$ associated with $\{\lambda_1, \cdots, \lambda_d\}$ span the signal subspace $\mathcal{R}(\mathbf{S})$, and the noise subspace $\mathcal{N}(\mathbf{G})$ is spanned by the columns of

$$\mathbf{G} = [\mathbf{g}_1, \cdots, \mathbf{g}_{L-d}]_{L\times(L-d)} \tag{3.B.2}$$

in which the orthonormal eigenvectors $\{\mathbf{g}_k\}$ are corresponding to $\{\lambda_{d+1}, \cdots, \lambda_L\}$, and it can be shown that [SM05]

$$\lambda_{d+1} = \cdots = \lambda_L = \sigma^2 \tag{3.B.3}$$

when white noise $w(t)$ is assumed in (3.2.1). From (3.2.10) and (3.B.3), it follows that

$$\mathbf{R}_y\mathbf{G} = \mathbf{G}\begin{bmatrix} \lambda_{d+1} & & \mathbf{0} \\ & \ddots & \\ \mathbf{0} & & \lambda_L \end{bmatrix} = \sigma^2\mathbf{G} = \mathbf{A}_L(v)\mathbf{P}\mathbf{A}_L^H(v)\mathbf{G} + \sigma^2\mathbf{G}. \tag{3.B.4}$$

As a result,

$$\mathbf{A}_L(v)\mathbf{P}\mathbf{A}_L^H(v)\mathbf{G} = \mathbf{0} \tag{3.B.5}$$

which further implies that

$$\mathbf{A}_L^H(v)\mathbf{G} = \mathbf{0} \tag{3.B.6}$$

as $\mathbf{A}_L(v)\mathbf{P}$ has full column rank. Therefore, the true frequencies and thus the corresponding underlying true velocity can be estimated by minimizing the following equation [SM05]

$$v = \arg\min_v \|\mathbf{A}_L^H(v)\mathbf{G}\|_F^2. \tag{3.B.7}$$

3.C Proof of (3.2.21)

Following [SM05], the proof of (3.2.21) is given as follow. As $\mathbf{R}_y$ is a Hermitian positive matrix and matrix $\mathbf{A}_L(v)$ has full column rank equal to d, it can be proven that the unique solution to the minimization problem

$$\mathbf{h}_k(v) = \arg\min_{\mathbf{h}_k(v)} \mathbf{h}_k^H(v)\mathbf{R}_y\mathbf{h}_k(v) \quad \text{subj. to} \quad \mathbf{h}_k(v)\mathbf{A}_L(v) = \mathbf{u}_k^T \tag{3.C.1}$$

is given by

$$\hat{\mathbf{h}}_k(v) = \mathbf{R}_y^{-1}\mathbf{A}_L(v)\left(\mathbf{A}_L^H(v)\mathbf{R}_y^{-1}\mathbf{A}_L(v)\right)^{-1}\mathbf{u}_k \tag{3.C.2}$$

which satisfies

$$\hat{\mathbf{h}}_k(v)\mathbf{A}_L(v) = \mathbf{u}_k^T. \tag{3.C.3}$$

Proof: Let $\mathbf{h}_k(v) = \hat{\mathbf{h}}_k(v) + \triangle$ where $\triangle \in \mathbb{C}^{L\times 1}$ with $\triangle^H\mathbf{A}_L(v) = \mathbf{0}$ so that $\mathbf{h}_k(v)$ also satisfies $\mathbf{h}_k^H(v)\mathbf{A}_L(v) = \mathbf{0}$. Then

$$\mathbf{h}_k^H(v)\mathbf{R}_y\mathbf{h}_k(v) = \hat{\mathbf{h}}_k^H(v)\mathbf{R}_y\hat{\mathbf{h}}_k(v) + \hat{\mathbf{h}}_k^H(v)\mathbf{R}_y\triangle + \triangle^H\mathbf{R}_y\hat{\mathbf{h}}_k(v) + \triangle^H\mathbf{R}_y\triangle \tag{3.C.4}$$

where the two middle terms are equal to each other

$$\{\hat{\mathbf{h}}_k^H(v)\mathbf{R}_y\triangle\}^H = \triangle^H\mathbf{R}_y\hat{\mathbf{h}}_k(v) \tag{3.C.5}$$

as $\mathbf{R}_y^H = \mathbf{R}_y$. Recalling (3.C.2), it can be shown that

$$\begin{aligned}\triangle^H\mathbf{R}_y\hat{\mathbf{h}}_k(v) &= \triangle^H\mathbf{R}_y\mathbf{R}_y^{-1}\mathbf{A}_L(v)\left(\mathbf{A}_L^H(v)\mathbf{R}_y^{-1}\mathbf{A}_L(v)\right)^{-1}\mathbf{u}_k \\ &= \triangle^H\mathbf{A}_L(v)\left(\mathbf{A}_L^H(v)\mathbf{R}_y^{-1}\mathbf{A}_L(v)\right)^{-1}\mathbf{u}_k \\ &= \mathbf{0}\end{aligned} \tag{3.C.6}$$

where $\triangle^H\mathbf{A}_L(v) = \mathbf{0}$. As a result, (3.C.4) can be rewritten as

$$\mathbf{h}_k^H(v)\mathbf{R}_y\mathbf{h}_k(v) - \hat{\mathbf{h}}_k^H(v)\mathbf{R}_y\hat{\mathbf{h}}_k(v) = \triangle^H\mathbf{R}_y\triangle \geq 0 \tag{3.C.7}$$

where $\mathbf{R}_y$ is positive definite. Therefore, it follows from (3.C.7) that the minimizing $\mathbf{h}_k(v)$ is identical to $\mathbf{h}_k^H(v)$ given in (3.C.2).

3.D Low Rank Approximation

To alleviate the rank deficiency problem in (3.2.22) in Section 3.2.3, a low rank approximation technique is employed, noting that a least-squares solution can be found using the singular value decomposition. Let

$$\mathbf{Q} = \mathbf{U}\boldsymbol{\Sigma}\mathbf{V}^H \tag{3.D.1}$$

where $\boldsymbol{\Sigma}$ is a diagonal matrix containing the d singular values of $\mathbf{Q}$ on the diagonal, and where $\mathbf{U}$ and $\mathbf{V}$ are unitary matrices. Further, let σ_l denote the lth singular value of $\mathbf{Q}$, and note that the solution minimizing $\|\mathbf{Q}\mathbf{r}_k - \mathbf{u}_k\|_2$, where $\|\cdot\|_2$ denotes the 2-norm and $\mathbf{u}_k$ is defined in (3.2.19), can be found as [GV96]

$$\hat{\mathbf{r}}_k = \sum_{l=1}^{\tilde{d}} \sigma_l^{-1}\mathbf{U}_l^H\mathbf{u}_k\mathbf{V}_l \tag{3.D.2}$$

where $\mathbf{U}_l$ and $\mathbf{V}_l$ denote the lth column of $\mathbf{U}$ and $\mathbf{V}$, respectively, and where $\tilde{d}$ is the rank of $\mathbf{Q}$, or alternatively the selected low-rank approximation of $\mathbf{Q}$. Using (3.D.2), then (3.2.22) can be expressed as

$$\hat{\rho}_{\hat{y}}^2(v) = \sum_{k=1}^{d} \mathbf{u}_k^T\hat{\mathbf{r}}_k \tag{3.D.3}$$

3.E Cramér-Row Lower Bound

Recalling (3.2.24) and (3.2.25), the unknown parameter vector $\boldsymbol{\theta} \in \mathbb{R}^{2d+1}$ is defined as

$$\boldsymbol{\theta} = [\Re(\boldsymbol{\beta}), \Im(\boldsymbol{\beta}), v]^T, \tag{3.E.1}$$

where $\Re[\boldsymbol{\beta}]$ and $\Im[\boldsymbol{\beta}]$ are the real and the imaginary parts of the complex amplitude $\boldsymbol{\beta} = [\beta_1, \ldots, \beta_d]^T$, respectively.

It holds that $\mathbf{y_N}$ has the complex Gaussian PDF

$$p(\mathbf{y_N}; \boldsymbol{\theta}) = \frac{1}{\pi^N \det \mathbf{C}_{\mathbf{y_N}}} e^{-(\mathbf{y_N} - \boldsymbol{\mu}(\boldsymbol{\theta}))^H \mathbf{C}_{\mathbf{y_N}}^{-1} (\mathbf{y_N} - \boldsymbol{\mu}(\boldsymbol{\theta}))}, \tag{3.E.2}$$

where $\mathbf{C}_{\mathbf{y_N}} = \sigma^2 \mathbf{I}$ and $\det(\cdot)$ the determinant operation, with

$$\boldsymbol{\mu}(\boldsymbol{\theta}) = [x(0), \cdots, x(N-1)]^T. \tag{3.E.3}$$

As a result, according to [Kay93], the Fisher information matrix (FIM) of $\boldsymbol{\theta}$ can be written as

$$\mathbf{FIM}(\boldsymbol{\theta}) = 2\sigma^{-2} \Re \left[\frac{\partial \boldsymbol{\mu}^H(\boldsymbol{\theta})}{\partial \boldsymbol{\theta}} \frac{\partial \boldsymbol{\mu}(\boldsymbol{\theta})}{\partial \boldsymbol{\theta}^T} \right]_{(2d+1)\times(2d+1)}. \tag{3.E.4}$$

Note that

$$\frac{\partial \boldsymbol{\mu}^H(\boldsymbol{\theta})}{\partial \boldsymbol{\theta}} = \begin{pmatrix} \frac{\partial \boldsymbol{\mu}^H(\boldsymbol{\theta})}{\partial \Re(\boldsymbol{\beta})} \\ \frac{\partial \boldsymbol{\mu}^H(\boldsymbol{\theta})}{\partial \Im(\boldsymbol{\beta})} \\ \frac{\partial \boldsymbol{\mu}^H(\boldsymbol{\theta})}{\partial v} \end{pmatrix}_{(2d+1)\times N} \tag{3.E.5}$$

and it can be shown that

$$\frac{\partial \boldsymbol{\mu}^H(\boldsymbol{\theta})}{\partial \Re(\boldsymbol{\beta})} = \mathbf{A}_N^H(v),$$

$$\frac{\partial \boldsymbol{\mu}^H(\boldsymbol{\theta})}{\partial \Im(\boldsymbol{\beta})} = -i\mathbf{A}_N^H(v),$$

$$\frac{\partial \boldsymbol{\mu}^H(\boldsymbol{\theta})}{\partial v} = \boldsymbol{\Delta}$$

where $\boldsymbol{\Delta} = -i\frac{4\pi}{c}\left[(\mathbf{f} \odot \boldsymbol{\beta}^H)\mathbf{A}_N^H(v)\right] \odot \mathbf{t}$, with $\odot$ denoting the Schur-Hadamard (element-wise) product, $\mathbf{f}^T = [f_{c_1}, \ldots, f_{c_d}]^T$ and $\mathbf{t}^T = [0, \ldots, N-1]^T$. Similarly,

$$\frac{\partial \boldsymbol{\mu}(\boldsymbol{\theta})}{\partial \boldsymbol{\theta}^T} = \left(\frac{\partial \boldsymbol{\mu}(\boldsymbol{\theta})}{\partial \Re(\boldsymbol{\beta})^T} \quad \frac{\partial \boldsymbol{\mu}(\boldsymbol{\theta})}{\partial \Im(\boldsymbol{\beta})^T} \quad \frac{\partial \boldsymbol{\mu}(\boldsymbol{\theta})}{\partial v} \right)_{N \times (2d+1)} \tag{3.E.6}$$

with

$$\frac{\partial \boldsymbol{\mu}(\boldsymbol{\theta})}{\partial \Re(\boldsymbol{\beta})^T} = \mathbf{A}_N(v),$$

$$\frac{\partial \boldsymbol{\mu}(\boldsymbol{\theta})}{\partial \Im(\boldsymbol{\beta})^T} = i\mathbf{A}_N(v),$$

$$\frac{\partial \boldsymbol{\mu}(\boldsymbol{\theta})}{\partial v} = \boldsymbol{\Delta}^H.$$

Thus, the FIM can be rewritten as

$$\mathbf{FIM}(\boldsymbol{\theta}) = 2\sigma^{-2}\Re \begin{bmatrix} \boldsymbol{\Psi}(v) & i\boldsymbol{\Psi}(v) & \mathbf{A}_N^H(v)\boldsymbol{\Delta}^H \\ -i\boldsymbol{\Psi}(v) & \boldsymbol{\Psi}(v) & -i\mathbf{A}_N^H(v)\boldsymbol{\Delta}^H \\ \boldsymbol{\Delta}\mathbf{A}_N(v) & i\boldsymbol{\Delta}\mathbf{A}_N(v) & \|\boldsymbol{\Delta}\|^2 \end{bmatrix} \tag{3.E.7}$$

where $\boldsymbol{\Psi}(v) = \mathbf{A}_N^H(v)\mathbf{A}_N(v)$ as in (3.2.28).

Thus, the CRLB for the velocity v can be obtained as

$$var(v) \geq \left[\mathbf{FIM}^{-1}(\boldsymbol{\theta})\right]_{(2d+1),(2d+1)}. \tag{3.E.8}$$

Part II

Application: Ultrasound

Chapter 4

FUNDAMENTALS OF MEDICAL ULTRASOUND

Ultrasound has found wide application in medicine and currently more than one fourth of medical imaging is produced via ultrasonic systems [Wel94]. An example of a modern portable ultrasound scanner is shown in Figure 4.1. Before examining the proposed methods with realistic ultrasound RF data, it is preferable to introduce some general theory of ultrasound. In this chapter, some basic physics encountered in the use of ultrasonic techniques will be discussed. First of all, wave propagation and wave interaction with human tissue will be reviewed, followed by the issues of transducer, beamforming and resolution. Then, the discussion will be focused on pulsed wave (PW) systems. More in-depth study of the physics of ultrasound can be found in [Jen96a, EM00, Hil86, LSE+86, Mai78], and the references therein.

4.1 Wave Propagation and Interaction

Waves can be classified into mechanical waves and non-mechanical waves, depending on whether they need a medium for propagation or not. A mechanical wave needs a medium to propagate while a non-mechanical wave does not, for example, ultrasound waves are

Figure 4.1. SonoSite portable ultrasound scanner (model: *SonoSite 180plus*). The total weight of this device is 2.6 kg. (Courtesy of SonoSite: www.sonosite.com).

mechanical since they need a medium (tissue) to propagate. Light is a non-mechanical wave since it can propagate in vacuum. From the point of view of the wave propagation direction, waves can also be defined as a longitudinal wave or transverse wave. If the vibration is parallel to the direction of propagation then the wave is a longitudinal wave, on the other hand if the vibration is perpendicular to the direction of propagation, then the wave is called a transverse wave. Further, from the point of view of identifying a wave pressure at a specific spatial point, waves can be regarded as scalar and vector waves, respectively. For a scalar wave, only the distance from the source origin (say transducer) is needed to identify the wave at each point in the medium, this is the case for a longitudinal wave. However, for a vector wave, not only a value of distance but also one of direction is needed; this is the case for a transverse wave. Ultrasonic waves are mechanical scalar waves [Hil86]. Other types of waves such as transverse waves are rarely applied in medical ultrasonics due to the strong

attenuation in soft tissue [EM00]. The general sound wave equation in three-dimensions can be expressed as [Mai78]

$$\frac{\partial^2\psi(x,y,z,t)}{\partial t^2} = c^2\left(\frac{\partial^2\psi(x,y,z,t)}{\partial x^2} + \frac{\partial^2\psi(x,y,z,t)}{\partial y^2} + \frac{\partial^2\psi(x,y,z,t)}{\partial z^2}\right) \tag{4.1.1}$$

where $\psi(x,y,z,t)$ is the wave amplitude (acoustic pressure) at point (x,y,z) at time t. The parameter c is the propagation speed in the medium, which depends on the medium, and is given by

$$c = \frac{1}{\sqrt{\rho K}} \tag{4.1.2}$$

where ρ is the mean density (kg/m^3) and K the compressibility (m^2/N), assuming no net transfer of energy from the wave to the medium. The speed values for soft tissue within the human body are closely clustered around 1540 m/s, which for this reason is normally chosen as the standard *sound speed* in medical ultrasound [EM00]. It is virtually independent of frequency of the transmitted sound and depends on the density and compressibility of the medium as shown in (4.1.2). Furthermore, the sound speed, c, is equal to the carrier frequency f_c of the transmitted sound times the wavelength λ stated mathematically as

$$c = f_c\lambda \tag{4.1.3}$$

By definition, a sound having a carrier frequency above 20 kHz is called *ultrasound.* For medical purposes, carrier frequencies between $2-10$ MHz are used [EM00], which corresponds to the wavelength range of $0.77-0.154$ mm (provided that the ultrasound velocity c is 1540 m/s). As ultrasound waves propagate into tissue, due to the changes of the acoustic properties of the media, they will encounter certain phenomena - *scattering, reflection, refraction* and *attenuation.*

Scattering

Scattering occurs when a sound wave travelling through a medium encounters a discontinuity of dimensions similar to or less than the wavelength of the wave. Some of the energy

of the wave is scattered in all directions. This phenomenon will definitely exist in medical ultrasound when investigating the blood flow in the human body and it enables the use of ultrasound for estimating blood velocities. This is because the estimation of blood velocity will rely on the scattering of the wave as it interacts with the blood. In the human body there exist many structures (cells, fibers, and connective tissues). which are much smaller than the wavelength of the emitted ultrasound. The emitted wave will interact with these numerous small structures, termed scatterers, during the propagation. Scattering from objects which are less than 10 times smaller than the wavelength is usually referred to as Rayleigh scattering [Jen96a]. The scattered strength is proportional to the fourth power of frequency [EM00]. The strength of a backscattered signal can be described either by the backscattering coefficient or the backscattering cross-section [Jen96a]. The measurement of backscattering cross-section is difficult to obtain in practice [EM00]. For different structures, the backscattering coefficients are different and so too is the backscattering strength. Analysis shows the clutter is 20 - 60 dB stronger than the backscattered signals from the blood scatterers [HvdVD+91, Jen93b, EM00]. Given the vast number of scattering ensembles, it is often appropriate to characterize the scattered waves in statistical terms. As the contributions from scatterers can be assumed independent, the *central limit theorem* states that the amplitude distribution of the scattered waves follows a zero mean Gaussian distribution [WSSL83, Jen96a]. Also, the amplitudes follow a complex Gaussian distribution with zero mean when the amplitudes are complex. It is worth noting that the backscattered signal is deterministic; the same signal will result as if a stationary structure is probed. However, for a slight movement in position, the successively received echoes are not equal, although still correlated. This correlation makes it possible to estimate blood velocities with ultrasound. As there is a strong correlation for small movements, it is possible to detect shifts in position by correlating the successive measurements of the moving blood ensembles.

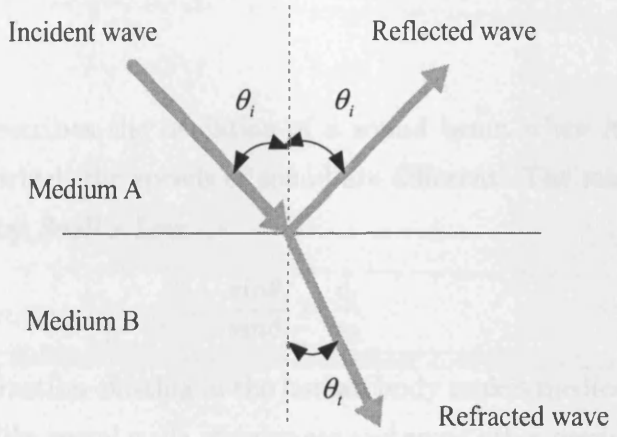

Figure 4.2. Reflection and refraction of a sound wave.

Reflection

Reflection is a special case of scattering which occurs at smooth surfaces on which the irregularities are very much smaller than a wavelength. As a wavefront encounters a smooth surface with an incident angle θ_i, it will be reflected at an equal angle as shown in Figure 4.2. The amplitude of the reflected wave can be calculated by [EM00]

$$a_r = a_i \left(\frac{\rho_2 c_2 cos\theta_i - \rho_1 c_1 cos\theta_t}{\rho_2 c_2 cos\theta_i + \rho_1 c_1 cos\theta_t} \right) \tag{4.1.4}$$

where a_r and a_i are the reflected amplitude and the incident amplitude, respectively; θ_i and θ_t denote the wave incident angle and the angle of refraction, respectively, as shown in Figure 4.2; further, ρ_1 and ρ_2 denote the density of medium A and medium B, respectively; and c_1 and c_2 are the corresponding speeds in these media. The amplitude of the reflected waves will be much stronger than that from scattering since the energy in the latter case is scattered in all directions. In diagnostic ultrasound, a combination of reflections and backscattered

echoes is picked up by the receiver.

Refraction

The term *refraction* describes the deviation of a sound beam when it crosses a boundary between two media in which the speeds of sound are different. The resultant angle of propagation is determined by *Snell's Law*:

$$\frac{sin\theta_i}{sin\theta_t} = \frac{c_1}{c_2} \tag{4.1.5}$$

The phenomenon of refraction existing in the human body makes medical ultrasound capable to map the boundaries like vessel walls, diaphragm and some other organ boundaries [Jen96a, EM00,Sch01]. Together with scattering and reflection, these effects make *colour flow imaging* possible.

Attenuation

Ultrasound propagation in tissue will be attenuated due to scattering and absorption, which is referred to as *attenuation*. Scattering will spread part of the energy in all directions while absorption will convert the acoustic energy into thermal energy due to viscous loss, heat conduction and the molecular exchanges of energy. The majority of the lost acoustic energy comes from absorption which can be up to 95% [Jen96a]. The attenuation is strongly dependent on frequency. Higher frequency will result in larger attenuation, which means that the backscattered echoes from deep-lying interfaces will be too weak to be detected and limits the effective probed depth. Thus there is a trade-off between the penetration depth, resolution and level of transmitted power. Attenuation limits the typical ultrasound system to depths of $10-30$ cm when frequencies between $2-10$ MHz are employed. Higher frequencies, such as 50 MHz, are limited to a 1-cm depth, but they offer the advantage of improved resolution, which could be useful for applications related to the eye, skin, and

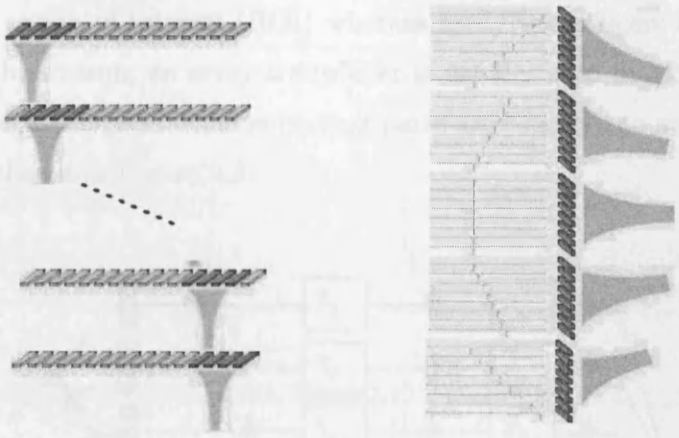

(a) (b)

Figure 4.3. (a) A linear array transducer used to scan a medium. (b) The steering process in a phased linear array transducer.

intravascular imaging [LTCF96].

4.2 Transducer, Beamforming and Resolution

Transducer

An ultrasonic transmitter-receiver, termed *transducer*, is the part of an ultrasound system that generates an ultrasonic beam and detects backscattered echoes. These are made from materials that contain piezoelectric (PZT) crystals. A PZT crystal will vibrate when excited by an alternating current (AC) electric signal of the right frequency (transmit mode). Conversely, it can generate a small electric signal when forced to vibrate (receive mode). A transducer is used to convert electronic signals to ultrasound waves and vice versa [Jen96a, EM00].

Typically, there are two kinds of transducers used in an ultrasound system, *single element transducers* and *array transducers*. For a single element transducer, it must be steered me-

chanically over the region of interest (ROI) whereas array transducers can steer the beam electronically. For this reason, an array transducer is usually used in blood flow imaging in modern ultrasound systems, and thus no moving parts are required to sweep the ultrasound beam direction, as shown in Figure 4.3.

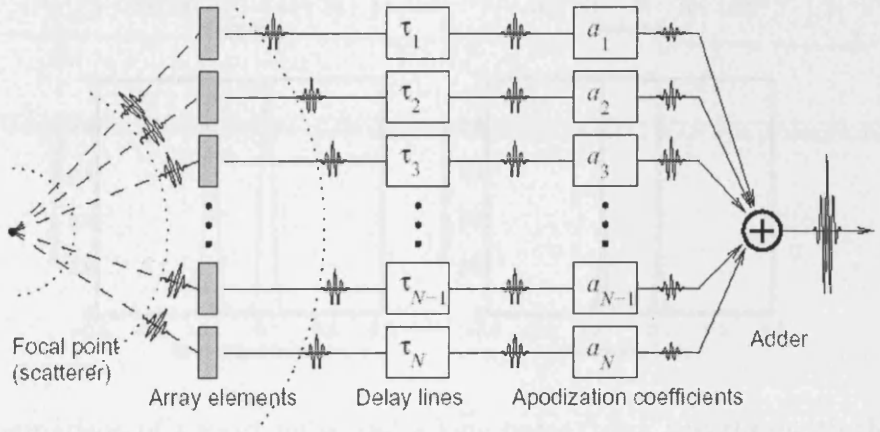

Figure 4.4. Beamforming for reception in a phased array transducer, reproduced from [Nik01].

Beamforming

For a phased array transducer, the transmitted and received signals can also be individually delayed in time, hence the term *phased array*. Through time delays a beam can be steered in a given direction and focused at a given axial distance both in transmit and receive, this is called *beamforming*. A detailed description of beamforming for reception in a phased array transducer is shown in Figure 4.4. Using simple geometric relations a transducer can be focused at any point [Nik01].

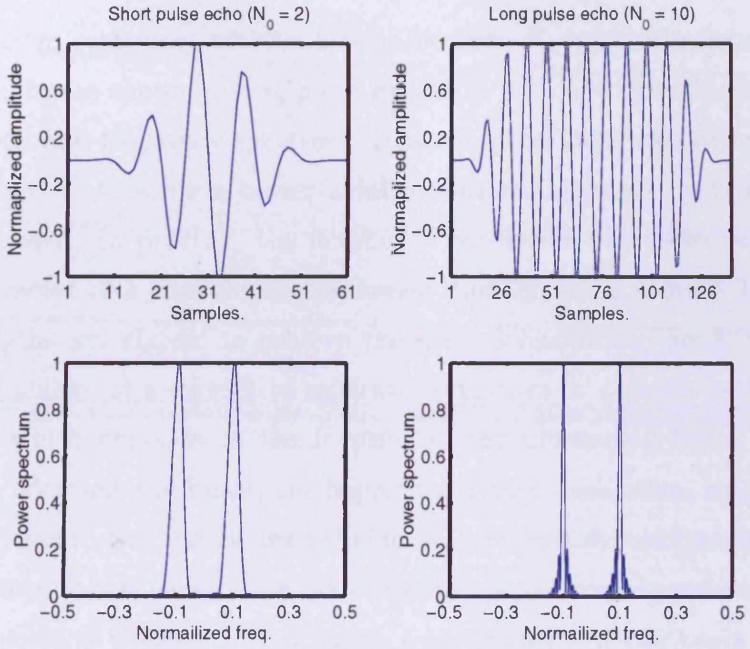

Figure 4.5. Comparison of a short pulse and a long pulse (top), together with their spectra (bottom), the true normalized carrier frequency is 0.1.

Resolution

The ability to distinguish echoes from adjacent reflectors in tissue is termed *resolution*, which is determined both by how close the reflectors are positioned to each other and the ability of the system's beamforming. Resolution comprises two features, *axial resolution* and *lateral resolution*. *Axial resolution* is the ability of a system to separate structures lying closely along wave propagation direction. It is determined by the length of the ultrasound pulse generated by the transducer. A long pulse will interact with a range of scatterers which move with different velocities, the recorded RF data will therefore contain a range of velocities due to the velocity spread. As a result, the averaged estimate of velocity will have a higher variance for an increasing velocity spread. Figure 4.5 shows the difference for a short pulse

echo (reflection from scatterer) with oscillation number $N_o = 2$ and a long pulse echo with $N_o = 10$. As the figure shows, a long pulse results in a narrowband spectrum and a short pulse gives a wideband frequency spectrum. Hence, a good axial resolution can be achieved by firing short bursts; to achieve better axial resolution, only one cycle instead of several cycles should be used. In practice, the number of oscillation of a pulse is restricted by the bandlimited character of a transducer, the lowest number being around 2. Typically, from 6 to 32 wavelengths are chosen to achieve the desired resolution [Jen96a, EM00]. *Lateral resolution* is the ability of a system to separate structures in a plane perpendicular to the beam direction, which depends on the focusing of the ultrasound beam produced by the transducer. The narrower the beam, the higher the lateral resolution, since a narrow beam enables small objects to become distinguishable. All systems should be designed to produce narrow beams, since this is usually the major limitation on lateral resolution. Also, a beam with uniform intensity is preferred. In practice, a nonuniform intense beam exists in the near field and a uniform beam is present in the far field (area of diverging beam in which lateral resolution is poor). It is possible to smooth the near field intensity pattern so as to yield a narrow beam with almost uniform intensity. Thus, a broadband pulse will produce many frequencies rather than just a single frequency. The presence of multiple frequencies tends to make the near field more uniform. Each frequency has an independent interference pattern, and when these patterns are superimposed on one another, the result is a smoothing of the overall intensity pattern. This reasoning also motivates the use of multi-frequency carriers in the transmission.

4.3 Pulsed Wave System

With respect to blood flow velocity estimation, two kinds of modes can be distinguished, *continuous wave* (CW) mode and *pulsed wave* (PW) mode as shown in Figure 4.6. In CW

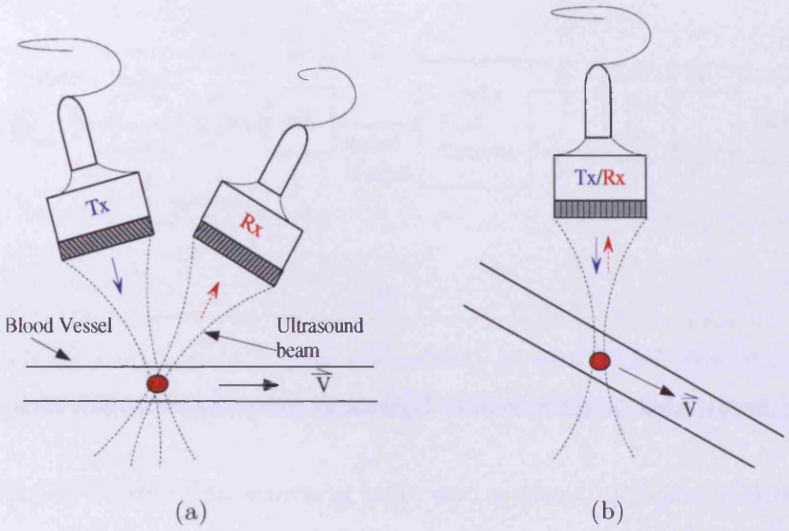

Figure 4.6. (a) *Continuous wave* (CW) system, *Tx* is the transmitter and *Rx* is the receiver, they use separated transducers; (b) *Pulsed wave* (PW) system, *Tx* and *Rx* use the same transducer.

mode, ultrasound is transmitted and received continuously by means of two transducers. The continuous signal is obtained from the sample volume where the transmitted beam overlaps the sensitivity region of the receiving transducer. With a continuous wave system, reflections will be obtained from all the blood motion along the beam, i.e., it is not possible to know the range from which the measurement was obtained if the two transducers are close to each other [Jen96a]. Instead, in the PW mode, short bursts of ultrasound are emitted with a given pulse repetition frequency. Between transmissions, the transducer is switched to reception mode to catch signals backscattered from blood as well as the surrounding tissue. The position of insonified regions can be localized since as the depth of the region of interest increases, the time before receiving the echo lengthens. Another advantage of a PW system over a CW system is that it only needs one transducer for both transmission and receiving, as shown in Figure 4.6 (b). Therefore, the transducer will

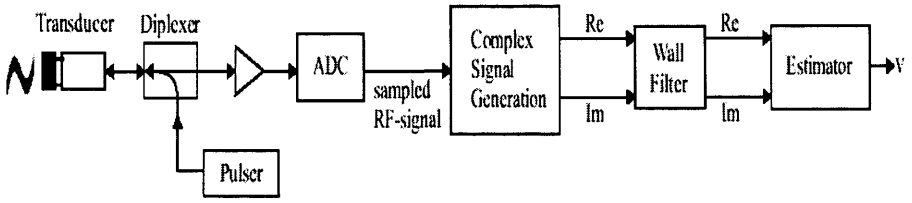

Figure 4.7. Block diagram of a PW ultrasound measurement system, reproduced from [Jen96a]. The *wall filter* in the figure is termed *clutter filter* in this thesis.

need to be switched between an emitting state and a receiving state, which makes diagnosis more convenient. For these reasons, PW mode is widely employed in CFI and herein the discussion will be confined to the PW system. Figure 4.7 briefly illustrates the block diagram of a typical PW ultrasound measurement system for CFI. The transducer emits a pulse and then switches to reception mode and acquires echoes from scatters before firing the next RF line (transmission). After amplifying and digitalizing the echo, the signal is represented in a complex form by a *quadrature demodulation* [Jen96a], normally performed via *Hilbert transform* as later illustrated in (4.3.3). Figure 4.8 depicts the scan-mode acquisition for CFI (left) and an RF data matrix is given (right) with dimension $M \times rN$, where M is the number of depth samples along the fast time (depth-wise) direction and r the number of *line of sight* (LOS). In each LOS, N ultrasound pulses are emitted, and *slow-time* samples can be defined as the N samples of signals resulting from a fixed depth with pulse repetition frequency f_{prf}. Each LOS corresponds to one specific Doppler angle and it is assumed that the flow characteristic changes very small for very limited time duration within each LOS. After firing N pulses in one direction, the pulse beam will sweep to the next LOS and another set of N pulses will be fired with a new Doppler angle. Typically, r is between $50-100$, N around $4-20$, and the imaging across the field of view may be around 15 cm [Jen96a, EM00].

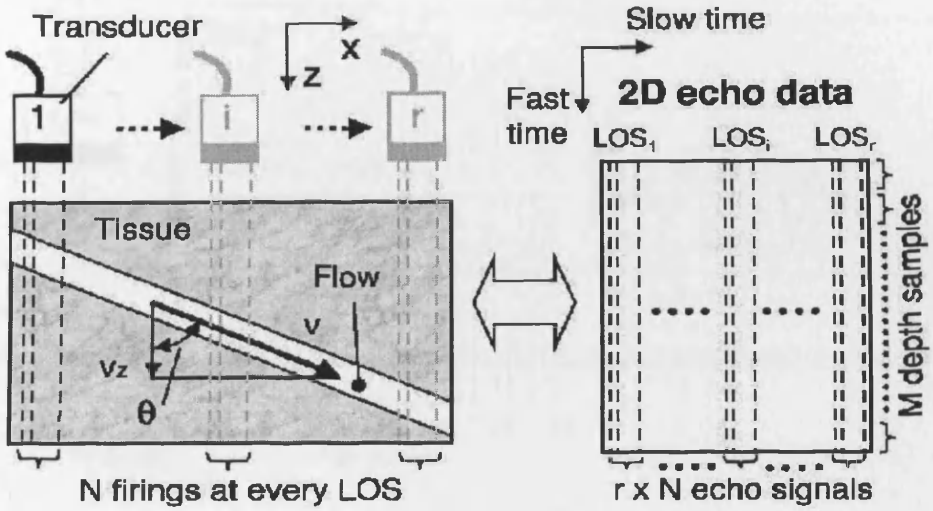

Figure 4.8. Diagram of a CFI measurement system (left) with output of a 2-D RF data matrix (right), reproduced from [KHTI03].

A sensitive technique for velocity estimation must be used since only a few echoes can enter the estimator in order to have a high frame rate. Using more echoes (slow time data samples) for the estimate leads to better estimate accuracy but at the cost of higher computational load which in return results in slower frame rate in CFI. As a result, a compromise between frame rate (estimation time) and accuracy must be found, making both clutter rejection and blood velocity estimation more challenging.

Figure 4.9 illustrates the basic principle of velocity estimation in each LOS, in which a simplified situation is assumed that a single scatterer moves away from the transducer with a velocity of $\vec{v}$. Initially, the depth of a scatterer is d_0 and the echo is recorded by the transducer at time instance $t_0 = 2d_0/c$ from the pulse transmission. Between every two

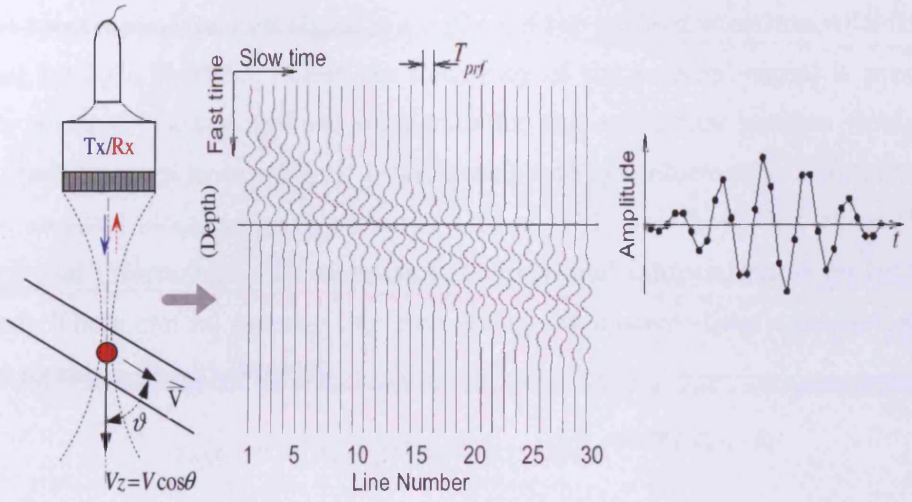

Figure 4.9. Basic principle of the velocity estimation in PW ultrasonic system.

emissions the scatterer moves a distance Δd along the ultrasound beam, which is proportional to the projected velocity along beam/axial direction, v. The time-shift t_s in the arrival time of the signal from pulse-to-pulse is given by

$$t_s = \frac{2\Delta d}{c} = \frac{2v}{c} T_{prf} \tag{4.3.1}$$

where $T_{prf} = 1/f_{prf}$ is the pulse repetition period. These shifted signals are illustrated in Figure 4.9. In order to estimate the velocity at a given depth, a new signal is generated as marked by the horizontal line. The new signal, which is shown on the right-hand side of Figure 4.9, has a sampling frequency of f_{prf}. The signal from a single scatterer and a narrow-band emitted pulse is approximated as [Jen96a]

$$x(n) \approx a(n) \cos(2\pi \frac{2v}{c} f_c n T_{prf} - \varphi) \tag{4.3.2}$$

where $a(n)$ is the envelope amplitude, f_c the carrier frequency, n the n^{th} RF line and φ a phase accounting for the propagation time from the transducer to the depth of interest and

back. The spectrum of the new signal is a replica of the emitted spectrum with the frequency axis scaled by $2v/c$ [Jen96a]. Thus the frequency of the received signal is proportional to the blood velocity. Taking real valued signals for the estimation process yields symmetric Doppler power spectra from which it is not possible to get information about flow direction. Normally, an ideal blood velocity profile or CFI should cover both flow strength as well as flow directional information. To estimate the directional information, complex valued data are needed. These can be obtained by computing the discrete-time *analytical* signal of the measured signal in (4.3.2) [Mar99],

$$x_a(n) = x(n) + j\mathsf{H}\{x(n)\} = a(n)e^{i(2\pi\frac{2v}{c}f_cT_{prf}-\varphi)} \tag{4.3.3}$$

where $x_a(n)$ denotes the corresponding analytical signal of $x(n)$, and $\mathsf{H}\{\cdot\}$ the *Hilbert transform* operation. Alternatively, the complex data can be generated using *Quadrature demodulation* [Jen96a].

Since the time between subsequent emitted pulses is determined by the depth of the point of interest, the f_{prf} is determined by the depth of that point: emission of the next burst is only allowed if the returned signal of the previous burst has been received, otherwise *aliasing* in depth will occur. The largest depth d_{max} into the body that can be investigated is a function of c and f_{prf}, defined in (3.1.2). When the Doppler frequency shift exceeds a limit defined by the Nyquist theorem (which equals $f_{prf}/2$), distortion of the signal takes place whereby the signal wraps itself up and appears to artificially change direction. Similarly, velocities higher than those related to Nyquist limit reappear as other, incorrect, velocities on the display. This phenomenon is known as *velocity aliasing.* The peak velocity that can be correctly resolved by the PW system is limited by the f_{prf} and therefore by the depth of the point of interest, the greater depth, the lower the f_{prf}. As discussed in Chapter 3, for the autocorrelation estimator (also termed KAT or UWLP methods as in Chapter 2), there exists a relationship between the maximum detectable axial velocity v_{Nyq} in (3.1.1) and the

maximum observable depth in (3.1.2),

$$v_{max} = \frac{c^2}{8 d_{max} f_c} \,. \tag{4.3.4}$$

4.4 Conclusion

This chapter presents a short overview of the theoretical background of ultrasound wave propagation and wave interaction with human tissues. After explaining the basic principles of transducer, beamforming and resolution, then, the discussion is focused on pulsed wave systems which are widely employed in CFI.

Chapter 5

EFFICIENT IMPLEMENTATION OF CLUTTER EIGENFILTERS

In this chapter, one of the classical challenges involved in CFI will be discussed, namely clutter rejection. First of all, a brief introduction about clutter and clutter rejection is given, followed by the literature review of existing clutter filters. Then, an efficient implementation of the recently developed eigenfilters using a fast subspace tracking technique is introduced, without degrading the performance as compared to employing conventional block EVD/SVD based eigenfilters.

5.1 Clutter Rejection

In ultrasound Doppler blood flow measurements, the backscattered signals from the moving blood scatterers are corrupted by interference signals, termed *clutter*, originating from the stationary or slowly-moving tissue such as vessel walls, and from stationary reverberations. [Jen96a, EM00, EFPF97, Sch01]. The measured ultrasonic signal resulting from the n^{th} pulse at depth k, denoted $r(k,n)$, can thus be well modelled as consisting of three statistically independent components [BTK02], i.e.,

$$x(k,n) = c(k,n) + b(k,n) + w(k,n), \tag{5.1.1}$$

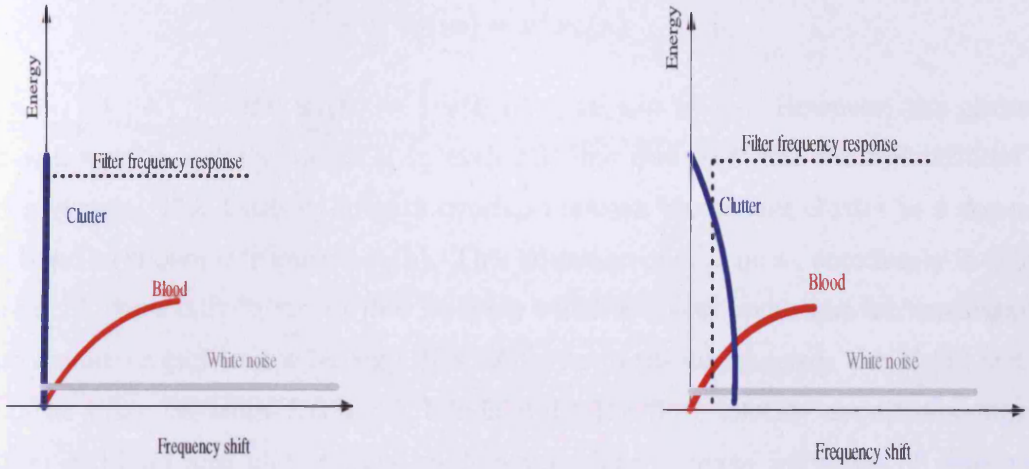

Figure 5.1. The frequency spectra of clutter, blood and noise contained in demodulated complex RF data, assuming the Doppler shift is positive for motion towards probe. The dotted line represents an ideal high-pass filter, (a) with stationary tissue; (b) with slow-moving tissue.

where $c(k,n)$, $b(k,n)$ and $w(k,n)$ denote the clutter, the blood and the additive noise components, respectively. Typically, the clutter signals are 20 - 60 dB stronger than the backscattered signals from the blood scatters [HvdVD+91, Jen93b, EM00]. On the other hand, the echoes scattered from rapidly moving blood cells have larger frequency shifts than the echoes scattered from slowly moving tissue. Figure 5.1 depicts the frequency spectra of the three components with or without moving tissue. For clutter which originates from the stationary tissue, shown in Figure 5.1 (a), the clutter component will remain identical in each RF line within each LOS. As a result, the stationary clutter signals can be filtered out by using a

simple difference filter (also called *stationary echo cancelling*) [Jen93b], i.e.,

$$y_k(n) = \mathbf{a}^T \mathbf{x}_k(n) \tag{5.1.2}$$

where $\mathbf{a} = \begin{bmatrix} 1 & -1 \end{bmatrix}^T$ and $\mathbf{x}_k(n) = \begin{bmatrix} x(k,n) & x(k,n-1) \end{bmatrix}^T$. However, the clutter component will not be strictly identical in each RF line due to tissue motion induced by the pulsating vessels. This leads to spectra overlap between blood and clutter in a common frequency band as shown in Figure 5.1 (b). This situation occurs quite commonly in blood flow measurement, especially in *strain-flow imaging* which is a new technique for investigating the vascular dynamics and tumor biology [KHTI03]. As in tumor imaging, the blood and clutter echoes often share the same frequency bands under low flow velocity conditions, making the separation of blood and clutter very challenging. The adverse influence of clutter can be reduced by minimizing the size of the echo sample volume, but even if the entire sample volume is inside a blood vessel, the unavoidable clutter from reverberations and transducer side lobes will affect the signal [KHTI03]. Furthermore, blood velocities are commonly estimated by using the autocorrelation method [KNKO85]. To obtain unbiased blood velocity estimates, the clutter signals need to be attenuated down to the thermal noise level and an efficient clutter filter must be applied before the estimation. Since clutter filters operate along the slow time axis, only $4 - 20$ echo samples are available for high pass filtering to maintain acceptable frame rate [EM00].

Thus, an ideal clutter filter should exhibit the following properties:

- Narrow transition band;
- Being adaptive to non-stationary clutter;
- Not reducing the limited available data samples;
- Not removing blood component.

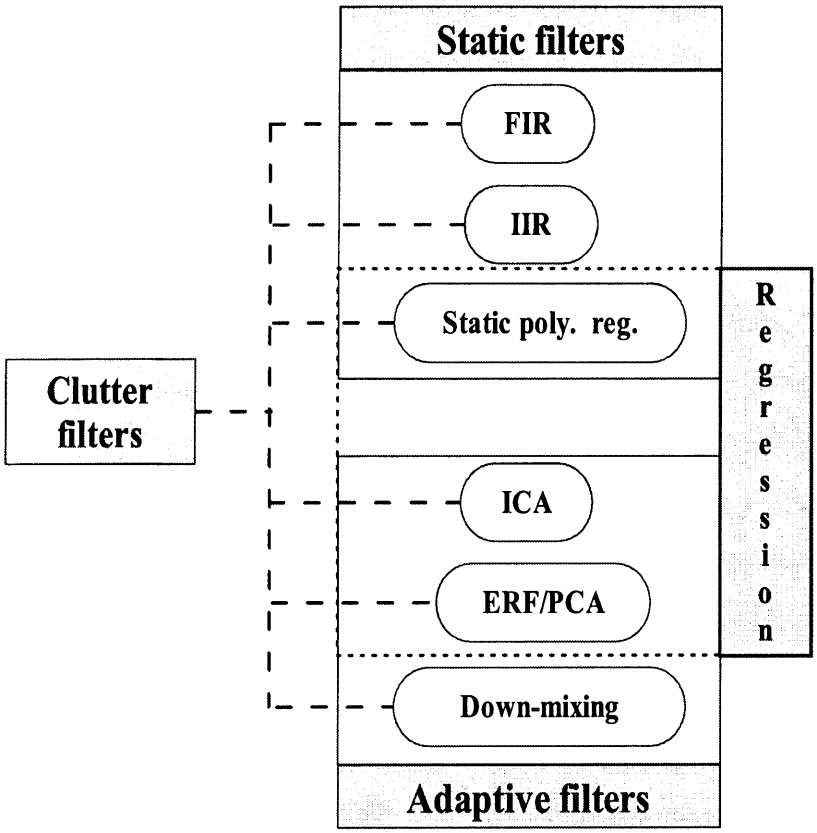

Figure 5.2. Classification of clutter filters.

The above facts and requirements make the design of an efficient clutter filter very challenging and as a result the problem has received significant attention over the last decades. In general, these filters can be classified into *static clutter filters* [HvdVD+91, Jen93b, PAB94, TH94, KL95] and *adaptive clutter filters* [BHR95, LBH97, Tor97, BT97, BTK02, KHTI03, KF02, YMK03, Kad02, GT02, GNT03, TWF+04], As summarized in Figure 5.2, the *static clutter filters* mainly comprise FIR, infinite impulse response (IIR) and polynomial regres-

sion filters; and the *adaptive clutter filters* mainly include independent component analysis (ICA)-based filters, eigenvector regression filters (ERF), which sometimes are also termed principal component analysis (PCA)-based filters [GT02, GNT03], as well as a down-mixing method [BTK02]. Of these methods, the *static polynomial regression* filters, the ERF filters and the ICA-based filters are also classified as *regression* filters, which will be discussed later. The PCA and ICA are two common methods of the blind source separation (BSS) family. More details about BSS can be found in ([Car98, Sto02], and the references therein).

Static clutter filters

As discussed above, various static clutter filters, such as FIR, IIR and polynomial regression filters, have been proposed to suppress the clutter from the backscattered signals (e.g., see [HHR91, PAB94, KL95, BTK02], and the references therein). To get a narrower transition band, both the FIR and IIR filters require higher order, which will further reduce the valid echo samples by a factor of the order of the filters. Moreover, the FIR filters need a higher order than the IIR filters to achieve an equivalent narrow transition band [OSB99]. It is worth noting that the most commonly used estimator in CFI, the autocorrelation estimator, will suffer higher variance when fewer valid data samples are used and the variance of it is inversely proportional to the number of valid outputs of the employed filter, as implied in (2.2.15) (the autocorrelation estimator is also termed UWLP in Chapter 2). Furthermore, the conventional FIR or IIR high pass filters will undiscriminatingly remove low frequency components. The obvious drawback is that the filters also filter out the signal from the low velocity (low Doppler shift) blood flow near vessel walls which is a region of great interest for detecting flow anomalies leading to atheroma formation [TMLI04].

Later, in [HvdVD+91, KL95], Hoeks and Kadi *et al.* developed regression filters different from FIR or IIR filters being based on the assumption that signals are a superposition of sinusoids. Regression filters operate on the assumption that the slowly varying clutter

component in the Doppler signal can be approximated by a polynomial of a given order, which in turn can be determined by performing least-squares regression analysis. The resulting filters are thus termed *polynomial regression filters.* Once approximated, this component can then be subtracted from the Doppler signal so that the contribution from blood-flow can be retrieved and analyzed. But this filter is still static, being independent of the input data sequence as shown in the following derivation. Mathematically, at depth k, the filtered data sample can be written as

$$\begin{aligned} c(k,n) &= \sum_{p=0}^{P} a_p n^p \\ y_k(n) &= x(k,n) - c(k,n), \quad n = 1,2,\cdots,N \end{aligned} \tag{5.1.3}$$

where $c(k,n)$ is the approximated clutter component, $\{a_p\}$ the set of regression model coefficients, P the regression order and N the number of data samples. Fitting a polynomial of degree P to a set of data points $\{x(k,n)\}$, $n = 1,2,\cdots,N$ involves finding a set of coefficients a_p, $p = 0,1,\cdots,P$, such that the sum of the squared differences between the actual data and the model

$$\epsilon^2 = \sum_{n=1}^{N} \left(x(k,n) - \sum_{p=0}^{P} a_p n^p \right)^2 \tag{5.1.4}$$

is minimized, which is equivalent to

$$\begin{aligned} \frac{\partial \epsilon^2}{\partial a_i} &= 0 \\ \frac{\partial^2 \epsilon^2}{\partial a_i^2} &> 0, \quad i = 0,\cdots,P, \end{aligned} \tag{5.1.5}$$

leading to the following set of linear equations

$$\sum_{n=1}^{N} \left(x(k,n) - \sum_{p=0}^{P} a_p n^P \right) n^i = 0, \quad i = 0,\cdots,P \tag{5.1.6}$$

which can be rearranged as

$$\sum_{p=0}^{P}\sum_{n=1}^{N} n^i n^p a_p = \sum_{n=1}^{N} n^i x(k,n). \tag{5.1.7}$$

Furthermore, by introducing the matrix and vector notations

$$\mathbf{\Gamma} = \begin{pmatrix} 1^0 & 1^1 & \cdots & 1^P \\ 2^0 & 2^1 & \cdots & 2^P \\ \vdots & \vdots & & \vdots \\ N^0 & N^1 & \cdots & N^P \end{pmatrix}, \quad \mathbf{a} = \begin{pmatrix} a_0 \\ a_1 \\ \vdots \\ a_P \end{pmatrix}, \quad \mathbf{x}_k = \begin{pmatrix} x(k,t) \\ x(k,t+1) \\ \vdots \\ x(k,t+N-1) \end{pmatrix} \tag{5.1.8}$$

at discrete time t, (5.1.7) can be rewritten as

$$\left(\mathbf{\Gamma}^T\mathbf{\Gamma}\right)\mathbf{a} = \mathbf{\Gamma}^T\mathbf{x}_k \tag{5.1.9}$$

or

$$\mathbf{a} = \left(\mathbf{\Gamma}^T\mathbf{\Gamma}\right)^{-1}\mathbf{\Gamma}^T\mathbf{x}_k. \tag{5.1.10}$$

For given N and P, substituting (5.1.10) into (5.1.3) will make $y_k(n)$ available. As can be seen, the polynomial regression filters do not shorten the length of valid data sequences, and are in this sense different from FIR or IIR filters. In [KL95], Kadi *et al.* further confirmed in their work that regression filters could offer significantly better performance than step-initialized IIR filters under heavy clutter conditions. It should be noted the evaluation of the matrix $\left(\mathbf{\Gamma}^T\mathbf{\Gamma}\right)^{-1}\mathbf{\Gamma}^T$ is computationally demanding. However, it is totally independent of the input sequence $\mathbf{x}_k$ and its elements are only determined by P and N. Because the clutter characteristics in RF signal vary, also due to the nonstationary tissue motions from cardiac activities and/or respiration and the transducer/patient movement [TH94], a static filter cannot remove the clutter effectively.

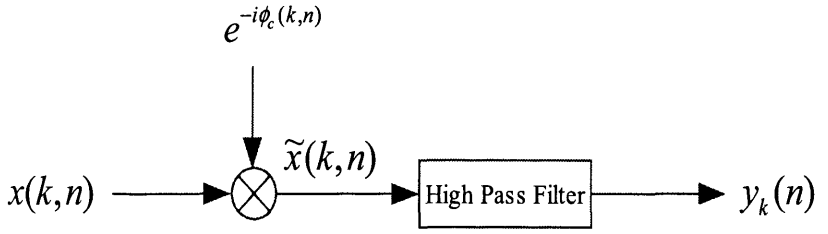

Figure 5.3. Down-mixing methods, where $\phi_c(k,n)$ is the estimated clutter frequency.

Adaptive clutter filters

In contrast to static clutter filters discussed above, the filtering operation depends on the characteristics of the clutter signal, and the resulting filters are termed *adaptive clutter filters*. The down-mixing methods, the ERF and the PCA/ICA methods are thus designed to filter the clutter adaptively.

The down-mixing methods were developed to shift adaptively clutter to be centered around zero frequency after estimating the clutter frequency at each location before applying a high pass filter [TH94, BHR95], as depicted in Figure 5.3. The down-mixing methods can suppress the clutter well when the clutter is of a) relatively high amplitude; b) narrow bandwidth and c) low mean frequency [BHR95]. However, this method cannot provide sufficient clutter rejection when several tissue velocities exist in the backscattered signals, owing to acceleration or deceleration of tissues. To compensate for this, a down-mixing method with varying phase increments computed from a clutter correlation matrix was recently proposed [BTK02], showing an improved performance in dealing with accelerated tissue motion.

However, its performance highly depends on how reliably the clutter correlation matrix can be estimated. It should also be noted that the computational complexity is particularly high.

In [LBH97], Ledoux *et al.* proposed a clutter rejection filter for multiline Doppler modalities based on the SVD. This method was further developed using a stochastic signal model [BT97, BTK02], termed *eigenvector regression filter*, in which the orthonormal basis functions for the regression filter are computed with the SVD or the *discrete Karhunen-Loève transform* (DKLT)[1] corresponding to the clutter statistics. In the case of uniform tissue motion induced by probe movement over an entire *region of interest* (ROI), Bjaerum *et al.* [BTK02] successfully demonstrated that the ERF outperformed the polynomial regression filter. Later, Kruse *et al.* [KF02] extended the ERF to deal with high blood-to-clutter ratios (BCR) by training the correlation matrix based on signal correlation. Recently, the ERF was also applied for strain-flow imaging [KHTI03, TMLI04]. Theoretically, the ERF can provide maximum clutter suppression with a given filter order because of its best mean-square approximation of the clutter. Clearly, it can still potentially remove the flow signal close to the clutter velocity. Furthermore, the application of ERF in a practical system is currently limited because of its high computational complexity [LBH97, BT97, BTK02].

Recently, two BSS-based approaches to the problem of adaptive clutter filtering were proposed, the PCA and the ICA techniques [Kad02, GT02, GNT03, TWF+04]. As pointed out earlier, the PCA method is essentially identical to the ERF in the sense that both methods are based on the decomposition of a second-order ensemble data vector as the sum of its projections onto the principal axis of its covariance matrix. Basically, the ERF/PCA methods decompose the input data sequence into a set of orthogonal basis functions. Because

[1]This transform is also commonly referred to as *principal component analysis* (PCA) or the Hotelling-transform. Hotelling was the first to derive the transformation of discrete variables into uncorrelated coefficients. He referred to it as the *method of principal components.* The analogous transformation for transforming continuous data was discovered by *Karhunen* and *Loève* [GW02]

orthogonality indicates that the basis functions are uncorrelated but does not imply that they are statistically independent unless the functions are also Gaussian or otherwise distributed random variables for which the third and higher order moments are zero [Chi97]. If an orthogonal decomposition is performed, the resulting basis functions may be orthogonal but not mutually independent. As a result, multiple independent source signals may project onto the same orthogonal basis vector, leading to incomplete source signal separation that makes clutter filtering via projection operations difficult. The ICA method is different from the ERF/PCA in the sense that it assumes that source signals are not only uncorrelated but also *mutually independent* [Car98, Sto02]. The ICA basis functions are extracted by maximizing the entropy in the joint probability density functions (PDF) of the basis vectors. If a set of signals has a maximum entropy PDF, it is implied that the signals are mutually independent. Of the existing ICA algorithms, the Jade algorithm [Car98] is perhaps the most common one. The method first determines the input data ensemble's DKLT. The decomposition is then whitened, meaning that each basis function is magnitude normalized. The eigenpairs of the fourth order cumulants of the whitened basis functions are calculated, and the eigenpairs are diagonalized with a unitary matrix. Finally, the matrix that separates the independent source signals from the data ensemble is determined from the whitened and unitary matrices. However, it should be noted that in a comparison study of the PCA and ICA methods, Gallippi *et al.* [GT02] showed that the first-order PCA method outperformed the ICA method. This could happen if the clutter and blood components are not independent with each other, then the ICA may find it difficult to separate the signals and the PCA may turn out to be a better choice. As a result, it is really difficult to choose between the ICA and the PCA methods for a given scenario.

In view of the literature review above, there obviously exists more work to be done to obtain a better understanding of an optimal solution for clutter rejection. As the review shows, currently, the ERF/PCA and possibly the ICA methods seem more promising than

other discussed methods for clutter rejection. In terms of the implementation of these methods, the conventional evaluation of block SVD involved in the ERF/PCA, and the first stage of ICA, is computationally complex, and renders real-time CFI impractical. As a result, next, efforts will be focused on the efficient evaluation of the SVD in association with the implementation of the ERF.

5.1.1 Eigenvector Regression Filter

Recalling (5.1.1), the $(2K+1) \times N$ matrix $\mathbf{X}_k$ centered at depth k is introduced, formed as

$$\mathbf{X}_k = \left[\begin{array}{ccc} \mathbf{x}_{k-K} & \cdots & \mathbf{x}_{k+K} \end{array} \right]^H , \tag{5.1.11}$$

with

$$\mathbf{x}_k = \left[\begin{array}{ccc} x(k,t) & \cdots & x(k,t+N-1) \end{array} \right]^H , \tag{5.1.12}$$

where $(\cdot)^H$ denotes conjugate transpose (Hermitian), and N the number of available temporal slow-time samples at discrete time t. Define the $N \times N$ correlation matrix of the measured signal assumed wide-sense stationary, for the k^{th} depth, as

$$\mathbf{R}_k = E\left\{ \mathbf{x}_k \mathbf{x}_k^H \right\} , \tag{5.1.13}$$

where $E\{\cdot\}$ denotes statistical expectation. As the correlation matrix is typically unknown and only limited samples are available, an estimate of the correlation matrix can be formed using the reflected signal from $\pm K$ depths offset from the k^{th} depth,

$$\hat{\mathbf{R}}_k = \frac{1}{L} \sum_{l=k-K}^{k+K} \mathbf{x}_l \mathbf{x}_l^H , \tag{5.1.14}$$

where $L = 2K+1$ denotes the number of depths considered, with typically $L \gg N$. Furthermore, $\hat{\mathbf{R}}_k$ can be decomposed as

$$\hat{\mathbf{R}}_k = \mathbf{U}_k \mathbf{\Lambda} \mathbf{U}_k^H , \tag{5.1.15}$$

where $\mathbf{\Lambda}$ is a diagonal matrix, containing the eigenvalues, λ_n, for $n = 0, \cdots, N-1$, non-increasingly lying along the diagonal, and $\mathbf{U}_k$ is a unitary matrix formed from the corresponding N eigenvectors. As the eigenvectors corresponding to the r largest eigenvalues can be viewed as spanning the clutter subspace, the eigenfilters optimally attenuating the influence of the clutter can be formed as the projection onto the space orthogonal to the one spanned by the clutter eigenvectors (see, e.g., [LBH97, BTK02, KHTI03, KF02, YMK03]), as illustrated in Figure 1.1. Let

$$\mathbf{A}_k = \left[\begin{array}{ccc} \mathbf{u}_0 & \cdots & \mathbf{u}_{r-1} \end{array} \right], \tag{5.1.16}$$

where

$$\mathbf{u}_i = [u_i(0), \cdots, u_i(N-1)]^T \tag{5.1.17}$$

denotes the eigenvector corresponding to the i^{th} eigenvalue. Alternatively, $\mathbf{A}_k$ can also be obtained by evaluating the SVD of $\mathbf{X}_k$. Then, the linear eigenfiltering operation is defined by

$$\mathbf{\Pi}^{\perp}_{\mathbf{A}_k} = \mathbf{I} - \mathbf{A}_k \mathbf{A}_k^H, \tag{5.1.18}$$

where $\mathbf{I}$ denotes the identity matrix with proper dimension, and the filtered signal is formed as

$$\mathbf{y}_k = \mathbf{\Pi}^{\perp}_{\mathbf{A}_k} \mathbf{x}_l \ . \tag{5.1.19}$$

The frequency response of the linear filtering operation in (5.1.19) becomes [Tor97]

$$H_{\mathbf{A}_k}(\omega) = 1 - \frac{1}{N} \sum_{i=0}^{r-1} \left| \sum_{n=0}^{N-1} \mathbf{u}_i(n) e^{-jn\omega} \right|^2 . \tag{5.1.20}$$

A typical example of the resulting filters is illustrated in Figure 5.4, where CNR denotes the clutter to noise ratio and $f_{clutter}$ the simulated frequency of the dominant clutter component. As is clear from the figure, the ERF shows steeper cut-off slopes as compared to the FIR filters. Furthermore, the longer the data vector length, N, the steeper the transition band.

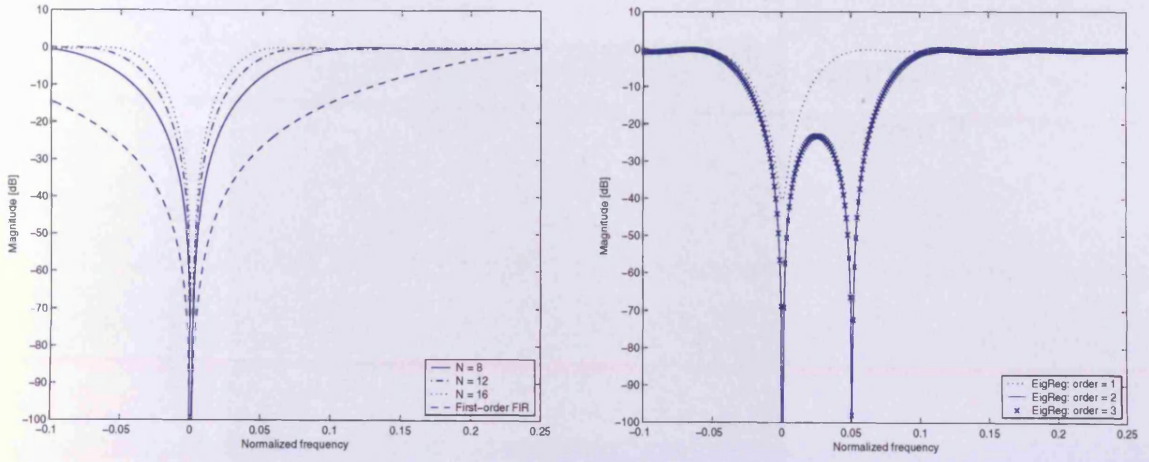

(a) (b)

Figure 5.4. Frequency responses with variable parameters: (a) A first-order ERF with variable ensemble data length N, $f_{clutter} = 0$, $CNR = 40$ dB; (b) ERF with variable order. $f_{clutter} = [0 \;\; 0.05]$, $N = 16$, $CNR = 40$ dB.

In Figure 5.4 (b), we simulate clutter with frequencies $f_{clutter} = [0 \;\; 0.05]$. As we can see, a first-order ERF will only remove the clutter with zero frequency, while a second-order ERF can provide satisfactory suppression for the clutter presented at both frequency locations.

It is worth noting that the choice of L in (5.1.14) reflects the size of the stationary data segment and should be selected as the range of depths over which the statistical properties of the clutter signal can be assumed to be approximately constant [BTK02]. If the statistics change as a function of spatial coordinates, the filter obtained from an LOS with varying statistics will not provide sufficient performance. As the clutter statistics vary over depth in many physiological cases, the correlation matrix should be properly formed to model the signal statistics within a stationary data segment. An illustration of this fact is shown in Figure 5.5. Typically, the size of the stationary data segment depends on factors such as the pulse bandwidth, sampling frequency, SNR, as well as the region size of flow and

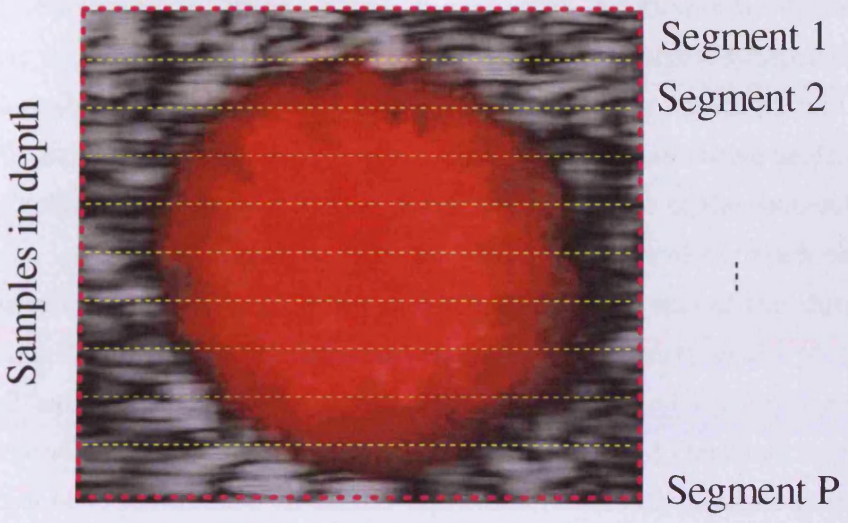

Figure 5.5. Cross section of a blood vessel buried in tissue. Each data segment should be selected with constant statistical properties of the clutter signal.

clutter. However, computing the sample correlation matrix $\hat{\mathbf{R}}_k$ and the corresponding EVD, or alternatively computing the SVD of stationary data segment $\mathbf{X}_k$, is often computationally prohibited in clinical diagnosis. To alleviate this problem, we proceed to introduce an efficient subspace tracking technique as an efficient way to form the eigenfilters.

Subspace tracking algorithms play an important role for many subspace-based high-resolution methods, and the literature on the topic is substantial (see, e.g., [CG90, Yan95, Str97, BRD04, MH98] and the references therein). Typically, subspace algorithms are applied to temporally slow-varying signals, formed into time-dependent data blocks

$$\mathbf{X}_t = \begin{bmatrix} \mathbf{x}_t & \cdots & \mathbf{x}_{t-L+1} \end{bmatrix}^H, \tag{5.1.21}$$

where $\mathbf{x}_t$ is a column vector. These algorithms exploit the fact that typically only a few dominant singular vectors, say 2-4, are needed to span the noise or signal subspace. Similarly, we exploit the fact that the clutter signal has a slowly time-varying nature both in the temporal and spatial domain. Thus, the clutter statistics between two consecutive depth positions will not change significantly, thereby enabling an efficient evaluation of the consecutive SVDs using a subspace tracking technique. Herein, we propose to recursively track the $r_{\max} < \frac{1}{2}N$ dominant eigenvectors, where $r_{\max}$ is an upper bound on the size of the clutter filter, and then only using the $r \leq r_{\max}$ most dominant eigenvectors to construct the projection matrix in (5.1.18). Then, given the filtered signal in (5.1.19), the blood velocity for each depth of interest is generally estimated using a correlation-based method [Jen96a]. It is worth noting that the choice of r, the number of clutter eigenvectors actually used, is both difficult and critical. If selected as $r = r_0 + 1$, where r_0 is the *optimal* choice, the filter will suppress a large part of the blood signal. However, if $r = r_0 - 1$, a strong clutter component will remain in the data, severely distorting the resulting velocity estimate. Additionally, to take the spatially varying clutter statistics into account, the choice of r should typically be allowed to vary over depth; we note that the proposed technique allows for such local variations as long as only $r \leq r_{\max}$ eigenvectors are required.

5.1.2 An Efficient Clutter Filter Implementation via Subspace Tracking

Given the SVD factorization

$$\mathbf{X}_k = \mathbf{V}_k \mathbf{\Sigma} \mathbf{U}_k^H \ , \tag{5.1.22}$$

where $\mathbf{V}_k \in \mathbb{C}^{L\times N}$ and $\mathbf{U}_k \in \mathbb{C}^{N\times N}$ are unitary matrices and $\Sigma \in \mathbb{R}^{N\times N}$ is a non-negative diagonal matrix,

$$\mathbf{\Sigma} = \begin{bmatrix} \delta_0 & & \\ & \ddots & \\ & & \delta_{N-1} \end{bmatrix} \tag{5.1.23}$$

with $\delta_0 \geq \delta_1 \geq \cdots \geq \delta_{N-1} \geq 0$. Thus, the r dominant singular vales are $\{\delta_0, \delta_1, \cdots, \delta_{r-1}\}$, and the associated r dominant left singular vectors and the r dominant right singular vectors are the r first columns of the matrix $\mathbf{V}_k$ and the r first columns of the matrix $\mathbf{U}_k$, respectively. As discussed in the previous section, to enable the use of locally computed eigenfilters, the SVD of stationary data segment $\mathbf{X}_k$ needs to be evaluated for a number of depths. Each such evaluation using the SVD[2] requires $4LN^2 + 8N^3$ operations [GV96], preventing the method from currently being practically applicable. To avoid the full computation of the SVD, one can use the classical sequential bi-iteration SVD algorithm, as summarized in Table 5.1, to track recursively the dominant clutter subspace [Str97]. As the clutter component will vary slowly over depth, one can view the data matrix $\mathbf{X}_k$ in (5.1.11) centered at depth k as a depthwise update from $\mathbf{X}_{k-1}$ at depth $k-1$, allowing the SVD of $\mathbf{X}_k$ to be approximated and updated just by replacing the iteration depth index k as shown in Table 5.1. Here, $\mathbf{I}_{r_{max}}$ denotes an $r_{max} \times r_{max}$ identity matrix. This algorithm generates two auxiliary matrices $\mathbf{Q}_A(k) \in \mathbb{C}^{N\times r_{max}}$ and $\mathbf{Q}_B(k) \in \mathbb{C}^{L\times r_{max}}$. It has been shown that the columns of $\mathbf{Q}_A(k)$ and $\mathbf{Q}_B(k)$ will converge to the r_{max} dominant right and left singular vectors, respectively. Furthermore, both $\mathbf{R}_A(k)$ and $\mathbf{R}_B(k)$ will converge to a diagonal matrix containing the r_{max} largest singular values. Therefore, the r first columns of $\mathbf{Q}_A(k)$ can be used to approximate $\mathbf{A}_k$ in (5.1.16). As we discussed previously, the choice of r is important and critical, and is in itself an interesting topic. A detailed description of the sequential bi-iteration SVD

[2]Computing the correlation matrix estimate in (5.1.14) together with the EVD requires approximately the same number of operations.

Table 5.1. Sequential bi-iteration SVD algorithm

Initialize: $\mathbf{Q}_A(0) = \begin{bmatrix} \mathbf{I}_{r_{max}} \\ \cdots \\ \mathbf{0} \end{bmatrix}$		
For each depth step Do:		
First iteration:		Complexity
$\mathbf{B}_k = \mathbf{X}_k \mathbf{Q}_A(k-1)$	matrix product	$8NLr_{max}$
$\mathbf{B}_k = \mathbf{Q}_B(k)\mathbf{R}_B(k)$	skinny QR factorization	$19Lr_{max}{}^2$
Second iteration:		
$\mathbf{A}_k = \mathbf{X}_k^H \mathbf{Q}_B(k)$	matrix product	$8NLr_{max}$
$\mathbf{A}_k = \mathbf{Q}_A(k)\mathbf{R}_A(k)$	skinny QR factorization	$19Nr_{max}{}^2$

algorithm can be found in [Str97]. This method is very robust, but the main drawback is the high complexity with the dominant cost of $16NLr_{max}$, where $r_{max} < \frac{1}{2}N \ll L$ in practice.

Fortunately, this algorithm has been further developed (see, e.g., [CG90, Yan95, Str97, BRD04, MH98] and the references therein). Recently, Badeau *et al.* [BRD04] derived a fast tracking approach termed the *sliding window adaptive* SVD (SWASVD) algorithm which showed excellent performance in the context of frequency estimation, having computational complexity with dominant cost of $23(L+N)r_{max}^2$ which is less than $16NLr_{max}$. A number of other, yet more efficient methods, also exist, having complexity $\mathcal{O}(Nr_{max})$ (see, e.g., [BRD04]). However, the choice of method should be done with some care depending on the acceptable level of accuracy and error propagation. Herein, the SWASVD method is revised and will be applied to the clutter subspace tracking problem. As pointed out

previously, the clutter subspace tracking problem arises in a spatial domain, different from conventional subspace tracking which is normally applied in a temporal domain. As a result, this method is accordingly revised to fit the spatial subspace tracking problem, the resulting method is termed the R-SWASVD algorithm. It is noteworthy that the R-SWASVD is essentially identical to the SWASVD algorithm [BRD04], except the opposite way of updating the RF data matrix in (5.1.24) at each depth step in the spatial domain resulting in the difference between the derivations of the R-SWASVD algorithm and the SWASVD algorithm. The derivation of the R-SWASVD algorithm is presented next. More details including the complete derivation of the SWASVD algorithm can be found in [BRD04].

Consider the compressed data vector, given the depthwise update structure of the data matrix $\mathbf{X}_k$ defined in (5.1.11) and the vector $\mathbf{x}_k$ at depth k defined in (5.1.12), and notice that

$$\begin{bmatrix} \mathbf{x}_{k-K-1}^H \\ \cdots\cdots\cdots\cdots \\ \mathbf{X}_k \end{bmatrix} \mathbf{Q}_A(k-1) = \begin{bmatrix} \mathbf{X}_{k-1} \\ \cdots\cdots\cdots \\ \mathbf{x}_{k+K}^H \end{bmatrix} \mathbf{Q}_A(k-1) \tag{5.1.24}$$

which can be further simplified as

$$\begin{bmatrix} \times\cdots\times \\ \cdots\cdots\cdots\cdots \\ \mathbf{B}_k \end{bmatrix} = \begin{bmatrix} \mathbf{X}_{k-1}\mathbf{Q}_A(k-1) \\ \cdots\cdots\cdots \\ \mathbf{h}_{k+K}^H \end{bmatrix}, \tag{5.1.25}$$

where the symbol $\times$ denotes uninteresting elements, and

$$\mathbf{h}_{k+K} = \mathbf{Q}_A^H(k-1)\,\mathbf{x}_{k+K}\,. \tag{5.1.26}$$

Next, use the low-rank approximation of $\mathbf{X}_k$ as

$$\begin{aligned}\hat{\mathbf{X}}_k &= \left(\mathbf{Q}_B(k)\mathbf{Q}_B^H(k)\right)\mathbf{X}_k \\ &= \mathbf{Q}_B(k)\mathbf{Q}_B^H(k)\mathbf{Q}_B(k)\mathbf{A}^H(k) \\ &= \mathbf{Q}_B(k)\mathbf{A}^H(k) \\ &= \mathbf{Q}_B(k)\mathbf{R}_A^H(k)\mathbf{Q}_A^H(k) \end{aligned} \tag{5.1.27}$$

which corresponds to the projection of the columns of $\mathbf{X}_k$ onto the subspace spanned by the columns of $\mathbf{Q}_B(k)$. As a result,

$$\hat{\mathbf{X}}_{k-1}\mathbf{Q}_A(k-1) = \mathbf{Q}_B(k-1)\mathbf{R}_A^H(k-1)\ . \tag{5.1.28}$$

Then, use $\hat{\mathbf{X}}_{k-1}$ to replace $\mathbf{X}_{k-1}$ in (5.1.25) yields

$$\begin{bmatrix} \times\cdots\times \\ \cdots\cdots\cdots \\ \mathbf{B}_k \end{bmatrix} \simeq \begin{bmatrix} \mathbf{Q}_B(k-1)\mathbf{R}_A^H(k-1) \\ \cdots\cdots\cdots\cdots\cdots \\ \mathbf{h}_{k+K}^H \end{bmatrix}\ . \tag{5.1.29}$$

Similarly, notice that

$$\begin{bmatrix} \mathbf{x}_{k-K-1} & \vdots & \mathbf{X}_k^H \end{bmatrix} \begin{bmatrix} 0\cdots 0 \\ \cdots\cdots\cdots \\ \mathbf{Q}_B(k) \end{bmatrix} = \begin{bmatrix} \mathbf{X}_{k-1}^H & \vdots & \mathbf{x}_{k+K} \end{bmatrix} \begin{bmatrix} 0\cdots 0 \\ \cdots\cdots\cdots \\ \mathbf{Q}_B(k) \end{bmatrix}\ , \tag{5.1.30}$$

the left hand side of which is identical to $\mathbf{A}_k$ according to the definition in Table 5.1. Thus, (5.1.30) becomes

$$\mathbf{A}_k = \begin{bmatrix} \mathbf{X}_{k-1}^H & \vdots & \mathbf{x}_{k+K} \end{bmatrix} \begin{bmatrix} 0\cdots 0 \\ \cdots\cdots\cdots \\ \mathbf{Q}_B(k) \end{bmatrix}\ . \tag{5.1.31}$$

Moreover, multiply $\mathbf{Q}_A^H(k-1)$ on both sides of (5.1.31) leading to

$$\mathbf{R}_B^H(k) = \left[\begin{array}{c:c} \mathbf{Q}_A^H(k-1)\mathbf{X}_{k-1}^H & \mathbf{h}_{k+K} \end{array} \right] \left[\begin{array}{c} 0 \cdots 0 \\ \cdots\cdots\cdots \\ \mathbf{Q}_B(k) \end{array} \right] , \tag{5.1.32}$$

where, according to the sequential bi-iteration SVD algorithm, summarized in Table 5.1, $\mathbf{R}_B^H(k)$ satisfies

$$\begin{aligned} \mathbf{R}_B^H(k) &= \mathbf{B}_B^H(k)\mathbf{Q}_B(k) \\ &= \mathbf{Q}_A^H(k-1)\mathbf{X}_k^H\mathbf{Q}_B(k) \\ &= \mathbf{Q}_A^H(k-1)\mathbf{A}_k \ . \end{aligned} \tag{5.1.33}$$

Then, define vector

$$\begin{aligned} \mathbf{x}_{k+K}^{\perp} &= \mathbf{x}_{k+K} - \mathbf{Q}_A(k-1)\mathbf{Q}_A^H(k-1)\mathbf{x}_{k+K} \\ &= \mathbf{x}_{k+K} - \mathbf{Q}_A(k-1)\mathbf{h}_{k+K} \ , \end{aligned} \tag{5.1.34}$$

which is orthogonal to the subspace spanned by the columns of $\mathbf{Q}_A(k-1)$, thus $\mathbf{x}_{k+K}$ can be seen as the sum of two orthogonal vectors

$$\mathbf{x}_{k+K} = \mathbf{Q}_A(k-1)\mathbf{h}_{k+K} + \mathbf{x}_{k+K}^{\perp} \ . \tag{5.1.35}$$

Replacing $\mathbf{X}_{k-1}$ with $\hat{\mathbf{X}}_{k-1}$ in (5.1.31) and (5.1.32), respectively, yields

$$\mathbf{A}_k \simeq \left[\begin{array}{c:c} \mathbf{Q}_A(k-1) & \mathbf{x}_{k+K}^{\perp} \end{array} \right] \left[\begin{array}{c|c} \mathbf{R}_A(k-1)\mathbf{Q}_B^H(k-1) & \mathbf{h}_{k+K} \\ \hline 0 \cdots 0 & 1 \end{array} \right] \left[\begin{array}{c} 0 \cdots 0 \\ \cdots\cdots\cdots \\ \mathbf{Q}_B(k) \end{array} \right] \tag{5.1.36}$$

Table 5.2. Revised Sliding Window Adaptive SVD algorithm (R-SWASVD)

Initialize: $\mathbf{Q}_A(0) = \begin{bmatrix} \mathbf{I}_{r_{max}} \\ \cdots \\ \mathbf{0} \end{bmatrix}$; $\mathbf{Q}_B(0) = \begin{bmatrix} \mathbf{I}_{r_{max}} \\ \cdots \\ \mathbf{0} \end{bmatrix}$; $\mathbf{R}_A(0) = \mathbf{I}_{r_{max}}$;	
For each depth step Do:	
First iteration:	Complexity
$\mathbf{h}_{k+K} = \mathbf{Q}_A^H(k)\mathbf{x}_{k+K}$	$8Nr_{max}$
$\begin{bmatrix} \times \cdots \times \\ \cdots\cdots\cdots \\ \mathbf{B}_k \end{bmatrix} \simeq \begin{bmatrix} \mathbf{Q}_B(k-1)\mathbf{R}_A^H(k-1) \\ \cdots\cdots\cdots\cdots\cdots \\ \mathbf{h}_{k+K}^H \end{bmatrix}$	$4L{r_{max}}^2$
$\mathbf{B}_k = \mathbf{Q}_B(k)\mathbf{R}_B(k)$	$19L{r_{max}}^2$
Second iteration:	
$\mathbf{x}_{k+K}^{\perp} = \mathbf{x}_{k+K} - \mathbf{Q}_A(k-1)\mathbf{h}_{k+K}$	$8Nr_{max}$
$\mathbf{A}_k = \mathbf{Q}_A(k-1)\mathbf{R}_B^H(k) + \mathbf{x}_{k+K}^{\perp}\mathbf{q}_{B1}^H(k+K)$	$4N{r_{max}}^2$
$\mathbf{A}_k = \mathbf{Q}_A(k)\mathbf{R}_A(k)$	$19N{r_{max}}^2$

and

$$\mathbf{R}_B^H(k) \simeq \begin{bmatrix} \mathbf{R}_A(k-1)\mathbf{Q}_B^H(k-1) & \vdots & \mathbf{h}_{k+K} \end{bmatrix} \begin{bmatrix} 0 \cdots 0 \\ \cdots\cdots\cdots \\ \mathbf{Q}_B(k) \end{bmatrix} . \tag{5.1.37}$$

Let $\mathbf{q}_{B1}(k+K)$ be the column vector obtained by conjugate transposing the last row of

$\mathbf{Q}_B(k)$, thus (5.1.36) and (5.1.37) finally yield

$$\begin{aligned}\mathbf{A}_k &= \left[\begin{array}{c:c} \mathbf{Q}_A(k-1) & \mathbf{x}_{k+K}^{\perp} \end{array}\right] \left[\begin{array}{c} \mathbf{R}_B^H(k) \\ \cdots\cdots\cdots \\ \mathbf{q}_{B1}^H(k+K) \end{array}\right] \\ &= \mathbf{Q}_A(k-1)\mathbf{R}_B^H(k) + \mathbf{x}_{k+K}^{\perp}\mathbf{q}_{B1}^H(k+K) \end{aligned} \tag{5.1.38}$$

which can be factorized as

$$\mathbf{A}_k = \mathbf{Q}_A(k)\mathbf{R}_A(k) \ . \tag{5.1.39}$$

As discussed in [BRD04], the exact computation of $\mathbf{A}_k$ and $\mathbf{B}_k$ requires $16NLr_{max}$ operations as shown in Table 5.1, whereas the approximated matrices (5.1.29) and (5.1.38) can be computed in $4Lr_{max}{}^2$ and $4Nr_{max}{}^2$ operations. Therefore, introducing these approximations in the sequential bi-iteration SVD algorithm leads to the lower complexity algorithm herein termed revised SWASVD (R-SWASVD) as compared to the SWASVD proposed in [BRD04], summarized in Table 5.2.

5.1.3 Simulation Results

In this section, the computational gain and the performance of the R-SWASVD algorithm are examined. Figures 5.6 and 5.7 illustrate the computational gain of using the R-SWASVD algorithm to track the $r = r_{max} = 2$ most dominant eigenvectors of $\hat{\mathbf{R}}_k$ as compared to the use of an ordinary block based SVD algorithm and the sequential bi-iteration SVD algorithm, respectively. As is clear from the figures, the computational gain of using the R-SWASVD algorithm is significant, especially as compared to the block SVD method. Furthermore, the gain of using the R-SWASVD algorithm will strongly depend on the number of pulses used in each data vector, N, as well as the size of the block used to form the sample correlation matrix, L. To verify the clutter subspace tracking performance of the R-SWASVD algorithm in a realistic situation, RF data are generated to simulate the flow in the carotid artery,

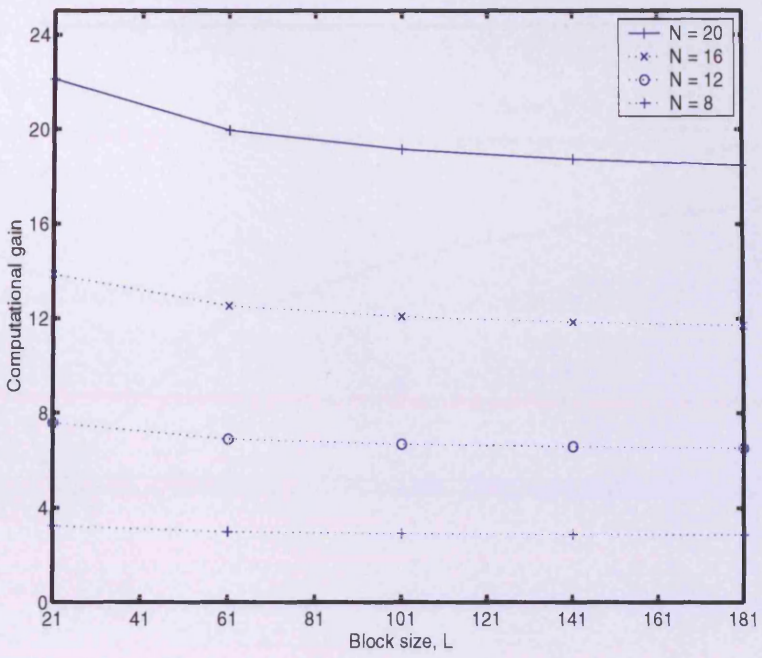

Figure 5.6. The computational gain of using the R-SWASVD algorithm as compared to the ordinary block-based SVD algorithm.

taking into account the tissue motion due to the breathing and pulsation, by using the Field II program[3] [Jen96b], with the main parameters outlined in Appendix 5.A. The upper plot in Figure 5.8 shows one of the examined RF lines, where the vertical dashed lines represent vessel walls and vessel centre. As is clear from the figure, the dominant peaks on both sides of the plot depict the strong clutter effects due to tissue motion. In this investigation, a set of $N = 20$ successive RF lines with $L = 80$ (equal to the pulse length) are used, which implies the computational gain as compared to the block-based SVD algorithm is a factor of 20, as seen in Figure 5.6. The lower part of Figure 5.8 shows the estimated velocity profiles, using the autocorrelation estimator [KNKO85], for the second-order clutter filters obtained from a

[3]Data available at: `http://www.oersted.dtu.dk/31655/?ultrasound_data/sim_car_wall.html`

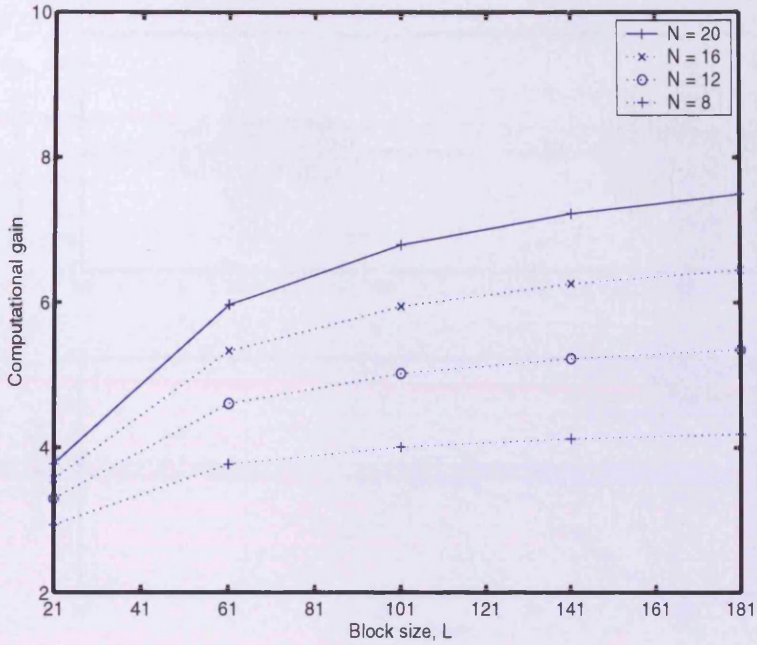

Figure 5.7. The computational gain of using the R-SWASVD algorithm as compared to the sequential bi-iteration SVD algorithm.

block-based SVD and the R-SWASVD algorithm. As seen from the figure, the R-SWASVD algorithm closely tracks the block-based SVD. It is worth noting that the center of the profile is not accurately estimated. This is likely an effect of the fixed order clutter filter; in the center of the vessel, r should typically be lower than at the vessel walls. Such variations can easily be accommodated for with the suggested approach, although further research is needed on how the filter order should be selected appropriately. This is a challenging topic for future research.

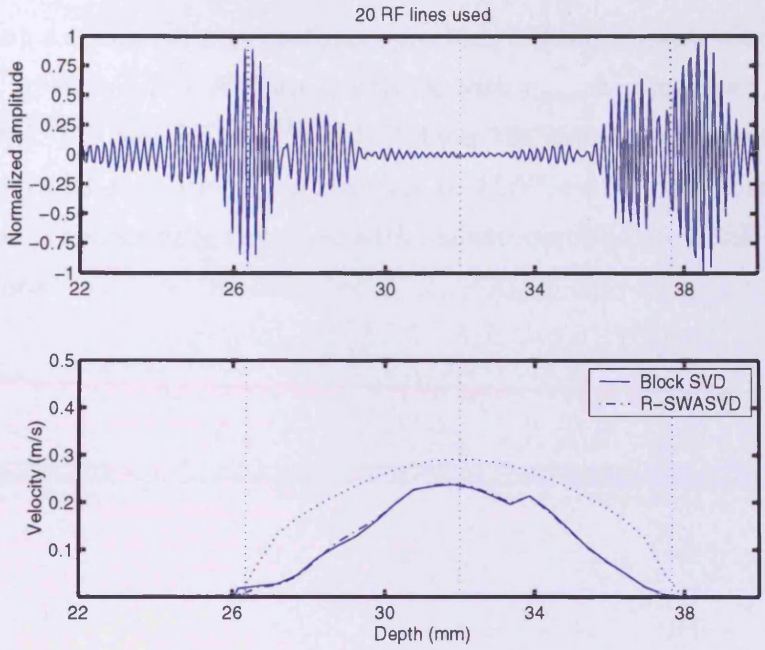

Figure 5.8. Estimated velocity profile with clutter filtering using the block-based SVD method and the R-SWASVD algorithm. The dotted curve represents the true parabolic velocity profile.

5.2 Conclusion

The clutter rejection problem is stated in this chapter, followed by the literature review of existing clutter filters which are classified into *static clutter filters* and *adaptive clutter filters*. The analysis of existing filters implies that the ERF/PCA and ICA methods are likely to be promising. In terms of the implementation of these methods, the conventional evaluation of block SVD involved in ERF/PCA, and the first stage of ICA, is computationally complex, and renders real-time CFI impractical. As a result, the rest of the chapter is focused on how to implement efficiently the ERF. Then, an efficient approach to form recursively the

clutter filters using a recent recursive subspace tracking technique is introduced. As discussed in Section 5.1.2, given an $L \times N$ data matrix $\mathbf{X}$ with r_{max} dominant singular values, the introduced R-SWASVD method significantly reduces the required computational cost down to dominant cost of $23(L+N)r_{max}^2$, in contrast to $4LN^2 + 8N^3$ using block SVD. The R-SWASVD method is successfully examined with realistic carotid flow which is simulated with the Field II toolbox.

Appendix

5.A Parameters for Simulating Blood Flow for Clutter Rejection

Transducer	convex, elevation focused array probe with 58 elements
Centre (single carrier) frequency, f_c	3.75 MHz
Sampling frequency, f_s	15 MHz
Pulse repetition frequency, f_{prf}	3.5 kHz
Sound speed (c)	1540 m/s
Pulse oscillation (M)	8
Doppler angle (DOA)	45°
RF lines (N)	20
Center of vessel	32 mm from transducer surface
Vessel radius	4 mm

Chapter 6

EXAMINING PROPOSED ESTIMATORS WITH REALISTIC DATA

In this chapter, the proposed hybrid estimator discussed in Chapter 2 and the multiple-carrier based DAVE and NLS estimators proposed in Chapter 3 are applied to blood velocity estimation. All the simulations in this chapter are performed using realistic ultrasound RF data simulated with the Field II toolbox [Jen96b].

6.1 Blood Velocity Estimation with Single Carrier

6.1.1 Examined with the Hybrid Estimator

To examine the performance of the hybrid estimator proposed in Chapter 2, initially, a single fibre-like flow which comprises 1000 blood particles lying along the vessel center and moving towards the transducer along the beam direction (pure axial velocity) with constant velocity $v = 0.5 \times v_{Nyq}$ is simulated. The details of the parameters for simulating the RF data are listed in Appendix 6.A. Figure 6.1 shows the MSE of the examined estimators as a function of the SNR at the transmission focus which is 35 mm away from the transducer surface. As is seen from the figure, the hybrid estimator uniformly exhibits better performance than the autocorrelation estimator (termed *Auto* in the figure) over the whole range of examined

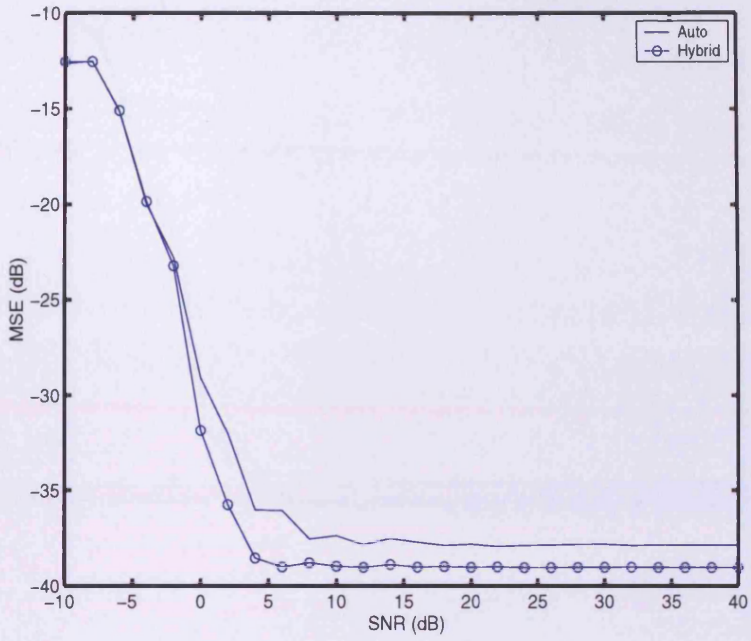

Figure 6.1. The MSE of the examined estimators as a function of the SNR, for $v = 0.5 \times v_{Nyq}$, with fibre RF data.

SNRs. Furthermore, a case with simulated laminar blood flow (consisting of 3×10^5 scatters) with parabolic profile is considered, i.e.,

$$v(r) = (1 - r^2)v_0, \tag{6.1.1}$$

where $r \in [0, 1]$ is the relative radius, and v_0 the peak velocity at the vessel center, $v_0 = 0.8 \times v_{Nyq}$, with the same parameters given in Appendix 6.A. Figure 6.2 shows the MSE of the examined estimators as a function of the SNR at the depth where the examined velocity $v = 0.5 \times v_{Nyq}$. As seen in the figure, the hybrid estimator shows preferable performance also for this case. As the data generation is somewhat time-consuming, the simulations for both the fibre and parabolic flow is limited to only 100 Monte Carlo simulations.

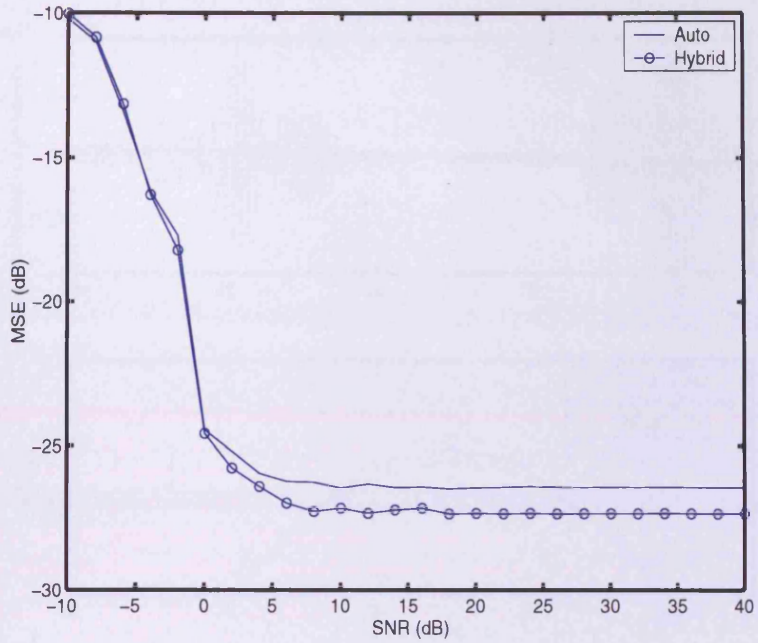

Figure 6.2. The MSE of the examined estimators as a function of the SNR, for $v = 0.5 \times v_{Nyq}$, with parabolic flow RF data.

Finally, to verify the performance of the hybrid estimator in a somewhat more realistic situation, RF data simulating the flow in the carotid artery are examined, with the parameters used identical to those outlined in Appendix 5.A, except that $N = 18$ successive RF lines are used herein (recall that the hybrid estimator considers only the case when N is an integer multiple of K [Fow02], see also Section 2.2.4.). The upper plot in Figure 6.3 shows one of the RF lines. The dominant peaks on both sides of the plot depict the strong clutter effects due to the existence of vessel walls (represented by the dashed vertical lines) and the tissue motion. To enable high quality blood velocity estimation, efficient clutter filtering must be applied prior to the velocity estimation. In this work, a second order block

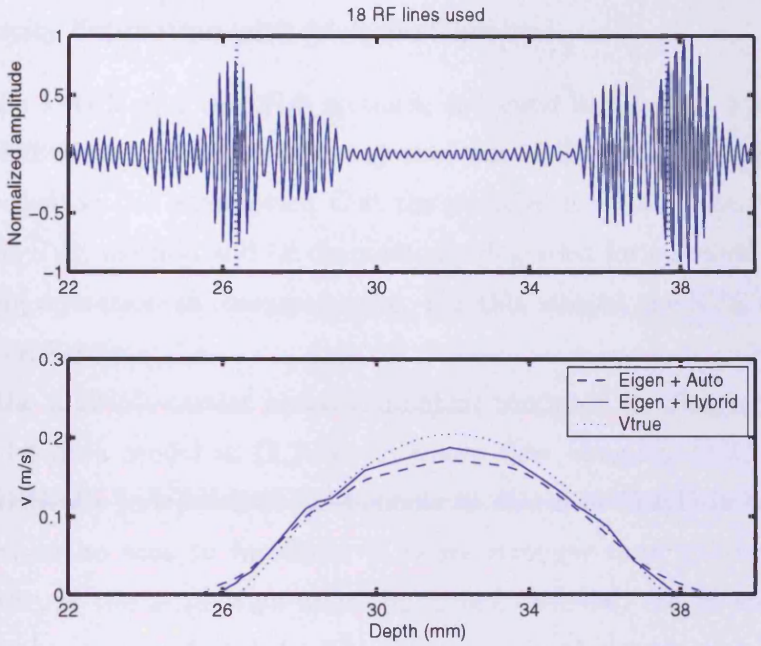

Figure 6.3. The estimated velocity profile using RF data from simulated carotid artery.

SVD-based eigenvector regression filter is used (termed *Eigen* in the figure). The lower plot in the figure illustrates the estimated velocity profile crossing the whole vessel using the autocorrelation method and the proposed hybrid estimator, respectively. As seen from the figure, both the autocorrelation method and the hybrid estimator accurately estimate the velocities close to the vessel walls. However, close to the vessel center, the hybrid estimator clearly outperforms the autocorrelation method. It is again worth noting that the center of the profile is not accurately estimated due to the fixed filter order employed therein. As already mentioned, the filter order should typically be allowed to vary over depth.

6.2 Blood Velocity Estimation with Multiple Carriers

In this section, the DAVE and the NLS methods proposed in Chapter 3 are extended for blood velocity estimation. It is worth noting that the SVE method proposed in Section 3.2.2 is derived based on the assumption that the additive noise is white. As a result, the performance of the SVE method will be dramatically degraded for coloured noise caused by the clutter filtering operation as discussed next. For this reason, the SVE method will not be further discussed herein.

Recall that the multiple-carrier based estimators proposed in Chapter 3 are based on the noisy sinusoidal data model in (3.2.1). In colour flow imaging, (3.2.1) is assumed to contain three statistically independent components as shown in (5.1.1) in which the clutter component is seen to be tens to hundreds of times stronger than the blood signal, and will completely corrupt the estimation unless cancelled [Jen96a]. To do so, one can apply a clutter filter to the measured signal. This filter can be designed in various ways, and is in itself an interesting topic of research; typically, a low order finite impulse response (FIR), infinite impulse response (IIR), or a subspace-based projection filter can be employed as discussed earlier. Such filters will strongly affect the assumed sinusoidal data model in (3.2.1). Recalling (3.2.1), let

$$z(t) = \mathbf{h}_P^H \mathbf{y}_P = \sum_{k=1}^{d} \gamma_k(v)\beta_k e^{i\omega_k(v)t} + \tilde{w}(t), \tag{6.2.1}$$

where $\mathbf{h}_P$ is a Pth order FIR filter, and

$$\mathbf{y}_P(t) \triangleq \begin{bmatrix} y(t) & \dots & y(t-P+1) \end{bmatrix}^T. \tag{6.2.2}$$

Further, $\gamma_k(v)$ is a velocity dependent function originating from the filtering and $\tilde{w}(t)$ is the coloured version of the additive noise $w(t)$ in (3.2.1) due to the clutter filtering introduced in (6.2.1). Very commonly, the clutter filter used is a simple difference filter [Jen96b], i.e.,

$$\mathbf{h}_P = \begin{bmatrix} 1 & -1 \end{bmatrix}^T, \tag{6.2.3}$$

yielding $\gamma_k(v) = e^{i\omega_k(v)} - 1$. As the data model in (3.2.1) is now changed as compared to (6.2.1), due to the filtering operation, the proposed methods in Chapter 4 need to be modified accordingly.

6.2.1 The Modified Data Adaptive Velocity Estimator

Similar to the DAVE derivation in Section 3.2.3, the modified data adaptive velocity estimator (M-DAVE) can be derived as follows. Let

$$\begin{aligned}\mathbf{z}_L(t) &\triangleq \left[\begin{array}{ccc} z(t) & \ldots & z(t+L-1) \end{array}\right]^T \\ &= \mathbf{A}_L(v)\tilde{\mathbf{\Phi}}_v(t)\boldsymbol{\beta} + \tilde{\mathbf{w}}_L(t), \end{aligned} \tag{6.2.4}$$

for $t = 0, \ldots, M = N - (P-1) - (L-1)$, $\tilde{\mathbf{w}}_L(t)$ is defined from $\tilde{w}(t)$ similar to $\mathbf{z}_L(t)$, and

$$\tilde{\mathbf{\Phi}}_v(t) = \boldsymbol{\gamma}(v)\mathbf{\Phi}_v(t) \tag{6.2.5}$$

$$\boldsymbol{\gamma}(v) = \left[\begin{array}{ccc} \gamma_1(v) & & \mathbf{0} \\ & \ddots & \\ \mathbf{0} & & \gamma_d(v) \end{array}\right] \tag{6.2.6}$$

with other notations defined in Section 3.2.2. Then, design a set of L-tap data adaptive FIR filters, $\mathbf{h}_k(v)$, for $k = 1, \ldots, d$, each centered at a given velocity v designed on the basis of solving the following constrained optimization

$$\min_{\mathbf{h}_k(v)} \mathbf{h}_k^H(v)\mathbf{R}_z\mathbf{h}_k(v) \quad \text{subject to} \quad \mathbf{h}_k^H(v)\mathbf{A}_L(v) = \mathbf{u}_k^T \quad \text{for} \quad k = 1, \ldots, d \tag{6.2.7}$$

where

$$\mathbf{R}_z = E\left\{\mathbf{z}_L(t)\mathbf{z}_L(t)^H\right\} \tag{6.2.8}$$

which can be estimated as for $\hat{\mathbf{R}}_y$ in (3.2.13). As derived in Section 3.2.3, the filter minimizing (6.2.7), is obtained as (see, e.g., [SM05])

$$\mathbf{h}_k^H(v) = \mathbf{u}_k^T \left[\mathbf{A}_L^H(v)\mathbf{R}_z^{-1}\mathbf{A}_L(v)\right]^{-1}\mathbf{A}_L^H(v)\mathbf{R}_z^{-1}, \tag{6.2.9}$$

suggesting that the velocity spectrum is formed as

$$\begin{aligned}\phi_z(v) &\triangleq \sum_{k=1}^{d} \mathbf{h}_k^H(v)\hat{\mathbf{R}}_z\mathbf{h}_k(v) \\ &= \sum_{k=1}^{d} \mathbf{u}_k^T \left[\mathbf{A}_L^H(v)\hat{\mathbf{R}}_z^{-1}\mathbf{A}_L(v)\right]^{-1}\mathbf{u}_k, \end{aligned} \tag{6.2.10}$$

where $\hat{\mathbf{R}}_z$ has also been used for the filter design in (6.2.9), which will thus mainly contain the d sinusoidal components resulting from the velocity v. Thus, by evaluating $\phi_z(v)$ for a range of velocities of interest, $v \in [v_{min}, v_{max}]$, the velocity of the reflecting scatterer can be estimated as the velocity maximizing $\phi_z(v)$. Similar to the DAVE algorithm, it is worth noting that the matrix $\mathbf{A}_L^H(v)\hat{\mathbf{R}}_z^{-1}\mathbf{A}_L(v)$ may be poorly conditioned for small v due to the resulting closely spaced frequency components. To alleviate this problem, one can employ a low rank approximation technique as performed in Appendix 3.D.

6.2.2 The Modified Nonlinear Least Squares Estimator

The modified nonlinear least squares (M-NLS) estimator, extending the NLS estimator derived in Section 3.2.4, is derived in this section. Note that (6.2.1) can be written as

$$\mathbf{z}_{N-(P-1)}(0) = \tilde{\mathbf{A}}_{N-(P-1)}(v)\boldsymbol{\beta} + \tilde{\mathbf{w}}_{N-(P-1)}(0)\ , \tag{6.2.11}$$

where

$$\mathbf{z}_{N-(P-1)}(0) = \left[\begin{array}{ccc} z(0) & \cdots & z(N-(P-1)-1)\end{array}\right]^T, \tag{6.2.12}$$

$$\tilde{\mathbf{A}}_{N-(P-1)}(v) = \mathbf{A}_{N-(P-1)}(v)\tilde{\boldsymbol{\Phi}}_v(0)\ , \tag{6.2.13}$$

with $\tilde{\mathbf{w}}_{N-(P-1)}(0)$ defined similar to $\mathbf{z}_{N-(P-1)}(0)$. Therefore, the M-NLS estimate of v can be obtained as

$$\hat{v} = \arg\min_{\boldsymbol{\beta},v} \| \ \mathbf{z}_{N-(P-1)}(0) - \tilde{\mathbf{A}}_{N-(P-1)}\boldsymbol{\beta} \ \|_F^2 \tag{6.2.14}$$

where the least-squares estimate of $\boldsymbol{\beta}$ can be found as [SM05]

$$\hat{\boldsymbol{\beta}} = \left[\tilde{\mathbf{A}}^H_{N-(P-1)}(v)\tilde{\mathbf{A}}_{N-(P-1)}(v) \right]^{-1} \tilde{\mathbf{A}}_{N-(P-1)}(v)\mathbf{z}_{N-(P-1)}(0) \ . \tag{6.2.15}$$

Inserting (6.2.15) into (6.2.14) yields the maximization

$$\hat{v} = \arg\max_v \| \ \boldsymbol{\Pi}_{\tilde{\mathbf{A}}} \mathbf{z}_{N-(P-1)}(0) \ \|_2^2 \tag{6.2.16}$$

where

$$\boldsymbol{\Pi}_{\tilde{\mathbf{A}}} \triangleq \tilde{\mathbf{A}}^H_{N-(P-1)}(v) \left[\tilde{\mathbf{A}}_{N-(P-1)}(v)\tilde{\mathbf{A}}_{N-(P-1)}(v) \right]^{-1} \tilde{\mathbf{A}}_{N-(P-1)}(v) \ . \tag{6.2.17}$$

Parallelling the low-rank discussion above, one can use a low-rank approximation to alleviate a possibly poor conditioning of the $\tilde{\mathbf{A}}_{N-(P-1)}(v)\tilde{\mathbf{A}}_{N-(P-1)}(v)$ matrix for small v; again, this can be done using the technique in Appendix 3.D.

6.2.3 Simulation Results

In this section, the M-DAVE and M-NLS methods will be examined with two different scenarios, *fibre flow* and *parabolic flow*. For simplicity, a second order FIR clutter filter is employed herein.

Fibre Flow

To examine the performance of the M-DAVE and M-NLS methods, initially, single fibre-like flow is simulated, which comprises 1000 blood particles lying along the vessel center and moving towards the transducer along the beam direction (pure axial velocity). The parameters for simulating RF data are listed in Appendix 6.B.

Figure 6.4 shows the velocity spectra using M-DAVE with RF data acquired from the transmission focus which is 35 mm away from the transducer surface as illustrated in Appendix 6.B. The underlying velocity of the fibre flow varies from $0.5 \times v_{Nyq}$ to $2 \times v_{Nyq}$ as

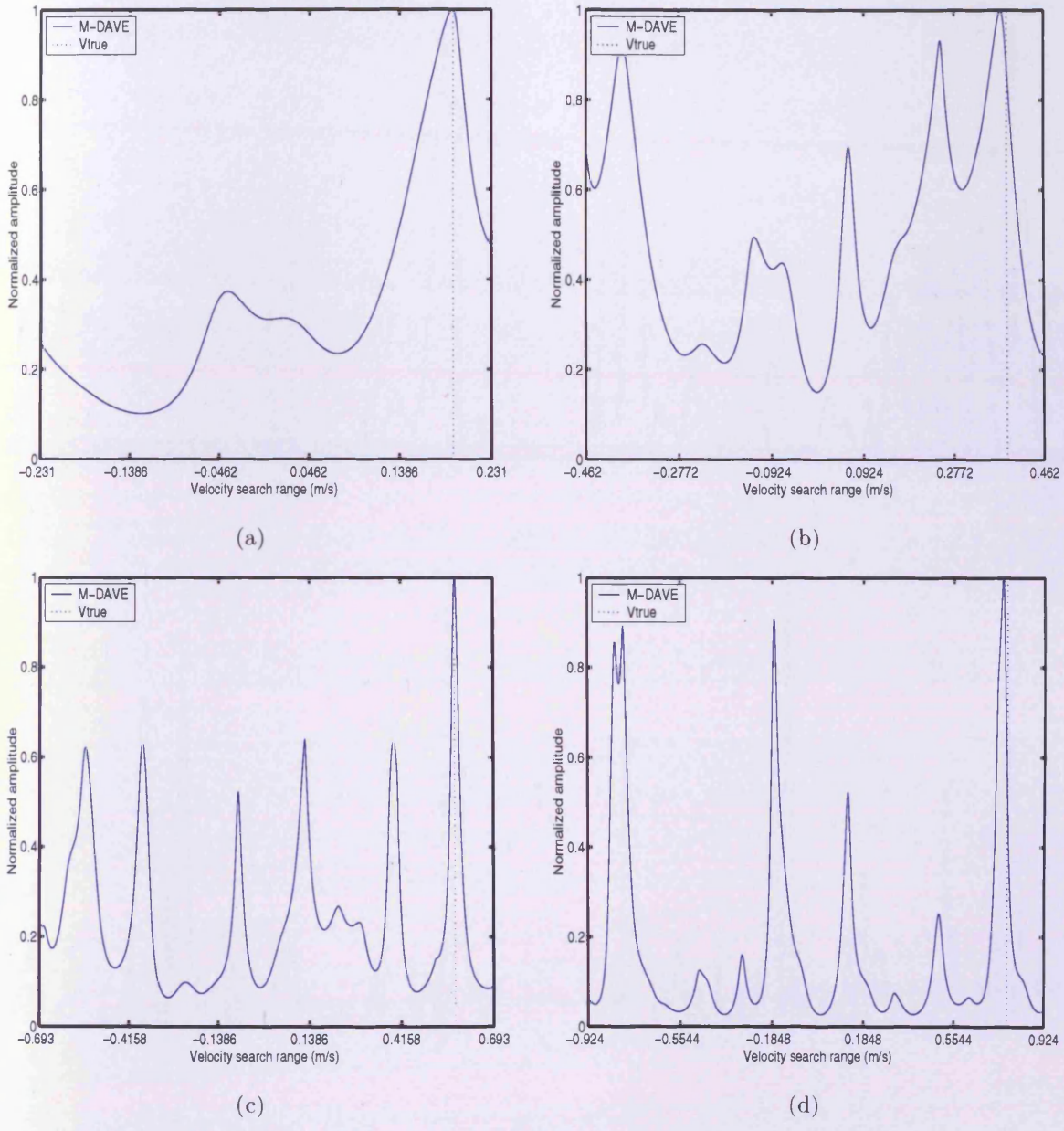

Figure 6.4. The velocity spectra using the M-DAVE method with RF data obtained from simulated fibre flow with $SNR = 10$ dB, for (a) $v = 0.5 \times v_{Nyq}$; (b) $v = 1 \times v_{Nyq}$; (c) $v = 1.5 \times v_{Nyq}$; (d) $v = 2 \times v_{Nyq}$.

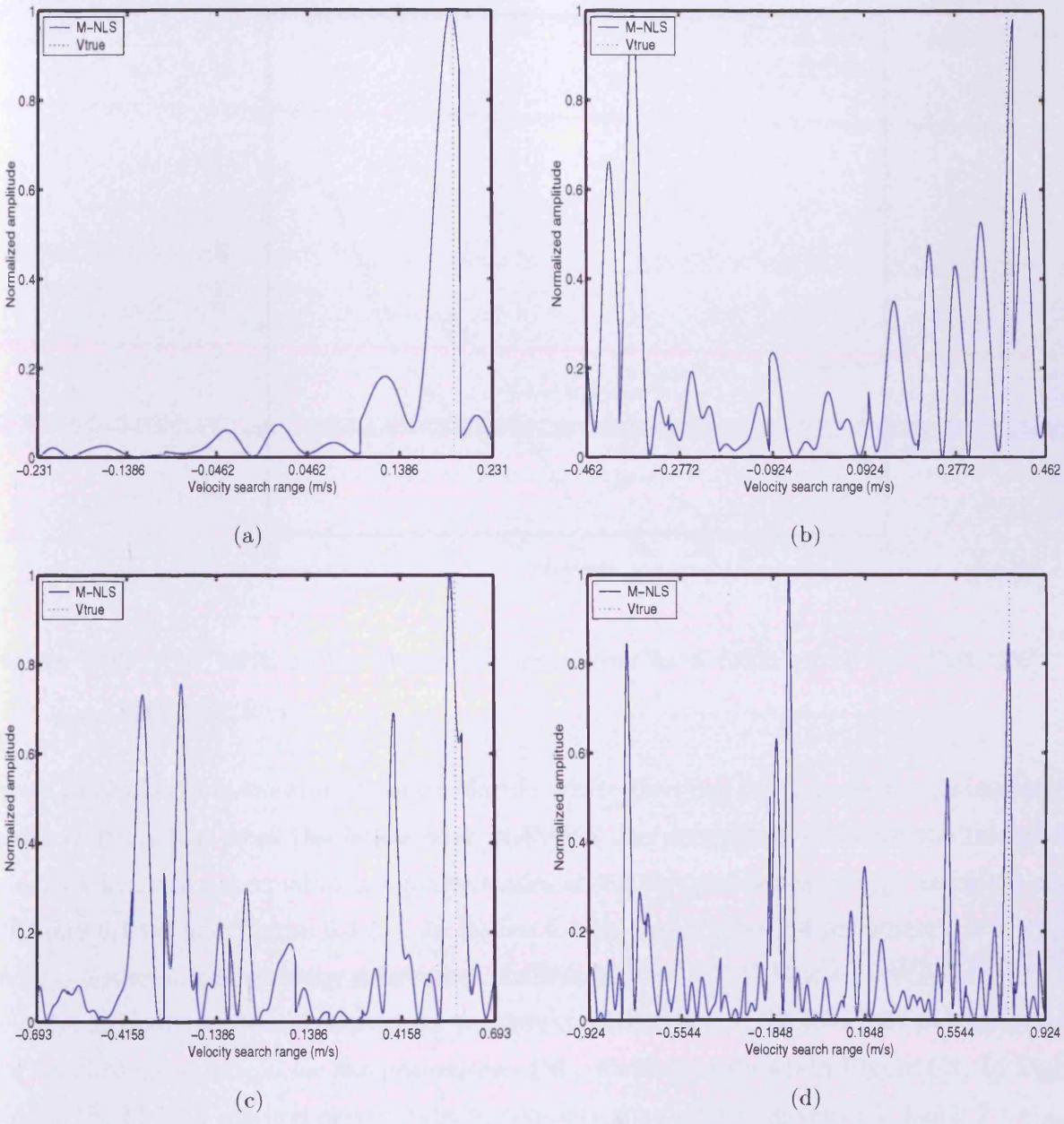

Figure 6.5. The velocity spectra using the M-NLS method with RF data obtained from simulated fibre flow with $SNR = 10$ dB, for (a) $v = 0.5 \times v_{Nyq}$; (b) $v = 1 \times v_{Nyq}$; (c) $v = 1.5 \times v_{Nyq}$; (d) $v = 2 \times v_{Nyq}$.

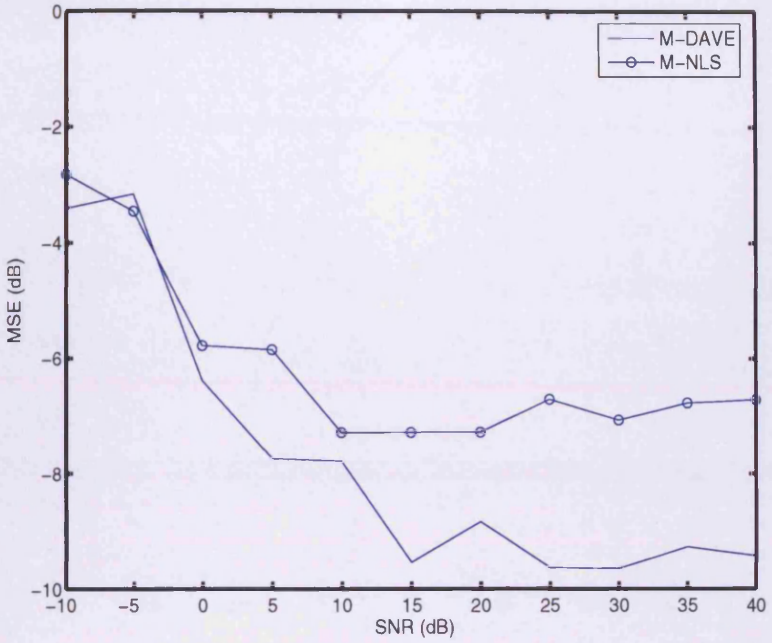

Figure 6.6. The MSE of the examined estimators as a function of the SNR, for $v = 1.5 \times v_{Nyq}$, with fibre flow.

shown clockwise from the top left in the figure, where the dash line represents the underlying velocity. It is clear from the figure that M-DAVE can accurately estimate the underlying velocity when it is not equal to integer multiples of the Nyquist velocity, v_{Nyq}, as for the cases in Figure 6.4 (a) and Figure 6.4 (c). In Figure 6.4 (b) and Figure 6.4 (d) where $v = 1 \times v_{Nyq}$ and $v = 2 \times v_{Nyq}$, respectively, it becomes challenging for M-DAVE to estimate correctly the underlying velocity. These results are consistent with those in Section 3.3. Similar results and conclusions also hold for the evaluation of the M-NLS as shown in Figure 6.5. In Figure 6.5 (d), the M-NLS method clearly fails to estimate the underlying velocity, being $2 \times v_{Nyq}$.

To further examine the performance of M-DAVE and M-NLS statistically, the MSE of

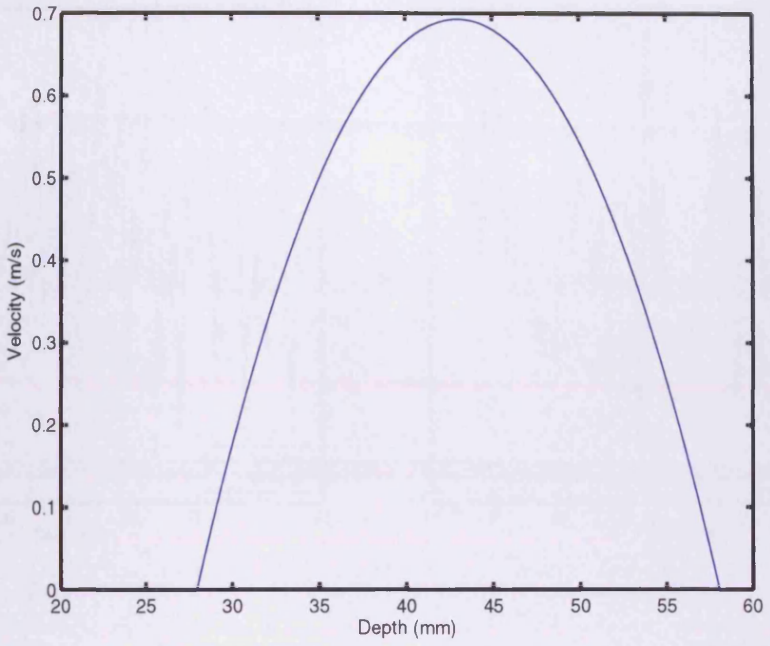

Figure 6.7. The parabolic velocity profile.

the estimates as a function of the SNR from the transmission focus point are calculated and shown in Figure 6.6, where the underlying velocity $v = 1.5 \times v_{Nyq}$. As is clear from the figure, both the methods show similar performance when the SNR is less than 0 dB. As SNR increases, the M-DAVE method is seen to outperform the M-NLS approach.

Parabolic Flow

Consider a realistic case where pure blood flow (consisting of 3×10^5 scatters) with parabolic profile as defined in (6.1.1) is simulated with maximum velocity $v_0 = 1.8 \times v_{Nyq}$ at the vessel center. The corresponding parameters are given in Appendix 6.B. The true axial velocity profile is depicted in Figure 6.7. As the flow is purely blood flow without taking into account

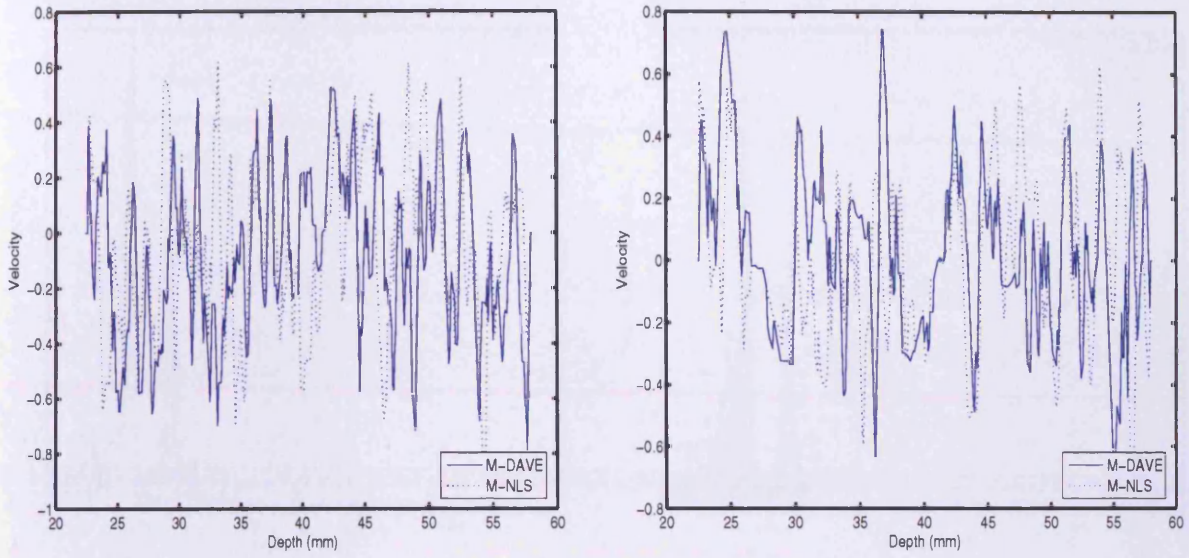

(a) (b)

Figure 6.8. The estimated velocity profile of parabolic flow, with (a) $SNR = 10$ dB; (b) $SNR = 30$ dB.

vessel walls and clutter effects, additive white Gaussian noise is added with different SNR defined based on the RF data from vessel centre position. Figure 6.8 shows the estimated velocity profile of parabolic flow with $SNR = 10$ dB and $SNR = 30$ dB, respectively. It is clear from the figure that the proposed methods actually failed to estimate the parabolic flow. To further investigate this, Figure 6.9 illustrates the power spectra of excitation (the sinusoidal signal transmitted by transducer) and one RF echo, for fibre flow and parabolic flow, respectively. It is clear from Figure 6.9 (a) that the transmitted power in the fibre flow is not seriously damped and the spectrum of the RF echo well matches the one obtained from the excitation. In the parabolic flow scenario, the transmitted power is damped seriously and more side lobes exist as shown in Figure 6.9 (b), implying that there exists a mismatch between the RF echo and the sinusoidal data model in (3.2.1). This may well explain why

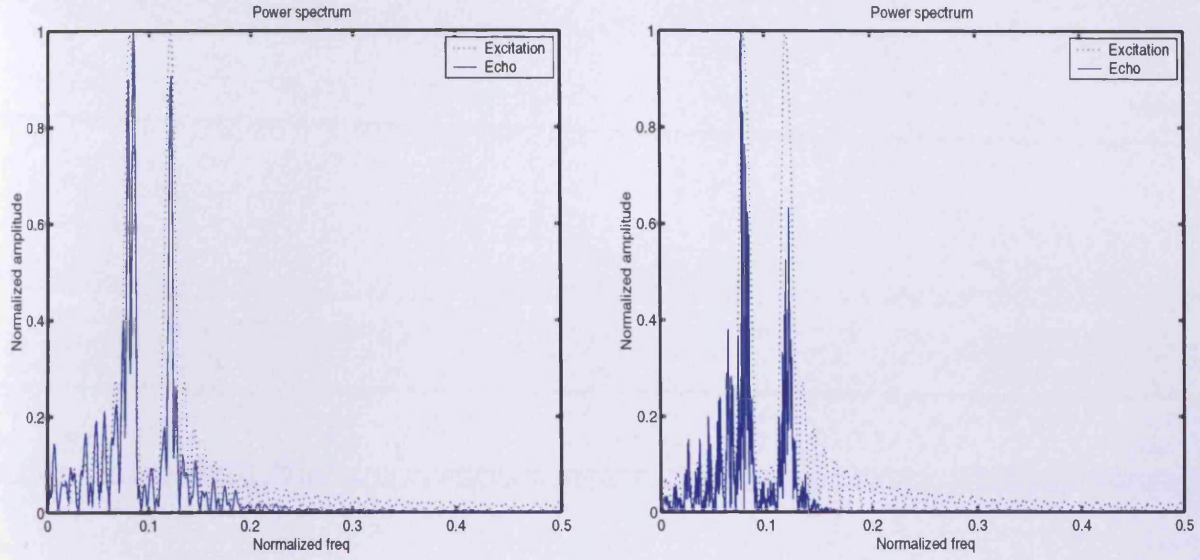

(a) (b)

Figure 6.9. The spectra of excitation and RF echo for (a) fibre flow; (b) parabolic flow.

the M-DAVE and M-NLS methods failed for the realistic parabolic flow. Further research will be needed on how to improve both the data model in (3.2.1) and the simulation model used for RF generation. This is a topic of ongoing research.

6.3 Conclusion

This chapter discusses the blood velocity estimation using the proposed estimators in Part I of this thesis. Realistic RF data generated with the Field II toolbox are used. Section 6.1 examines the hybrid estimator proposed in Chapter 2. The MSE results obtained from examining with fibre flow RF data show that the hybrid estimator statistically outperforms the conventional autocorrelation estimator. To further confirm this, both the methods are examined with realistic carotid flow and the hybrid estimator again shows better performance

than the autocorrelation estimator. It is worth noting that, as discussed in Chapter 2, the performance of the hybrid estimator will be worse if there exists serious power damping or frequency spread in RF data.

In Section 6.2, the DAVE and the NLS methods proposed in Chapter 3 are modified to take into account the applied FIR clutter filtering. The modified estimators are then examined using RF data obtained from simulated fibre flow as well as parabolic flow. The results indicate that the M-DAVE and M-NLS methods work well with fibre flow, but fail with parabolic flow. The most likely reason for this failure is due to the mismatch between the multiple-carrier based sinusoidal data model in (3.2.1) and the actual RF data obtained from parabolic flow. The failure of the estimators also implies that the estimators are very sensitive to the data examined and will perform worse if there is a mismatch between the examined data and the ideal data model from which the estimators are derived.

Appendix

6.A Parameters for Simulating Blood Flow with Single Carrier

Centre (single carrier) frequency, f_c	10 MHz	Transducer type	Phased array
Sampling frequency, f_s	100 MHz	Transducer elements	64
Pulse repetition frequency, f_{prf}	10^4 Hz	Transducer element pitch	0.077 mm
Velocity in fibre, v	$0.5 \times v_{Nyq}$	Transducer element kerf	0.00385 mm
Peak velocity in parabolic flow, v_0	$0.8 \times v_{Nyq}$	Transducer element width	0.732 mm
Sound speed, c	1540 m/s	Transducer element height	5 mm
RF lines per estimate, N	18	Focus in transmission	35 mm
Pulse oscillation (M)	10	Focus in reception	35 mm
DOA in fibre	0°	Elevation focus	25 mm
DOA in parabolic flow case	45°	Apodization in transmission	Hanning
Bandwidth	0.6	Apodization in reception	Hanning
Center of vessel	35 mm	Vessel radius	5 mm

6.B Parameters for Simulating Blood Flow with Multiple Carriers

Multiple carriers	[8.1, 11.97] MHz	Transducer type	Phased array
Sampling frequency, f_s	100 MHz	Transducer elements	64
Pulse repetition frequency, f_{prf}	10^4 Hz	Transducer element pitch	0.077 mm
Sound speed, c	1540 m/s	Transducer element kerf	0.00385 mm
RF lines per estimate, N	20	Transducer element width	0.732 mm
Pulse oscillation (M)	10	Transducer element height	5 mm
DOA in fibre	0°	Focus in transmission	35 mm
DOA in parabolic flow case	45°	Focus in reception	35 mm
Bandwidth	0.6	Elevation focus	25 mm
Center of vessel	35 mm	Apodization in transmission	Hanning
Vessel radius	5 mm	Apodization in reception	Hanning

Chapter 7

CONCLUSIONS AND SUGGESTIONS FOR FUTURE RESEARCH

In this chapter, the conclusions are drawn for the work involved in this thesis and possible topics are suggested for future research.

7.1 Conclusions

In this work, a variety of problems are examined:

i. The problem of estimating the frequency of a sinusoid in noise is stated in Chapter 2. A hybrid phase-based single frequency estimator with low computational complexity is proposed, combining previously proposed SNR threshold reduction approaches with a recent outlier removal scheme. The proposed estimator achieves a lower mean square error than other available techniques, lowering the SNR threshold at which the CRLB is closely followed. Furthermore, in contrast to many other techniques, the performance of the hybrid estimator is found to be essentially independent of the true frequency. Related issues such as power damping and frequency spread are also briefly discussed;

ii. Doppler shift estimation or the resulting velocity estimation of a moving target is an important topic in a wide variety of fields. In Chapter 3, three novel velocity estimators

using multiple frequency carriers have been developed. Evaluation using synthetic data indicates that these new estimators have the capability to mitigate the poor high velocity performance of conventional correlation based techniques and thereby provide usable performance beyond the conventional Nyquist velocity limit. Furthermore, the CRLB for the velocity estimation is derived to evaluate the performance of the proposed methods.

iii. To enable high quality ultrasound color flow images, efficient attenuation of the clutter signal is one of the critical factors. The analysis of existing filters implies that the recent introduction of the ERF/PCA and possibly the ICA methods seem very promising for this purpose. An efficient approach to recursively form the clutter filters using a recent recursive subspace tracking technique is introduced in Chapter 5. The proposed method is successfully examined with realistic carotid flow which is simulated with the Field II toolbox [Jen96b].

iv. Commonly, narrow-band PW systems estimate the blood velocity using an autocorrelation-based estimator. In Chapter 6, the hybrid frequency estimator proposed in Chapter 2 is examined with realistic RF data which shows the achievable performance gain of this method as compared to the traditional approach.

v. As the multiple-carrier based velocity estimators proposed in Chapter 3 are motivated in association with the application of blood velocity estimation, in Chapter 6 the DAVE and the NLS estimators are modified (accordingly termed M-DAVE and M-NLS, respectively) due to the introduced clutter filtering and applied to realistic RF data for blood velocity estimation. The M-DAVE and M-NLS methods were found to work well with fibre flow, but fail with parabolic flow. The most likely reason for this failure is due to the mismatch between the multiple-carrier based sinusoidal data model and the actual RF data obtained from parabolic flow.

All of the above conclusions illustrate the usefulness of parameter estimation in solving practical problems arising in a variety of applications. It also exposes the problems existing in current research. Therefore, it is believed that the following suggestions provide a pathway for future research.

7.2 Suggestions for Future Research

Based on the work and analysis in this thesis, four possible topics for future research projects are proposed.

Frequency Estimation of a General Sinusoidal Data Model

The problem of a single tone estimation has been well studied in this thesis. However, this study is confined to the pure sinusoidal data model only, which somewhat restricts the generality of this hybrid estimator. As a result, it is natural to extend the hybrid estimator to be valid for a more general sinusoidal data model allowing power damping and frequency spread.

Estimation of 2-Dimensional Frequencies

In Chapter 2, the hybrid estimator has been shown to outperform the examined single tone estimators, exhibiting lower MSE and SNR threshold as compared to other estimators. It is believed that there is more to be done in this topic. One thing to examine would be to extend the single tone estimator to the estimation of 2-dimensional frequencies.

Order Estimation of Subspace-based Clutter Filters

In this thesis, the clutter rejection problem is studied and an efficient implementation of clutter subspace tracking technique for the subspace-based clutter filters is successfully in-

troduced. However, the order estimation problem involved in the clutter filters has not been investigated yet in this work. As pointed out in the previous chapters, further research is needed on how the filter order should be selected appropriately. Thus, to better implement the introduced efficient subspace tracking technique in clutter rejection, a critical problem is the corresponding order estimation.

Improving the Multiple-carrier Based Estimators

The failure of the M-DAVE and the M-NLS estimators with realistic parabolic flow investigated in Chapter 6 implies that the estimators are very sensitive to the data examined and their performance will degrade if there is a mismatch between the examined data and the ideal data model from which the estimators are derived. Further research will be needed on how to improve the data model in (3.2.1) and the resulting estimators so that they can be successfully implemented in practice.

In addition, it is worth noting that the proposed multiple-carrier based estimators in Chapter 3 have high computational complexity. As a result, it would be interesting to look into how these methods can be implemented with lower computational load.

BIBLIOGRAPHY

[AP03] S. K. Alam and K. J. Parker. Implementation Issues in Ultrasonic Flow Imaging. *Ultrasound in Med. and Biol.*, 29(4):517–528, 2003.

[BFMT93] L. N. Bohs, B. H. Friemel, B. A. Mcdermott, and G. E. Trahey. A Real Time System for Quantifying and Displaying Two-dimensional Velocities Using Ultrasound. *Ultrasound in Med. and Biol.*, 19(9):751–61, Sept. 1993.

[BHR95] P. J. Brands, A. P. G. Hoeks, and R. S. Reneman. The Effect of Echo Suppression on the Mean Velocity Estimation Range of the RF Cross-correlation Model. *Ultrasound in Med. and Biol.*, 21(7):945–959, 1995.

[BP86] O. Bonnefous and P. Pesque. Time Domain Formulation of Pulse-Doppler Ultrasound and Blood Velocity Estimation by Cross Correlation. *Ultrason Imaging*, 8(2):73–85, April 1986.

[BRD04] R. Badeau, G. Richard, and B. David. Sliding Window Adaptive SVD Algorithms. *IEEE Trans. Signal Processing*, 52(1):1–10, Jan. 2004.

[BT97] S. Bjaerum and H. Torp. Optimal Adaptive Clutter Filtering in Color Flow Imaging. In *Proc. IEEE Ultrason. Symp.*, volume 2, 1997.

[BTK02] S. Bjaerum, H. Torp, and K. Kristoffersen. Clutter Filters Adapted to Tissue Motion in Ultrasound Color Flow Imaging. *IEEE Trans. Ultrason., Ferroelec., Freq. Contr.*, 49(6):693–704, June 2002.

[BW02] T. Brown and M. M. Wang. An Iterative Algorithm for Single-Frequency Estimation. *IEEE Trans. Signal Processing*, 50(11):2671–2682, Nov. 2002.

[Car98] J. F. Cardoso. Blind Signal Separation: Statistical Principles. *Proceeding of the IEEE*, 9(10):2009–2025, Oct. 1998.

[CG90] P. Comon and G. H. Golub. Tracking a Few Extreme Singular Values and Vectors in Signal Processing. *IEEE Proc.*, 78(8):1327–1343, Aug. 1990.

[Chi97] D. G. Childers. *Probability and Random Processes.* McGraw-Hill, New York, 1997.

[CKQ94] V. Clarkson, P. J. Kootsookos, and B. G. Quinn. Analysis of the Variance Threshold of Kay's Weighted Linear Predictor Frequency Estimator. *IEEE Trans. Signal Processing*, 42(9):2370–2379, Sept. 1994.

[Cla92] V. Clarkson. Efficient Single Frequency Estimators. In *The International Symposium on Signal Processing and its Applications (ISSPA92)*, pages 327–330, Gold Coast, Australia, 1992.

[DGS92] B. Dousse, B. Grossniklaus, and C. Scheuble. Two Years Experience in Measuring Velocities Beyond the Nyquist Limit with Color Flow Mapper. *Eurodop*, 1992.

[Edd93] B. Edde. *Radar: Principles, Technology, Applications.* Prentice-Hall, Upper Saddle River, N.J., 1993.

[EFPF97] A. I. El-Fallah, M. B. Plantec, and K. W. Ferrara. Ultrasonic Mapping of Breast Tissue Motion and the Implications for Velocity Estimation. *Ultrasound in Med. and Biol.*, 23(7):1047–1057, July 1997.

[EM00] D. H. Evans and W. N. McDicken. *Doppler Ultrasound-Physics, Instrumentation and Signal Processing, 2nd Edition.* Wiley, 2000.

[Eva93] D. H. Evans. Techniques for Color-flow Imaging. *Advances in Ultrasound Techniques and Instrumentation* , 28:452–456, 1993.

[FJ99] M. L. Fowler and J. A. Johnson. Extending the Threshold and Frequency Range for Phase-Based Frequency Estimation. *IEEE Trans. Signal Processing*, 2857-2863(10):212–214, Oct. 1999.

[Fow02] M. L. Fowler. Phase-Based Frequency Estimation: A Review. *Digital Signal Processing*, 12(2):590–615, Oct. 2002.

[GNT03] C. M. Gallippi, K. R. Nightingale, and G. E. Trahey. BSS-based Filtering of Pphysiological and APFI-induced Tissue and Blood Motion. *Ultrasound in Med. and Biol.*, 29(11):1583–1592, Nov. 2003.

[GT02] C. M. Gallippi and G. E. Trahey. Adaptive Clutter Filtering via Blind Source Separation for Two-Dimensional Ultrasonic Blood Velocity Measurement. *Ultrasonic Imaging*, 24(4):193–214, Oct. 2002.

[GV96] G. H. Golub and C. F. Van Loan. *Matrix Computations.* The Johns Hopkins University press, 1996.

[GW02] R. C. Gonzalez and R. E. Woods. *Digital Image Processing, 2nd Edition.* Addison-Wesley, 2002.

[Hö95] P. Händel. On the Performance of the Weighted Linear Predictor Frequency Estimator. *IEEE Trans. Signal Processing*, 43(12):3070–3071, Dec. 1995.

[HHR91] A. P. G. Hoeks, M. Hennerici, and R. S. Reneman. Spectral composition of Doppler signals. *Ultrasound in Med. and Biol.*, 17(8):751–760, 1991.

[Hil86] C. R. Hill. *Physical Principles of Medical Ultrasonics.* Ellis Horwood series in applied physics: Ellis Horwood Limited, 1986.

[HvdVD+91] A. P. G. Hoeks, J. J. W. van de Vorst, A. Dabekaussen, P. J. Brands, and R. S. Reneman. An Efficient Algorithm to Remove Low Frequency Doppler Signal in Digital Doppler System. *Ultrason Imaging*, 13(3):135–145, 1991.

[Jen93a] J. A. Jensen. Range/Velocity Limitations for Time-domain Blood Velocity Estimation. *Ultrasound in Med. and Biol.*, 19:741–749, 1993.

[Jen93b] J. A. Jensen. Stationary Echo Canceling in Velocity Estimation by Time-domain Cross-correlation. *IEEE Trans. Medical Imaging*, 12(3):471–477, Dec. 1993.

[Jen96a] J. A. Jensen. *Estimation of Blood Velocities Using Ultrasound.* Cambridge University Press, New York, 1996.

[Jen96b] J. A. Jensen. Field: A Program for Simulating Ultrasound Systems. In *Medical and Biological Engineering and Computing*, volume 34, pages 351–353, 1996.

[Jen01] J. A. Jensen. *Users' Guide for the Field II Program.* Technical University of Denmark, Aug. 2001.

[Kad02] Y. M. Kadah. Spatio-temporal Analysis of Color Doppler Information Using Independent Component Analysis. In *Proceedings of SPIE: Medical Imaging 2002: Ultrasonic Imaging and Signal Processing*, volume 4687, pages 227–234, 2002.

[Kay88] S. M. Kay. *Modern Spectral Estimation: Theory and Application.* Prentice-Hall, Englewood Cliffs, N.J., 1988.

[Kay89] S. Kay. A Fast and Accurate Single Frequency Estimator. *IEEE Trans. Acoustics Speech Signal Processing*, 37(12):1987–1990, Dec. 1989.

[Kay93] S. M. Kay. *Fundamentals of Statistical Signal Processing, Volume I: Estimation Theory.* Prentice-Hall, Englewood Cliffs, N.J., 1993.

[KF02] D. E. Kruse and K. W. Ferrara. A New High Resolution Color Flow System Using an Eigendecomposition-based Adaptive Filter for Clutter Rejection. *IEEE Trans. Ultrason., Ferroelec., Freq. Contr.*, 49(12):1739–1754, 2002.

[KHTI03] C. Kargel, G. Höbenreich, B. Trummer, and M. F. Insana. Adaptive Clutter Rejection Filtering in Ultrasonic Strain-Flow Imaging. *IEEE Trans. Ultrason., Ferroelec., Freq. Contr.*, 50(7):824–835, July 2003.

[KK01] N. Kannan and D. Kundu. Estimating Parameters in the Damped Exponential Model. *Signal Processing*, 81(11):2343–2351, Nov. 2001.

[KL95] A. P. Kadi and T. Loupas. On the Performance of Regression and Step Initialized IIR Clutter Filters for Color Doppler Systems in Diagnostical Medical Ultrasound. *IEEE Trans. Ultrason., Ferroelec., Freq. Contr.*, 42(3):927–937, 1995.

[Kle05] J. D. Klein. Fast Statistically Efficient Algorithms for Single Frequency Estimation . In *Proc. ICASSP 05*, pages 389–392, Philadelphia, USA, 2005.

[KNC96] D. Kim, M. J. Narasimha, and D. C. Cox. An Improved Single Frequency Estimator. *IEEE Signal Processing Letters*, 3(7):212–214, July 1996.

[KNKO85] C. Kasai, K. Namekawa, A. Koyano, and R. Omoto. Real-time Two-dimensional Blood Flow Imaging Using an Autocorrelation Technique. *IEEE Trans. Sonic Ultrason*, 32:458–464, May 1985.

[KP95] W. B. Kleijn and K. K. Paliwal, editors. *Speech Coding and Synthesis.* Elsevier Science, 1995.

[LBH97] L. A. F. Ledoux, P. J. Brands, and A. P. G. Hoeks. Reduction of the Clutter Component in Doppler Ultrasound Signals Based on Singular Value Decomposition: a Simulation Study. *Ultrasonic Imaging*, 19:1–18, Sept. 1997.

[LM89] S. W. Lang and B. R. Musicus. Frequency Estimation from Phase Differences. In *Proc. ICASSP 89*, pages 2140–2143, Glasgow, Scotland, 1989.

[LRP73] G. W. Lank, I. S. Reed, and G. E. Pollon. A Semicoherent Detection and Doppler Estimation Statistic. *IEEE Trans. Aerospace and Electronic Systems*, 9(2):151–165, March 1973.

[LSE+86] N. P. Luckman, R. Skidmore, J. M. Evans, D. Jenkins, and P. N. T. Wells. *Physics in Medical Ultrasound II.* York, UK: The Institute of Physical Sciences in Medicine, 1986.

[LTCF96] G. R. Lockwood, D. H. Turnbull, D. A. Christopher, and F. S. Foster. Applications of high-frequency ultrasound imaging. *IEEE Eng. Med.Biol. Mag.*, 15(6):60–71, Nov.-Dec. 1996.

[LW92] B. C. Lovell and R. C. Williamson. The Statistical Performance of Some Instantaneous Frequency Estimators. *IEEE Trans. Signal Processing*, 40(7):1708–1723, July 1992.

[Mac04] M. D. Macleod. An Improved Fast Estimator of the Frequency of a Single Complex Tone. In *Sixth IMA International Conference on Mathematics in Signal Processing*, pages 155–158, Cirencester, UK, 2004.

[Mai78] I. G. Main. *Vibrations and Waves in Physics.* Cambridge university press, 1978.

[Mar87] S. L. Marple, Jr. *Digital Spectral Analysis with Applications.* Prentice-Hall, Englewood Cliffs, N.J., 1987.

[Mar99] S. L. Marple. Computing the Discrete-time "Analytic" Signal via FFT. *IEEE Trans. Signal Processing*, 47(9):2600–2603, September 1999.

[MH98] Y. Miao and Y. Hua. Fast Subspace Tracking and Neural Network Learning by a Novel Information Criterion. *IEEE Trans. Signal Processing*, 46(7):1967–1979, July 1998.

[Nik01] S. I. Nikolov. *Synthetic Aperture Tissue and Flow Ultrasound Imaging.* PhD thesis, Technical University of Denmark, Aug. 2001.

[NRB+95] H. J. Nitzpon, J. C. Rajaonah, C. B. Burckhardt, B. Dousse, and J. J. Meister. A New Pulsed Wave Doppler Ultrasound System to Measure Blood Velocities Beyond the Nyquist Limit. *IEEE Trans. Ultrason., Ferroelec., Freq. Contr.*, 42(2):265–79, Mar. 1995.

[OSB99] A. V. Oppenheim, R. W. Schafer, and J. R. Buck. *Discrete-time Signal Processing, 2nd Edition.* Prentice Hall, 1999.

[PAB94] R. B. Peterson, L. E. Atlas, and K. W. Beach. A Comparison of IIR Initialization Techniques for Improved Color Doppler Wall Filter Performance. In *Proc. IEEE Ultrason. Symp.*, volume 3, 1994.

[Pro95] R. Prony. Essa: Experimentale et Analytique. *J. Ecole Polytechnique*, pages 24–76, 1795.

[Pro89] J. G. Proakis. *Digital Communications.* McGraw-Hill, Inc., 1989.

[QH01] B. G. Quinn and E. J. Hannan. *The Estimation and Tracking of Frequency.* Cambridge, NY : Cambridge University Press, 2001.

[Qui00] B. G. Quinn. On Kay's Frequency Estimator. *Journal of Time Series Analysis*, 21(6):707–712, Nov. 2000.

[RB74] D. C. Rife and R. R. Boorstyn. Single-Tone Parameter Estimation from Discrete-Time Observations. *IEEE Trans. Information Theory*, 20(5):591–598, Sept. 1974.

[Sch01] M. Schlaikjer. *Development and Characterization of Algorithms for Estimation of Blood Velocity with Ultrasound.* PhD thesis, Technical University of Denmark, Feb. 2001.

[SDM93] M. A. Shariati, J. H. Dripps, and W. N. McDickend. A Comparison of Colour Flow Imaging Algorithms. *Phys. Med. Biol.*, 38(11):1589–1600, Nov. 1993.

[SM05] P. Stoica and R. Moses. *Spectral Analysis of Signals.* Prentice Hall, Upper Saddle River, N.J., 2005.

[Sto93] P. Stoica. List of Reference on Spectral Line Analysis. *Signal Processing*, 31(3):329–340, April 1993.

[Sto02] J. V. Stone. Independent Component Analysis: an Introduction. *TRENDS in Cognitive Sciences*, 6(2):59–64, Feb. 2002.

[Str97] P. Strobach. Bi-Iteration SVD Subspace Tracking Algorithms. *IEEE Trans. Signal Processing*, 45(5):1222–1240, May 1997.

[TH94] L. Thomas and A. Hall. An Improved Wall Filter for Flow Imaging of Low Velocity Flow. In *Proc. IEEE Ultrason. Symp.*, volume 3, 1994.

[TMLI04] J. K. Tsou, J. J. Mai, F. A. Lupotti, and M. F. Insana. Simultaneous Narrow-band Ultrasonic Strain-Flow Imaging. In *SPIE: Medical Imaging 2004*, San Diego, USA, 2004.

[Tor89] P. Tortoli. A Tracking FFT Processor for Pulsed Doppler Analysis Beyond the Nyquist Limit. *IEEE Trans. Biomed., Eng.*, 36(2):265–79, Feb. 1989.

[Tor97] H. Torp. Clutter Rejection Filters in Color Flow Imaging: A Theoretical Approach. *IEEE Trans. Ultrason., Ferroelec., Freq. Contr.*, 44(2):417–424, March 1997.

[Tre85] S. A. Tretter. Estimating the Frequency of a Noisy Sinusoid by Linear Regression. *IEEE Trans. Information Theory*, 31(6):832–835, Nov. 1985.

[TWF+04] Q. Tao, Y. Wang, P. Fish, W. Wang, and J. Cardoso. The Wall Signal Removal in Doppler Ultrasound Systems Based on Recursive PCA. *Ultrasound in Med. and Biol.*, 30(3):369–379, Mar. 2004.

[VSH+00] L. Vanhamme, T. Sundin, P. V. Hecke, S. V. Huffel, and R. Pintelon. Frequency-Selective Quantification of Biomedical Magnetic Resonance Spectroscopy Data. *Journal of Magnetic Resonance*, 143(1):1–16, Mar. 2000.

[Wai02] A. D. Waite. *Sonar for Practicing Engineers.* Wiley, Chichester, England, 2002.

[Wel94] P. N. T. Wells. Ultrasonic Colour Flow Imaging. *Phys. Med. Biol.*, 38(39):2113–2145, Dec. 1994.

[WSSL83] R. F. Wagner, S. W. Smith, J. M. Sandrick, and H. Loepz. Statistics of Speckle in Ultrasound B-scans. *IEEE Trans. Son. Ultrason.*, 30(3):156 – 163, May 1983.

[Yan95] B. Yang. Projection Approximation Subspace Tracking. *IEEE Trans. Signal Processing*, 43(1):95–107, Jan. 1995.

[YK99] G. York and Y. Kim. Ultrasound Processing and Computing: Review and Future Directions. *Annu. Rev.Biomed. Eng.*, 01(1):559–588, aug. 1999.

[YMK03] Y. M. Yoo, R. Managuli, and Y. Kim. Adaptive Clutter Filtering for Ultrasound Color Flow Imaging. *Ultrasound in Med. and Biol.*, 29(9):1311–1319, 2003.

[ZH97] G. Zhu and Y. Hua. Quantitative NMR Signal Analysis by an Iterative Quadratic Maximum Likelihood Method. *Chemical Physics Letter*, 264:424–428, Jan. 1997.

[ZJJC04] Z. Zhang, A. Jakobsson, J. A. Jensen, and J. A. Chambers. On the Efficient Implementation of Adaptive Clutter Filters for Ultrasound Color Flow Imaging. In *Sixth IMA International Conference on Mathematics in Signal Processing*, pages 227–230, Cirencester, UK, 2004.

[ZJMC05a] Z. Zhang, A. Jakobsson, M. D. Macleod, and J. A. Chambers. A Hybrid Phase-based Single Frequency Estimator. *IEEE Signal Processing Letters*, 12(9):657–660, Sept. 2005.

[ZJMC05b] Z. Zhang, A. Jakobsson, M. D. Macleod, and J. A. Chambers. On the Efficient Estimation of Blood Velocities. In *Proceedings of the 2005 IEEE Engineering in Medicine and Biology 27th Annual Conference*, Shanghai, China, Sept. 2005.

[ZJMC05c] Z. Zhang, A. Jakobsson, M. D. Macleod, and J. A. Chambers. On the Efficient Frequency Estimation of a Single Tone. In *IEEE 13th Workshop on Statistical Signal Processing*, Bordeaux, France, July 2005.

[ZJMC05d] Z. Zhang, A. Jakobsson, M. D. Macleod, and J. A. Chambers. Statistically and Computationally Efficient Frequency Estimation of a Single Tone. Technical Report EE-2005-02, Dept. of Electrical Engineering, Karlstad Univ., Karlstad, Sweden, February 2005.

[ZJNC04] Z Zhang, A. Jakobsson, S. Nikolov, and J. A. Chambers. A Novel Velocity Estimator Using Multiple Frequency Carriers. In *Medical Imaging 2004: Ultrasonic Imaging and Signal Processing*, volume 5373, pages 281 – 289, San Diego, USA, Feb. 2004.

[ZJNC05a] Z. Zhang, A. Jakobsson, S. Nikolov, and J. A. Chambers. Extending the Un-

ambiguous Velocity Range Using Multiple Carrier Frequencies. *IEE Electronics Letters*, 41(22):1206–1208, Oct. 2005.

[ZJNC05b] Z. Zhang, A. Jakobsson, S. Nikolov, and J. A. Chambers. On Multicarrier-based Velocity Estimation. Technical Report EE-2005-04, Dept. of Electrical Engineering, Karlstad Univ., Karlstad, Sweden, May 2005.